UNIVERSIDAD POLITÉCNICA DE MADRID

Escuela Técnica Superior de Ingeniería y Sistemas de Telecomunicación



Contribution to the modelling and advanced simulation of photovoltaic applications

DOCTORAL THESIS

Submitted for the degree of Doctor by:

Francisco Javier Ramírez Ledesma

Máster Universitario en Sistemas Telemáticos e Informáticos

Madrid, 2023





UNIVERSIDAD POLITÉCNICA DE MADRID
Escuela Técnica Superior de Ingeniería y
Sistemas de Telecomunicación

Doctoral Degree in Systems and Services Engineering for the Information Society

Contribution to the modelling and advanced simulation of photovoltaic applications

DOCTORAL THESIS

Submitted for the degree of Doctor by:

Francisco Javier Ramírez Ledesma

Máster Universitario en Sistemas Telemáticos e Informáticos

Under the supervision of:

Dr. Eduardo Lorenzo Pigueiras (Supervisor)

Dr. Rita Hogan de Almeida (Co-supervisor)

Madrid, 2023

Title: Contribution to the modelling and advanced simulation of photovoltaic applications

Author: Francisco Javier Ramírez Ledesma

Doctoral Programme: Systems and Services Engineering for the Information Society

Thesis Supervision:

Dr. Eduardo Lorenzo Pigueiras, Catedrático de Universidad, Universidad Politécnica de Madrid (Supervisor)

Dr. Rita Hogan Teves de Almeida, Profesor Contratado Doctor, Universidad Politécnica de Madrid (Co-supervisor)

External Reviewers:

Thesis Defense Committee:

Thesis Defense Date:

This thesis has been partially supported by:

- The work presented in Chapter 2 is part of the Project MADRID-PV2 (P2018/EMT-4308), funded by the Comunidad de Madrid with the support from ERDF Funds.
- The author acknowledges financial support from the Spanish MCIN/AEI/10.13039/501100011033 through the GREASE project (PID2020-113533RB-C31) for the work presented in Chapter 3.
- The work presented in Chapter 4 was possible thanks to the funding from the European Union's Horizon 2020 research and innovation program for the SOLAQUA project under grant agreement No. 952879 and thanks to the Project MADRID-PV2 (P2018/EMT-4308) funded by the Comunidad de Madrid with the support from ERDF Funds.

A mis padres, Pablo (1941-2018) y Felisa (1942-).
"Pescador que pesca un pez, pescador es."

A mis hijos, Héctor (2010-), Diego (2012-) y Noa (2012-).
"Uno llega a ser grande por lo que lee y no por lo que escribe" (Jorge Luis Borges)

.

Acknowledgement

A Eduardo y Luis. Director y Tutor. Aprendí lo que pude de dos enormes investigadores y personas sabias. Vuestra entrenada intuición es la base de esta tesis. Gracias infinitas.

A Rita, Codirectora. Tu ayuda ha sido imprescindible. Gracias por la revisión.

A Francisco, Pablo, Celena, Luismi, Laura, Eva, Estrella, Ana Belén, Carlos, Pedro, Isaac, Juancho, Juan, Kiane, Cristina, Gonzalo, Felipe y disculpas si me dejo a alguien. Pasado, presente y futuro del Grupo de Investigación SPV. Sois el mejor equipo.

A Rodri, Jorge, Manu, Miguel de QPV, y Mikel, Nacho, Ricardo de Acciona Energía. Una gran experiencia en Benban (Egipto). Ojalá coincidamos en otras plantas FV.

A Sofía, Juan, equipo de G-Advisory. Nos acercáis la realidad y aprendemos juntos.

A Javier, amigo y compañero de despacho y proyectos. Que sigamos recorriendo camino juntos. Gracias por tu revisión.

A Fernando, Javier, Antonio. Compartimos la Dirección del Departamento DTE-UPM durante 5 años. Sin vuestro ánimo y tu empujón, Fernando, esto no habría comenzado.

A mis compañeros del Departamento DTE. José Luis, contigo empecé. Pablo, anímate.

A César, Eduardo, Ana Belén, CAPD de la ETSIST-UPM. Por vuestra labor.

A mis amigos y familiares. Nos hemos visto menos de lo deseado en esta etapa, pero seguís ahí.

Abstract

Firstly, this thesis addresses open issues in the application of bifacial photovoltaic (PV) modules by investigating the modelling of the energy performance of large-scale bifacial plants, the contribution of backside irradiance and its correlation with on-site measurement campaigns. A simplified two-dimensional (2D) view-factor model for bifacial PV systems is presented. This model also accounts for non-uniform back irradiance. The influence of varying structure height is found to be less significant than row-to-row spacing. The calculated bifacial gain is lower than the state of the art at the time of publication. Experimental observations over 10 months in a 6.6 kW_p PV system validate the predictive accuracy of the model and establish average back-irradiance at some points as a suitable predictor for DC power estimation. It also corrects the state of the art on the early existence of bifacial modules and their modelling by presenting a pioneering chapter on the industrialisation of bifacial PV modules in Spain (1984-1989) and the first application of the view factor to the modelling of bifacial PV modules.

Secondly, this work provides an answer to the emerging question of how the productivity expectation of large monofacial and bifacial PV systems, both with fixed structure and with single-axis tracking, varies when they are not located on horizontal terrain, but on terrain with arbitrary orientation and slope, the so-called complex orography. For this purpose, an evolution of the 2D view-factor model is proposed and described, which allows to dispense with the previous horizontality constraint. Equations are also provided for extending the tracking (and backtracking) angles of existing single-axis tracking controllers, which were previously restricted to horizontal terrain. A real case study of a 90 MW_p PV plant on uneven terrain is analysed, taking into account the terrain orography and the relative frequency distribution of the STC power on different facets. The results show that, depending on the azimuth and slope values of the terrain and the orientation of the axis, the energy yield can be higher or lower than that associated with a horizontal terrain. The weighted average performance of the whole PV system, taking into account the relative frequency of the facets, shows a performance potential comparable to that of a horizontal terrain on the favourable facets.

Finally, in the emerging market of high-powered PV irrigation systems (PVIS), simulation tools are also crucial for estimating energy and water productivity. A solution was available for modelling a PVIS consisting of a single pump powered by a PV generator, allowing to match the energy required by the pump at any moment with the energy available from the generator. However, most real high-power PVISs consist of several pumps in parallel. This work allows the modelling of these multi-pump PVIS systems that share a PV generator and a hydraulic system. The current objective of the model is to maximise the instantaneous water flow rate as a function of the available PV power. The ability to model multi-pump systems made it possible to detect errors in the PV sector when estimating multi-pump systems from the result of a single pump in the system. The model demonstrates the ability to compare different multi-pump designs. For example, two groups of pumps operating at variable frequency are shown to perform better than one group operating at variable frequency and one at nominal frequency, resulting in an 8% increase in water pumped.

All those contributions have been implemented in the SISIFO simulation tool, which has been developed by the Instituto de Energía Solar in several European projects since 2005. The tool has also been improved by implementing a new microservices architecture and a new web interface.

Resumen

En primer lugar, esta tesis aborda cuestiones de las grandes plantas fotovoltaicas (FV) bifaciales. Investiga su rendimiento energético, la contribución de la irradiancia trasera y su correlación con las campañas de medición in situ. Para ello, se desarrolla y presenta un modelo bidimensional (2D) basado en factores de visión aplicable a sistemas FV bifaciales. Este modelo permite considerar la no uniformidad de la irradiancia trasera. Como resultado, la influencia de la variación de la altura de la estructura es menos significativa que la del espaciado entre filas. La ganancia bifacial que se obtiene es inferior a la publicada en el estado del arte. Las observaciones experimentales realizadas en un sistema FV de 6,6 kW_p validan la precisión predictiva del modelo, y permiten establecer que la irradiancia trasera, obtenida como media aritmética en algunos puntos, se corresponde adecuadamente con la potencia generada. Además, se presenta un capítulo pionero sobre la industrialización de los módulos FV bifaciales en España (1984-1989) y el primer caso de aplicación de factores de visión a la modelización de módulos FV bifaciales, corrigiendo el estado del arte acerca de ambos aspectos.

En segundo lugar, este trabajo responde a la pregunta de cómo varía la expectativa de productividad de grandes plantas FV con seguimiento a un eje, cuando se ubican en terrenos con orientación y pendiente arbitrarias (orografía compleja) en lugar de horizontales. Para ello, se propone y describe una evolución del modelo matemático 2D basado en factores de visión, que permite prescindir de la anterior restricción de horizontalidad en plantas FV mono y bifaciales. Se proporcionan nuevas ecuaciones para calcular los ángulos de seguimiento que permiten adaptar los controladores de seguimiento de un eje que usaran las ecuaciones restringidas al caso horizontal. Se analiza un caso real de una planta FV de 90 MW_p en una orografía compleja, conocida la distribución de frecuencias relativas de la potencia STC en cada orientación del terreno. Los resultados muestran que, en función de los valores de acimut y pendiente del terreno y de la orientación del eje del seguidor, el rendimiento energético podría ser superior o inferior al asociado a un terreno horizontal, no siempre inferior.

Por último, en el mercado emergente de los sistemas de riego FV (SRFV) de alta potencia, las herramientas de simulación también son cruciales para estimar la

productividad energética e hídrica. Era posible modelar un SRFV constituido por una única bomba (monobomba) alimentada por un generador FV. Para ello, se calcula el punto de trabajo adecuado de la bomba centrífuga para que la energía demandada del generador FV nunca supere la energía que este puede proporcionar. Sin embargo, la mayoría de los SRFV reales de alta potencia constan de varias bombas en paralelo (multibomba). Esta tesis permite modelar estos SRFV multibomba que comparten un mismo generador FV y un sistema hidráulico. El modelo obtiene el punto de operación de cada bomba para maximizar el caudal instantáneo de agua en función de la potencia FV disponible. Se ha detectado un error frecuente en el sector FV al extrapolar la productividad de SRFV multibomba a partir de la productividad de un SRFV monobomba. El modelo permite, además, comparar distintos diseños y combinaciones de bombas. Como ejemplo, se muestra en un caso representativo donde dos grupos de bombas, ambos funcionando a frecuencia variable, presentan un mejor rendimiento que un grupo que funcione a frecuencia nominal y otro a frecuencia variable (un aumento del 8% del agua bombeada).

Estas contribuciones se han implementado en la herramienta de simulación SISIFO, desarrollada por el Instituto de Energía Solar a lo largo de varios proyectos europeos desde 2005. Además, se ha mejorado la herramienta implementando una nueva arquitectura de microservicios y una nueva interfaz web que permita su acceso abierto.

Table of Contents

Acknowledgement ..... *iii*
Abstract ..... *v*
Resumen ..... *vii*
Table of Contents ..... *ix*
List of Figures ..... *xiii*
List of Tables ..... *xvii*
Abbreviations and Acronyms ..... *xix*

Chapter 1 ..... **25**
INTRODUCTION **25**

1.1 Introduction 25
1.2 Background 28
1.3 Objectives 32

1.3.1 Related to photovoltaics 32
1.3.2 Related to simulation software 33

1.4 About this thesis 34

Chapter 2 ..... **37**
A SIMULATION MODEL OF THE IRRADIATION AND ENERGY YIELD OF LARGE BIFACIAL PV PLANTS ON FLAT TERRAIN **37**

2.1 Introduction 37
2.2 The 2D bifacial radiation model 41

2.2.1 Shaded and unshaded segments of ground 41
2.2.2 Other rear irradiance components 45
2.2.3 Non-uniformity 47

2.3 Electrical and thermal models 52
2.4 Performance ratio 54
2.5 Experimental observations 55

2.5.1 Experimental set-up 55
2.5.2 Errors in P_{DC} estimates 57
2.5.3 Performance and PR values 59
2.6 Implementation in SISIFO: bifacial PV performance model 60
2.6.1 Static structure 61
2.6.2 Horizontal single-axis trackers 63
2.7 Blind PV modelling intercomparison 66
2.8 Conclusions 67
Chapter 3 71
SINGLE-AXIS TRACKING AND BIFACIAL GAIN ON SLOPING TERRAIN 71
3.1 Introduction 71
3.2 Tracking software background 72
3.3 The backtracking geometry 77
3.4 Implementation in SISIFO 83
3.4.1 Irradiance components 85
3.5 A representative example 86
3.5.1 Relationship between terrain slope and energy yield for horizontal NS oriented axis trackers. 89
3.5.2 Influence of other parameters: GCR, ρ and H 91
3.5.3 NS oriented non-horizontal axes. 92
3.5.4 Other than NS oriented axes 93
3.6 Uneven terrains 95
3.6.1 Example 98
3.7 Conclusions 100
Chapter 4 103
MODELLING AND SIMULATION OF MULTIPUMPING PV IRRIGATION SYSTEMS 103

4.1 Introduction 103
4.2 Materials and Methods 108
4.3 Modelling of the Multipumping PV Irrigation Systems 110
4.3.1 Configuration 1: Multipump PVIS Made Up of a Group of N Equal Motor Pumps, in Parallel and Synchronized in Frequency 110
4.3.2 Configuration 2: Group of N Equal Pumps + Group of M Equal Pumps 115
4.4 Results and Discussion 122
4.4.1 Independent PV Generators vs. Shared PV Generator 123
4.4.2 Performance vs. Type of Frequency Control 125
4.4.3 Performance of a Study Case N = 5 and M = 2 127
4.5 Conclusions 132

Chapter 5 135
THE SISIFO SIMULATION SOFTWARE TOOL AS AN OPEN ACCESS TOOL 135

5.1 Introduction 135
5.1.1 Background 135
5.1.2 Starting point and aims 137
5.2 Architecture 139
5.2.1 Simulation engine 140
5.2.2 Web interface based on a single page application (SPA) model 140
5.2.3 Simulation microservice 141
5.3 Volumetry and usage statistics 144
5.3.1 Volumetry 144
5.3.2 Statistics 144
5.4 Conclusions 148

Chapter 6 151
CONCLUSIONS AND FUTURE WORK 151

6.1 Conclusions 151

6.2 Future work 156

Chapter 7 163

DISSEMINATION 163

7.1 International peer-reviewed journals 163

7.2 Conference papers 164

7.3 Technology transfer 165

Annex A 167

References 170

List of Figures

Figure 2.1 PV plants with bifacial modules produced in the 1980s. (a) A 8.1 kWp one installed in Noto (Senegal) in 1986 (E. Lorenzo, Montero, and Egido 1988); (b) a 9.9 kWp one installed in Rio Madera (Spain) in 1989 (Lancho 1989); (c) Rural Andalusian houses and (d) a 5 kWp PV pump still in operation in Jaen (Spain). Photos belong to IES-UPM own collection.....38
Figure 2.2. Two-dimension (2D) geometry of a bifacial PV array.....42
Figure 2.3. Geometry of the view factor from the segment L_1L_2 to a surface element dR.....43
Figure 2.4. Limit angles of the view field from a rear point of a PV array.....45
Figure 2.5. Ground, rear row and sky contributions to the rear irradiance.....46
Figure 2.6. Simulated distributions of G_{REAR} along a row (X_F is -0.5 for its top edge and +0.5 for its bottom edge) for a static PV plant located in Madrid (a) at noon throughout the year (b) at noon of the two solstices and spring equinox (c) GNU throughout the year (d) GNU along the two solstices and spring equinox.....49
Figure 2.7. View factor from unshaded segments, VF_{NS}, to the center point of the row (a) throughout the year (b) throughout the two solstices and spring equinox. View factor from shaded segments, VF_S, to the center point of the row (c) throughout the year (d) throughout both solstices and spring equinox.....50
Figure 2.8. Simulated distributions of G_{REAR} along a row (X_F is -0.5 for its top edge and +0.5 for its bottom edge) for a horizontal single-axis tracking PV plant located in Madrid and characterized by H=0.8 and L=3 (a) at noon throughout the year (b) at noon of the two solstices and spring equinox (c) GNU throughout the year (d) GNU along the two solstices and spring equinox.....51
Figure 2.9. Front (a) and rear (b) views of the bifacial PV plant operating at the IES-UPM roof.....56
Figure 2.10. Daily evolution of the rear irradiance values measured at the center and in two edges of the PV array throughout (a) a clear day (October 5th 2019), and (b) a cloudy day (November 22th 2019). Note that the range of left-'y'-axis is different in the graphics.....57
Figure 2.11. Errors in P_{DC} estimates. The left and right columns correspond to errors when using $G_{REAR,CENTER}$ and $G_{REAR,AVERAGE}$, respectively. The upper row plots errors versus irradiance. The middle row plots errors versus GNU, and the lower row presents the error histograms.....58
Figure 2.12. Sankey diagram corresponding to a representative bifacial static-structure PV plant.....62
Figure 2.13. Yearly irradiation bifacial ratio, G_yBR, depending on H and L.....62
Figure 2.14. Sankey diagram corresponding to a representative bifacial horizontal north-south one-axis tracking PV plant.....64
Figure 2.15. Yearly irradiance bifacial ratio, G_yBR, depending on H and L.....65
Figure 3.1. Sun and tracker positions in site (left) and tracker (right) reference frames. Depicted cases are: (**a**) Horizontal ground and north-south oriented axes; (**b**) Axes with given azimuth, αA, on flat

terrain. (**c**) Ground and axes with given azimuth, $\alpha A = \alpha G$, and tilt, $\beta A = \beta G$; (**d**) Ground and axes with different azimuth, $\alpha A \neq \alpha G$, and tilt, $\beta A \neq \beta G$, leading to a non-zero cross-axis slope angle, βCS, between horizontal and the axes line. 76
Figure 3.2. Geometry of backtracking for (**a**) horizontal and (**b**) sloping terrain. Both are equivalent, i.e. lead to the same rotation angle if $\Delta LC = LC0\ tan\omega IDtan(\beta CS)$....79
Figure 3.3. Evolution of ωID and ωIDC for βCS=0° (left) and βCS=15° (right) of a tracker with a limit rotation angle of 55° throughout a June day at a location at $40.38°N$ latitude. 80
Figure 3.4. Two-dimensional geometry of the (**a**) a bifacial PV array formed by equally spaced rows of and (**b**) the view factor from the segment $L1L2$ to the receiver surface element. 82
Figure 3.5. βCS affectation on a generic view factor edge for (**a**) $GREAR$ and (**b**) $GFRONT$. 83
Figure 3.6 Points selected for $GREAR$ calculation. The average of the irradiance calculated for these four points is then used as an input for the power calculation....88
Figure 3.7. (Left) $\Delta YF, y$, $\Delta GFRONT, y$, $\Delta GREAR, y$ and $\Delta GB, y$ versus βEW for the case of horizontal NS oriented axis. (Right) The same for the significant radiation components: $\Delta GFRONT, yB$; $\Delta GFRONT, yDS$; $\Delta GFRONT, yRG$; $\Delta GREAR, yRG$ and $\Delta GREAR, yDS$. 91
Figure 3.8. (left) Annual final energy yield, (center) annual bifacial radiation and (right) corresponding sensitivity to βEW versus (upper) GCR, (center) ρ and (bottom) H. 92
Figure 3.9. (left) Annual final energy yield, (center) annual bifacial radiation and (right) corresponding sensitivity to βEW versus βNS. 93
Figure 3.10 (left) A terrain with a slope, βEW, only in the EW direction and a tracker axis with a given azimuth, αA; (right) the resulting axis slope βA and cross-axis slope βCS as a function of αA for three βEW values 94
Figure 3.11. (**a**) (top) YF, y versus βEW and αA; (left) YF, ydetail for some αAvalues; (right) EW slope sensitivity with respect to $YF, y(\beta NS = 0, \beta EW = 0, \alpha A)$ for each αA. (**b**) Front and (**c**) rear (left) annual radiation versus βEW and αA, and (right) EW slope sensitivity with respect to $(\beta NS = 0, \beta EW = 0, \alpha A)$ radiation for each considered αA 95
Figure 3.12. EW profile of an uneven terrain with translational symmetry in NS direction....96
Figure 3.13. Real (red) ground profiles, with concave and convex zones, versus implicitly assumed (blue) ones. 97
Figure 3.14. Orography of the land on which a commercial PV plant will be built. On the left is the original state of the land (the explanation of the colour code is given in the text), and on the right is the arrangement of the tracker axes after a partial earth movement. It is clear that the PV designer has tried to make the most of the pink areas with favourable slopes. 99
Figure 4.1. Configuration of a PV pumping system: PV generator, frequency converter, centrifugal motor pump, and water pool. 104
Figure 4.2. Model consisting of a group of several equal pumps in parallel that share a PV generator. ...109
Figure 4.3. Model consisting of two groups of pumps working in parallel and sharing the same PV generator....110

Figure 4.4. Characteristic curves of an equivalent pump corresponding to N equal and frequency-synchronized pumps, where N = 1..5. 111
Figure 4.5. Illustration of the procedure to calculate the P2 required by the equivalent pump working at a certain point (QB, HB). Point A would be the operating point on the system curve if the pump were operating at the rated frequency, ω_rated. Point B is the actual operating point at a lower frequency. The pump works at the same efficiency at point B as at point C, therefore allowing P2 at point B to be calculated. 113
Figure 4.6. PDC-Q curves of each of the equivalent pumps of a group of five equal and synchronized pumps. 115
Figure 4.7. For the case N = 2 and M = 1, Q-H curves and the working point when n = 2 and m = 1 active pumps at Hs 118
Figure 4.8 Q-H curves and working points for the case N = 2 and M = 1 and the Q-H locus where the second group of variable frequency pumps is required to work for each combination of n active pumps in the first group 118
Figure 4.9. P_{DC}-Q curves for each combination (m, n) of active pumps for the case N = 2 and M = 2. 119
Figure 4.10. For the case N = 2 and M = 2, combination of pumps that maximizes the water flow pumped depending on available P_{DC}, as well as the frequency at which the two groups of pumps will work; (**a**) operation view—working frequencies, (**b**) design view—efficiencies, power balance, not used P_{DC}. 120
Figure 4.11. Q-H curves and working points for the case N = 2 and M = 1, and the Q-H "pseudo system area" where the second group of variable frequency pumps is required to work for each combination of n active pumps working at variable synchronized frequency in the first group. 121
Figure 4.12. For the case N = 2 and M = 2, combination of pumps that maximizes the water flow pumped for a certain available P_{DC}, as well as the frequency of the two groups of pumps; (**a**) operation view—working frequencies, (**b**) design view—efficiencies, power balance, non-useful P_{DC}. 122
Figure 4.13. H-Q and P_{DC}-Q characteristic curves—(**a**) and (**b**), respectively—for each of the equivalent pumps for N = 5 and M = 2 123
Figure 4.14. (**a**) A single pump connected to a single PV generator of P_{nom1}. (**b**) Group of N pumps sharing a single PV generator of $N \times P_{nom1}$. 124
Figure 4.15. Relative gain of the volume pumped in the N case with respect to the base case with and without resizing the hydraulic piping system. 125
Figure 4.16. Three possible frequency controls under comparison: (**a**) both pumps work synchronized at a variable frequency, (**b**) one pump works at a constant (nominal) frequency, and the second pump works at a variable frequency, and (**c**) one pump works at a variable frequency, and the second pump also works at a variable frequency, which can be different. 126
Figure 4.17. Combination of pumps that maximizes the water flow pumped for a certain available P_{DC}, as well as the frequency at which the two groups of pumps will work in control (**a**)—n pumps at

nominal frequency and m pumps at variable frequency; and in control (**b**)—n pumps at a variable frequency and m pumps at other variable frequency. 129
Figure 4.18. Cloudy and clear day. Case N = 5 and M = 2. (As there are two groups of different pump types, the best combination (with the chosen criteria) can include 0 or more active pumps in each group. A line disappears (discontinuous effect) in those combinations where there are 0 active pumps in one of the groups.) 131
Figure 5.1 Generic example of microservices architecture. Source: (Microsoft n.d.) 140
Figure 5.2 Sequence diagram of the concurrent execution of simulations by the microservice. 143
Figure A.1. Bifacial reference module (a) View of the frontal side (b) Electrical scheme 168
Figure A.2. (a) Bifacial reference module (rear view) and calibrated reference cell to measure G_{REAR} (b) Comparison between the G_{REAR} measured by both devices 169

List of Tables

Table 1.1 Publications in high impact scientific journals in relation to new model proposals implemented in SISIFO. 29
Table 2.1. Statistical parameters of errors in P_{DC} estimates in %. 58
Table 2.2. Statistical parameters of the weekly results of measured AC energy, front and rear (center, and three-points average) irradiations and the corresponding front and bifacial PRs. 59
Table 2.3. Results of the simulation for a representative static-structure PV plant. 61
Table 2.4. Yearly in-plane irradiation $G_y=G_{FRONT}+G_{REAR}$ and yearly DC energy yield improvement ratios in relation to the analyzed (H=0.8, L=2) case. 63
Table 2.5. Yearly results of the simulation for a representative bifacial horizontal one-axis tracking PV plant. 63
Table 2.6. Yearly in-plane irradiation $G_y=G_{FRONT}+G_{REAR}$ and yearly DC energy yield improvement ratios in relation to the analyzed (H=0.8, L=3) case. 65
Table 3.1. Influence of βCS on the different irradiance components. 85
Table 3.2. Characteristics of the baseline simulated case. 87
Table 3.3. Simulation results for the reference PV plant. 89
Table 3.4 (left) Relative frequency of STC power for each $(\alpha G, \beta G)$ bean. (right) Corresponding gain/loss relative to the reference horizontal case. Azimuth and slope values are in degrees. 99
Table 4.1. Simulated yearly relevant results for each type of control 127
Table 4.2. Simulated yearly results for the two configurations in Los Monegros 128

Abbreviations and Acronyms

(x_G, y_G, z_G)	Ground coordinates vector in a local reference frame
(x_S, y_S, z_S)	Solar coordinates vector in a local reference frame
(x_S''', y_S''', z_S''')	Solar coordinates vector in a tracker reference frame
a	Ratio of thermal voltage to open circuit voltage
AC	Alternating Current
c	Two-dimensional(2D) radiant intensity (radiant flux emitted per unit angle)
C_T	Coefficient of variation of cell temperature with irradiance
DC	Direct Current
DHI	Diffuse horizontal irradiance
DP	Dynamic Programming
dR	Infinitesimal flat receptor
$D_y(0)$	Yearly diffuse horizontal irradiation
E_{AC}	AC energy output throughout the considered period
E_{DC}	DC energy output throughout the considered period
F_T	Transparency factor
G	Irradiance
G^*	Irradiance at STC
GBR	Irradiance bifacial ratio
GCR	Ground Coverage Ratio
G_{FRONT}	Irradiance on the front side of the modules
GHI	Global horizontal irradiance
G_mBR, G_yBR	Monthly and yearly irradiance bifacial ratio, respectively
GNU	Irradiance non-uniformity index
G_{REAR}	Irradiance on the rear side of the PV module, or rear irradiance
$G_{REAR,AVERAGE}$	G_{REAR} as an average of three points on the back of the PV module
$G_{REAR,CENTER}$	G_{REAR} at the center point of the rear side of the PV module
$G_y(0)$	Yearly global horizontal irradiation
H	Row center height, normalized to the transversal width of the row
INU	Current non-uniformity index
I_{SC}	Short-circuit current

L	Row-to-row space, normalized to the transversal width of the row
L_1L_2	Reflector segment
m	Slope of a regression line
MPP	Maximum Power Point
$NOCT$	Nominal Operation Cell Temperature
P_{DC}	Measured power (DC)
P_{MPP}	PV power of PV modules
PR_B	Bifacial Performance Ratio (considering both front and rear side irradiances)
PR_F	Front Performance Ratio (considering only the front side irradiance)
PV	Photovoltaic
PVGIS	Photovoltaic Geographic Information System
STC	Standard Test Conditions
T_A	Ambient temperature
T_C	PV module temperature
VF_{NS}	View factor from unshaded segments to a point of the rear side
VF_S	View factor from shaded segments to a point at the rear side
V_{OC}	Open-circuit voltage
$WGNU$	Weighted rear irradiance non-uniformity index
$WINU$	Weighted rear current non-uniformity index
X_F	Calculation point along the transversal section of the row (range from -0.5 to 0.5)
μ	Angle of the top edge of the rear row with the horizontal from X_F
ρ	Albedo of the reflector
ρ	Albedo
γ	Power temperature coefficient
γ'_s	Profile angle of the Sun
ϕ_1, ϕ_2	View angles of a shadow
ϕ_{E1}, ϕ_{E2}	Extreme angles which define the field of vision of the ground from X_F
B_{GROUND}	Direct solar irradiance on the ground
$B_{\mathrm{REAR}}^{\mathrm{SKY}}$	Direct solar irradiance on the rear side of the modules
$D_{\mathrm{CIR,GROUND}}$	Circumsolar component of the diffuse irradiance on the ground
$D_{\mathrm{ISO,GROUND}}$	Isotropic component of the diffuse irradiance on the ground
$D_{\mathrm{REAR}}^{\mathrm{SKY}}$	Diffuse irradiance from the sky on the rear side of the modules

$G_{\mathrm{FRONT(1A)}}$	An approximation to G_{FRONT} (intermediate variable)
$G_{\mathrm{REAR(1A)}}$	An approximation to G_{REAR} (intermediate variable)
G_{1A}	An approximation to G (intermediate variable)
G_{FRONT}	Frontal irradiance
G_{GROUND}	Irradiance on the ground (it is assumed equal to *GHI* when the ground is not shaded)
G_{MAX}	Maximum value of irradiance along a side of the row
G_{MIN}	Minimum value of irradiance along a side of the row
G_{REAR}	Rear irradiance on bifacial PV arrays
$G_{\mathrm{REAR}}^{\mathrm{GROUND}}$	Ground reflected component of irradiance on the rear side of the PV module
$G_{\mathrm{REAR}}^{\mathrm{ROW}}$	Rear-row reflected component of irradiance on the rear side of the PV module
$G_{\mathrm{REAR}}^{\mathrm{SKY}}$	Irradiance from the sky on the rear side of the modules
G_{REAR}^{L12}	Contribution of a reflector segment L_1L_2 to the rear irradiance
G_{SHADED}	Irradiance on a shaded segment
G_{UNSHADED}	Irradiance on an unshaded segment
G_R^{L12}	Contribution of the segment L_1L_2 to the irradiance at the receptor
$I_{\mathrm{SC,FRONT}}$	Short-circuit current of the front side of the PV module
$I_{\mathrm{SC,FRONT}}^*$	Short-circuit current of the front side of the PV module at STC
$I_{\mathrm{SC,REAR}}^*$	Short-circuit current of the rear side of the PV module
$I_{\mathrm{SC,REAR}}^*$	Short-circuit current of the rear side of the PV module at STC
L_{C0}	Horizontal distance between tracker rows in case of horizontal constraint
$L_{\mathrm{C}\beta}$	Horizontal distance between tracker rows
P_{FRONT}^*	Peak power of the front side of the PV module
P_{REAR}^*	Peak power of the rear side of the PV module
PV	Photovoltaic
S_1^N, S_2^N	Coordinates of both edges of the shadow N (N=0 is the own module shadow)
SPA	Single Page Application
$T_{\mathrm{C,FRONT}}$	PV module temperature at the front side
$T_{\mathrm{C,MPP}}$	PV module temperature at MPP
$T_{\mathrm{C,REAR}}$	PV module temperature at the rear side

$T_{C,voc}$	PV module temperature neglecting the effect of temperature on short-circuit current
T_c^*	PV module temperature at STC
V_{OC}^*	Open-circuit voltage at STC
W_{AC}	AC wiring losses
k_1	Anisotropic index
s_{ID}	Shadow length for ω_{ID}
α	Azimuth
α_A	Tracker axis azimuth
α_G	Azimuth of the steepest slope line of the terrain, terrain aspect
α_S	Solar azimuth
α_T	Thermal coefficients of I_{SC}
β	Tilt
β_A	Tracker axis tilt
β_{CS}	Ground slope in the cross-axis plane
β_{EW}	Ground EW slope
β_G	Ground slope in αG direction (steepest slope of the terrain)
β_{NS}	Ground NS slope
β_T	Thermal coefficient of V_{OC}
γ_S	Solar elevation in a local reference frame
γ_S'''	Solar elevation in a tracker reference frame
η_{FRONT}^*	Efficiency of the frontal side of the PV module
φ_I	Bifacial short-circuit current coefficient of the PV module
φ_P	Bifacial power coefficient of the PV module
ω	Tracker rotation angle: the clockwise angle around the tracker axis, where zero is the horizontal position in the 2D scene.
ω_C	Backtracking correction angle
ω_{ID}	Ideal, or true-tracking, value of ω
ω_{IDC}	Final resulting ω
ϕ_1, ϕ_2	Edge angles of 2D view fields
	Photovoltaic irrigation specific:
E_1	AC energy yield at the motor-pump input
E_{DC}	DC energy yield
$E_{DC,MPP}$	Potential DC energy yield (at MPP)
E_H	Hydraulic energy yield

f, ω	Frequency
$f_{z-1}(x)$	Cost of the rest of the path, in this case, the demanded DC power of the rest of z − 1 active pumps, PDC,z−1, pumping the rest of water flow, Qs − Qz at Hs
$g_z(x)$	State cost function, for this case, the demanded DC power by a single pump while pumping a water flow Qz at Hs
H	Pumping head
H_{B}	Pumping head at a certain duty point not included in the Q-H curve at nominal frequency
$k_{\mathrm{b0,1}}$, $k_{\mathrm{b1,1}}$, $k_{\mathrm{b2,1}}$	Parameters that fit the *Q-H* curve of the individual pump
$k_{\mathrm{b0},N}$, $k_{\mathrm{b1},N}$, $k_{\mathrm{b2},N}$	Parameters that fit the *Q-H* curve of the equivalent pump of N equal pumps
$k_{\mathrm{p0,1}}$, $k_{\mathrm{p1,1}}$, $k_{\mathrm{p2,1}}$	Parameters that fit the *Q-P2* curve of the individual pump
$k_{\mathrm{p0},N}$, $k_{\mathrm{p1},N}$, $k_{\mathrm{p2},N}$	Parameters that fit the *Q-P2* curve of the equivalent pump of N equal pumps
k_{s0}, k_{s2}	Parameters that fit the system curve
k_{z_n0},k_{z_n1},k_{z_n3},k_{z_n4}	Parameters that fit the "pseudo system curves"
m	Number of active motor pumps in the second group
M	Number of motor pumps in the second group
MP	Motor pump
n	Number of active motor pumps in the first group
N	Number of motor pumps in the first group
P_1	Demanded power at the input of the motor
$P_{1\mathrm{B}}$	P_1 at point B
P_2	Demanded power at the pump input (1 pump)
$P_{2,N}$	Demanded power at the pump input (N pumps)
$P_{2\mathrm{B}}$	P_2 at point B
P_{AC}	Power at the output of the frequency converter
$P_{\mathrm{AC,B}}$	Power at the output of the frequency converter at point B
P_{DC}	DC power
$P_{\mathrm{DC},z-1}$	Demanded DC power of the rest of $z-1$ active pumps, $P_{\mathrm{DC},z-1}$, pumping the rest of water flow, $Q_{\mathrm{s}} - Q_z$ at H_{s}
$P_{\mathrm{DC,mpp}}$	Available PV power
P_{DCmax}	Maximum DC power of the equivalent pump
P_{DCmin}	Minimum DC power of the equivalent pump

P_{HB}	Hydraulic power at point B
P_{HC}	Hydraulic power at point C
PVIS	Photovoltaic irrigation system
Q	Water flow
Q_1	Water flow of the individual pump
Q_B	Water flow at a certain duty point not included in the rated-frequency *Q-H* curve
Q_{min}	Minimum cooling water flow of the pumps
Q_N	Water flow of the equivalent pump of *N* pumps
Q_s	Required water flow at the system curve discretized in *S* samples ($0 < Q_z < Q_s$)
$Q_{s,max}$	Maximum required water flow at the system curve discretized in *S* samples
S	Number of samples from the system curve
x	Constrained state variable
Z	Number of equivalent pumps resulting from the possible combinations of *N* pumps
z	Each combination of active pumps
η_{FC}	Frequency converter efficiency
η_{PB}	Pump efficiency at point B
η_{PC}	Pump efficiency at point C
θ	Constant value that depends on the water density and gravity
ω_{max}	Maximum operating frequency of each individual pump
ω_{rated}	Rated frequency

Chapter 1

INTRODUCTION

"It's a dangerous business, Frodo, going out your door. You step onto the road, and if you don't keep your feet, there's no knowing where you might be swept off to." (J.R.R. Tolkien)

1.1 Introduction

The current and future importance of photovoltaic technology is beyond doubt. It is the energy source that has added the most capacity to the world's electricity system in recent years. In 2022, global installed solar capacity reached 1.18 TW (4.5% of global electricity capacity), of which 25% (300 GW) was added in 2022, 65% of renewable energy installed in 2022 (IEA-PVPS Task1 2023). And studies agree that future growth will need to be even faster to effectively mitigate global warming. In this respect, the International Renewable Energy Agency (IRENA) estimates that an "*annual deployment of some 1 000 GW of renewable power is needed to stay on a 1.5°C pathway*", this is, to limit global warming to 1.5° C by 2050 (IRENA, 2023).

This rapid growth requires a number of technological developments, both on the PV cell technology side and on the application (engineering) side. For the purposes of this work, PV engineering comprises two phases:

(a) During the design phase, a production expectation is established for a representative period. This is often the electrical energy supplied over a year in the case of direct grid connections, or the volume of water pumped over a quarter in the case of water pumping systems. In any case, this production expectation is obtained by means of a simulation exercise that aims to reflect reality as closely as possible and for which the simulation is based on a series of assumptions

concerning three different areas: (a) the evolution of the operating conditions on site (G and T_C), (b) the electrical characteristics of the system (sizes, efficiencies, temperature coefficients, etc.) and (c) the operating conditions (dirt, availability, etc.). The simulation software combines this information by means of behavioural models (of the photovoltaic generator, the inverter, the transformer, the motor pump, etc.) and the result is the evolution of the instantaneous output of the system (electrical power, flow rate, etc.), which in turn is integrated over the period considered (to obtain electrical power, volume of water pumped, etc.).

(b) During the operational phase, the data recorded during the actual operation of the system (irradiances, temperatures, currents, voltages, powers, etc.) are evaluated. Comparison with the corresponding values in the simulation makes it possible to detect any deviations between expectations and reality and to diagnose which assumptions are affected. In other words, it is necessary to analyse the extent to which reality matches expectations so that the models and loss scenarios used in future simulations can be adjusted and improved.

At this point it is important to stress that the result of a simulation depends on the quality of the software, understood as the goodness of its internal mathematical models, but also on some loss assumptions (mismatch, wiring, terrain roughness, dirt, etc.), which are mainly the result of the user's intuition or previous experience.

The current state of the art in photovoltaic simulation is characterised by:

(a) A certain availability of both commercial (PVsyst, ...) and open software (SAM, SISIFO, Radiance, ...). The most paradigmatic case is PVsyst, which is used as an industrial standard. Each software implements a set of mathematical models. Often the same mathematical model is implemented in several simulation software, and in such a case the results are not expected to be very different in terms of the aspect modelled. For a particular aspect, a software may offer several alternative models and, in such a case, the choice of the most appropriate model (based on the location or climatology of the site, the technology used, etc.) again depends on the intuition or experience of the user.

(b) Careful observation of reality is the way both to assess the quality of mathematical models and to refine the intuition of simulation software users. And it so happens that the current state of the art, although it may come as a surprise to some, reports that the difference between reality and expectations in terms of the annual production of a PV system is large. Independent studies contrasting the expectations established at the design stage with the actual production observed in the operational phase of commercial PV power plants consistently point out that the differences are on average in the order of 6% (kWh Analytics, 2021). Such a difference is very significant (in the current context, the profitability of PV projects is decided by less than this figure), which indicates that the current PV simulation scenario suffers from a lack of adherence to reality.

In our view, the current gap between expectations and reality is due to over-optimistic loss assumptions (e.g. soiling or availability) and the fact that some models do not adequately reflect reality (cell temperature or spectral losses are examples of open issues today).

The latter includes the consequence of using simplified models that simulate a much more complex reality. The modelling of single-axis tracking on horizontal terrain is a good example of this situation, as well as of one of the works carried out in the context of this thesis to mitigate the difference between expectations and reality. It happens that the irradiation gains (irradiation on the plane of the generators divided by the horizontal irradiation) observed in real plants are very often lower than those predicted by the simulation software. For example, recent IES-UPM studies at some commercial PV plants have shown that the simulation software calculates the position of the receivers (i.e. the angle of rotation of the trackers) assuming that the terrain is perfectly flat. However, real terrain, even if reasonably flat, always has some degree of roughness. This roughness means that if the angle calculated by the software for horizontal terrain were to be followed, mutual shadows would occur between the rows of trackers during the backtracking time. To avoid this, the trackers incorporate position corrections that reduce the angle of rotation, bringing it closer to the horizontal, which in turn results in a loss of irradiance. This means that some trackers are actually configured as if they were on slightly sloping terrain. In the simulation, however, the trackers are assumed to be on a

perfectly horizontal surface. In addition to diagnosing this situation, IES-UPM has also modelled the angle deviations observed in these installations, which makes it possible to refine the calculation of the estimated irradiance, bringing it closer to the actual observed irradiance.

Consequently, the development of new contributions in the field of modelling and simulation of PV systems is an open question and this thesis is mainly concerned with this aspect of PV engineering. The creation of expectations on the one hand, and the analysis of reality on the other hand, in order to improve behaviour models and loss scenarios, are two aspects that need to be addressed from the point of view of PV simulation. This thesis is based on PV simulation with the aim of obtaining expectations that are closer to reality. This involves both the definition and development of new mathematical models applicable to certain aspects of PV power plants and their implementation in simulation software.

1.2 Background

IES-UPM has developed the ability to simulate the electrical behaviour of PV systems at a pace dictated by the needs it perceives from providing services to the Spanish industrial sector. The process began in 1994 with the studies that underpinned the design of Toledo-PV, the first PV power plant to break the MW barrier in Europe. This was followed by the treatment of typical meteorological years, TMY - a tool that is now standard but was still in its beginnings at the time - and the development of the equations for tracking on a horizontal axis. The provision of the service itself was complemented by research to answer questions arising from the service itself. Thus, the work on Toledo PV resulted in the first two publications in the field, dealing with the development of the TMY of the region (Macagnan et al., 1994) and the details of horizontal tracking (Lorenzo & Macagnan, 1994).

Fortunately, the years that followed were marked by important milestones that provided as many opportunities for progress in photovoltaic simulation, in close contact with the reality observed in commercial power plants. In (Lorenzo et al., 2002), the 1.4 MW_p Tudela PV plant (the largest tracking plant in the world at the time) led to the generalisation of the treatment of tracking, including vertical axes. In the period 2005-2008, the so-called "*Spanish photovoltaic boom*" opened the way to bank financing in the

form of project financing ("*Project Finnance*"), which involves a strict control of the technical quality (as part of the "Due diligence") and served to extend the simulation to the rest of the components of a PV plant (inverters, transformers, etc.) and to develop a first tool made available to the public (the software was called IESPRO).

The work on this thesis started in 2018 at the same time as the emergence of PV technology in the field of mass electricity production and its penetration into other fields, in particular that of high-power water pumps for agricultural irrigation. The leap to tens of MW and the expansion of applications are accompanied by the emergence of technological innovations (bifacial modules, TOPCon, etc.) and increasing precision requirements, which, in short, have made it necessary for this thesis to represent a further step in the simulation capabilities of IES-UPM, materialised in SISIFO, the current software of IES-UPM, and also in its public availability through an online web-based interface (the use of SISIFO outside IES-UPM, through this online web interface, has reached about 57,000 simulations since its inception, and the demand comes from more than 50 countries).

The Table 1.1 presents the publications in high-impact scientific journals that are the result of this trajectory (de la Parra et al., 2017; Ledesma et al., 2020, 2022; Lorenzo et al., 2002, 2011; Lorenzo & Macagnan, 1994; Martin & Ruiz, 2005; Martín & Ruiz, 1999; Martínez-Moreno et al., 2010; Moretón et al., 2017; Narvarte & Lorenzo, 2008), and they are presented here as a brushstroke that helps to perceive both the continuity and the relevance of this trajectory, as well as the contributions of this thesis in particular.

Table 1.1 Publications in high impact scientific journals in relation to new model proposals implemented in SISIFO.

Models	**IES-UPM Publications: 11 (+1 under review) articles in Q1 and Q2 journals, between 1994 and 2023**
Effective irradiance	• Moretón, R., Lorenzo, E., Pinto, A., Muñoz, J., & Narvarte, L. (2017). From broadband horizontal to effective in-plane irradiation: A review of modelling and derived uncertainty for PV yield prediction. *Renewable and Sustainable Energy Reviews*, 78, 886–903.

	https://doi.org/10.1016/j.rser.2017.05.020
Tracking	• Lorenzo, E., & Macagnan, M. H. (1994). Considerations in the design of a one-axis tracking photovoltaic system. *Progress in Photovoltaics: Research and Applications*, 2(1), 45–55. https://doi.org/10.1002/pip.4670020107 • Lorenzo, E., Pérez, M., Ezpeleta, A., & Acedo, J. (2002). Design of tracking photovoltaic systems with a single vertical axis. *Progress in Photovoltaics: Research and Applications*, 10(8), 533–543. https://doi.org/10.1002/pip.442 • Narvarte, L., & Lorenzo, E. (2008). Tracking and ground cover ratio. *Progress in Photovoltaics: Research and Applications*, 16(8), 703–714. https://doi.org/10.1002/pip.847 • Lorenzo, E., Narvarte, L., & Muñoz, J. (2011). Tracking and back-tracking. *Progress in Photovoltaics: Research and Applications*, 19(6), 747–753. https://doi.org/10.1002/pip.1085
DC Power	• De la Parra, I., Muñoz, M., Lorenzo, E., García, M., Marcos, J., & Martínez-Moreno, F. (2017). PV performance modelling: A review in the light of quality assurance for large PV plants. *Renewable and Sustainable Energy Reviews*, 78, 780–797. https://doi.org/10.1016/j.rser.2017.04.080
Shading	• Martínez-Moreno, F., Muñoz, J., & Lorenzo, E. (2010). Experimental model to estimate shading losses on PV arrays. *Solar Energy Materials and Solar Cells*, 94(12), 2298–2303. https://doi.org/10.1016/j.solmat.2010.07.029

Angular response	• Martin, N., & Ruiz, J. M. (2005). Annual Angular Reflection Losses in PV Modules. *Progress in Photovoltaics: Research and Applications*, 13, 9. https://doi.org/10.1002/pip.585
Spectral response	• Martín, N., & Ruiz, J. M. (1999). A new method for the spectral characterisation of PV modules. *Progress in Photovoltaics: Research and Applications*, 7(4), 299–310. https://doi.org/10.1002/(sici)1099-159x(199907/08)7:4<299::aid-pip260>3.0.co;2-0
Contributions of this thesis:	
Bifacial modules (rear irradiance)	• Ledesma, J. R., Almeida, R. H., Martinez-Moreno, F., Rossa, C., Martín-Rueda, J., Narvarte, L., & Lorenzo, E. (2020). A simulation model of the irradiation and energy yield of large bifacial photovoltaic plants. *Solar Energy*, 206, 522–538. https://doi.org/10.1016/j.solener.2020.05.108
Pumping systems (multi-pump)	• Ledesma, J. R., Almeida, R. H., & Narvarte, L. (2022). Modeling and Simulation of Multipumping Photovoltaic Irrigation Systems. *Sustainability*, 14(15). https://doi.org/10.3390/su14159318
Sloping grounds	• Ledesma J. R., Lorenzo E., Narvarte L. One-axis tracking and bifacial gain on sloping grounds. (Under review; sent to *Progress in Photovoltaics: Research and Applications* in March 2023).

In addition, although not included in Table 1.1, several IES studies and analyses, some of which have also been published in high-impact journals, make use of the results obtained from various simulation exercises carried out with the SISIFO tool, with the flexibility offered by having one's own tool to adapt it if necessary or to analyse any intermediate results that may be relevant.

1.3 Objectives

As we have seen, this PhD thesis is framed in the strategy of keeping the simulation capabilities of PV systems at IES-UPM at the forefront of the state of the art and taking the lead in the evolution of the simulation capabilities of PV systems at IES-UPM. To this end, the contributions of this thesis are related to two different fronts: on the one hand to photovoltaics and on the other hand to simulation software.

1.3.1 Related to photovoltaics

With regard to photovoltaics, two types of activities can be distinguished:

(a) On the one hand, the development of mathematical models to deal with innovations arising from technological evolution and for which there is no well-established solution in the state of the art. Contributions in this sense, which can be understood as specific objectives of this thesis, have been:

- **Modelling the irradiance at the back of bifacial generators**. More than 40% of the current market is already bifacial, and this percentage is expected to grow.
- **Modelling of single-axis tracking (and fixed-tilt) photovoltaic plants on terrain with complex orography** (non-horizontal terrain). Although still in its infancy, PV on complex terrain is attracting increasing interest as flat land becomes scarcer or more expensive, or simply because reducing earthworks is seen as economically attractive.
- **Modelling of multi-pump systems for water pumping**. Pumping PV systems combine water and energy and have great potential for future growth

Each of these contributions has been or is being published in high-impact scientific journals. The corresponding articles constitute the basis of the Chapter 2 and Chapter 4. Chapter 3 is the basis of a journal article currently under review.

(b) On the other hand, **to refine some basic capabilities of SISIFO, to add new mathematical models available in the state of the art, to allow the simulation of new characteristics of PV systems or to refine the correct operation or implementation of the models**. Thus, improving the treatment of the Typical Meteorological Year (TMY), the operating point of photovoltaic generators when inverters are working in saturation (*clipping*), etc., power limitation at the interconnection point, improving the treatment of electrical losses, allowing the use of albedos in time periods shorter than a year (daily, monthly) or adding more cell temperature models, obtaining TMY data online or horizon height or motor pump characteristics from online databases, are some examples of this activity.

In general, the particular issues involved in this activity are not new to science. For example, the practical difficulty in dealing with the TMY arises from the fact that it is typically received in UTC time coordinates and on an hourly basis and needs to be corrected to True Solar Time coordinates, which requires an adjustment in minutes. The principles of translating data from one time system to another are well known, but the different time scales mean that care must be taken to ensure the consistency of the corrected TMY. Otherwise, strange results can occur, such as non-zero beam irradiance data at times before dawn. Because of this lack of novelty, and although this activity required a lot of effort (detecting and correcting hidden problems is always tedious) and was a *sine-qua-non* for keeping SISIFO properly updated, it is not dealt with in this thesis.

1.3.2 Related to simulation software

Regarding the simulation software itself, the aim of this thesis was **to address the necessary measures to ensure that the simulation software**, which was initially proprietary at IES-UPM, **could be used free of charge** by any user anywhere in the world.

The SISIFO base software was originally designed and implemented as a monolithic application in Matlab© and has a certain internal complexity (several types of PV generators, mathematical models, hybridisation with diesel systems, grid connection, ...).

In period 2012-2015, a first attempt was made to make it possible to use it online. To this end, a completely independent web application was developed. To carry out the calculation part of the simulation results of this application, a part of the calculation code in Matlab© was migrated to a script language (PHP). A web interface was added, also in PHP language, to collect parameters and display some of the simulation results.

However, the approach used suffered from a number of drawbacks related to usability, performance and the development and maintenance process. Therefore, another main objective of this thesis was **to propose and implement a different software architecture that avoids or minimises these drawbacks**.

1.4 About this thesis

The reminder of this thesis is organized as follows:

CHAPTER 2: A SIMULATION MODEL OF THE IRRADIATION AND ENERGY YIELD OF LARGE BIFACIAL PV PLANTS ON FLAT TERRAIN presents a simplified two-dimensional view factor model for bifacial PV plants, as well as a specific definition of performance ratio (PR) for this type of installations. This model has been implemented for static structures and horizontal single-axis trackers. It tries to answer some questions regarding the use of bifacial photovoltaic (PV) modules, such as how to link the energy-yield modelling of large bifacial PV plants with further on-site measurements campaigns, the effect of the non-uniformity of the rear irradiance, as well as the convenience of varying the geometry of the plants to enhance the bifacial contribution. A pioneering chapter of bifacial PV modules industrialization which took place in Spain between 1984 and 1989, and probably the first use of view factor to model bifacial PV modules, are also presented in this chapter.

CHAPTER 3: SINGLE-AXIS TRACKING AND BIFACIAL GAIN ON SLOPING TERRAIN describes a mathematical model for dealing with large bifacial single-axis tracking PV plants over terrain of arbitrary orientation and slope. The only constraint is that the ground surface and the plane of the tracker axes must be parallel. This allows for 2D modelling of the ground shading scene required for backtracking geometry and rear irradiance calculations. It also provides a set of equations for upgrading tracker

controllers, which were restricted to horizontal terrain. As a representative case, a real 90 MW_p PV plant installed on an uneven terrain is analised.

CHAPTER 4: MODELLING AND SIMULATION OF MULTIPUMPING PV IRRIGATION SYSTEMS solves the requirement of the growing market of high-power photovoltaic irrigation systems (PVIS) —made up of systems with different and multiple motor pumps working in parallel— of simulation tools capable of estimating their energy and water productivity. The aim of this Chapter is to present the simulation models developed for parallel multi-pump PVIS fed by a single PV generator. These models seek to maximize the instantaneous water flow rate according to the available PV power and were developed for the typical configurations of large-power irrigation facilities. The models present some advantages when compared with the current state of the art (in which a single motor pump connected to a $1/N$ fraction of the PV generator is simulated and the result is multiplied by N): in the case of negligible hydraulic friction losses, the use of the multi-pump model shows gains with respect to the state of the art; in the case of appreciable friction losses, the current state of the art overestimates the productivity of the systems. The ability of these models to compare different multi-pump designs is also demonstrated.

CHAPTER 5: THE SISIFO SIMULATION SOFTWARE TOOL AS AN OPEN ACCESS TOOL extends the background of the SISIFO software simulation tool in order to clarify the starting point of the work in this thesis, and explains the generality of the steps taken to achieve the objectives related to the simulation software.

CHAPTER 6: CONCLUSIONS AND FUTURE WORK summarizes the main results of this research work and points out some directions in which we are considering to expand it.

CHAPTER 7: DISSEMINATION is an account of the dissemination activities of the results of this thesis: journal articles, conference papers and technical workshops.

Chapter 2

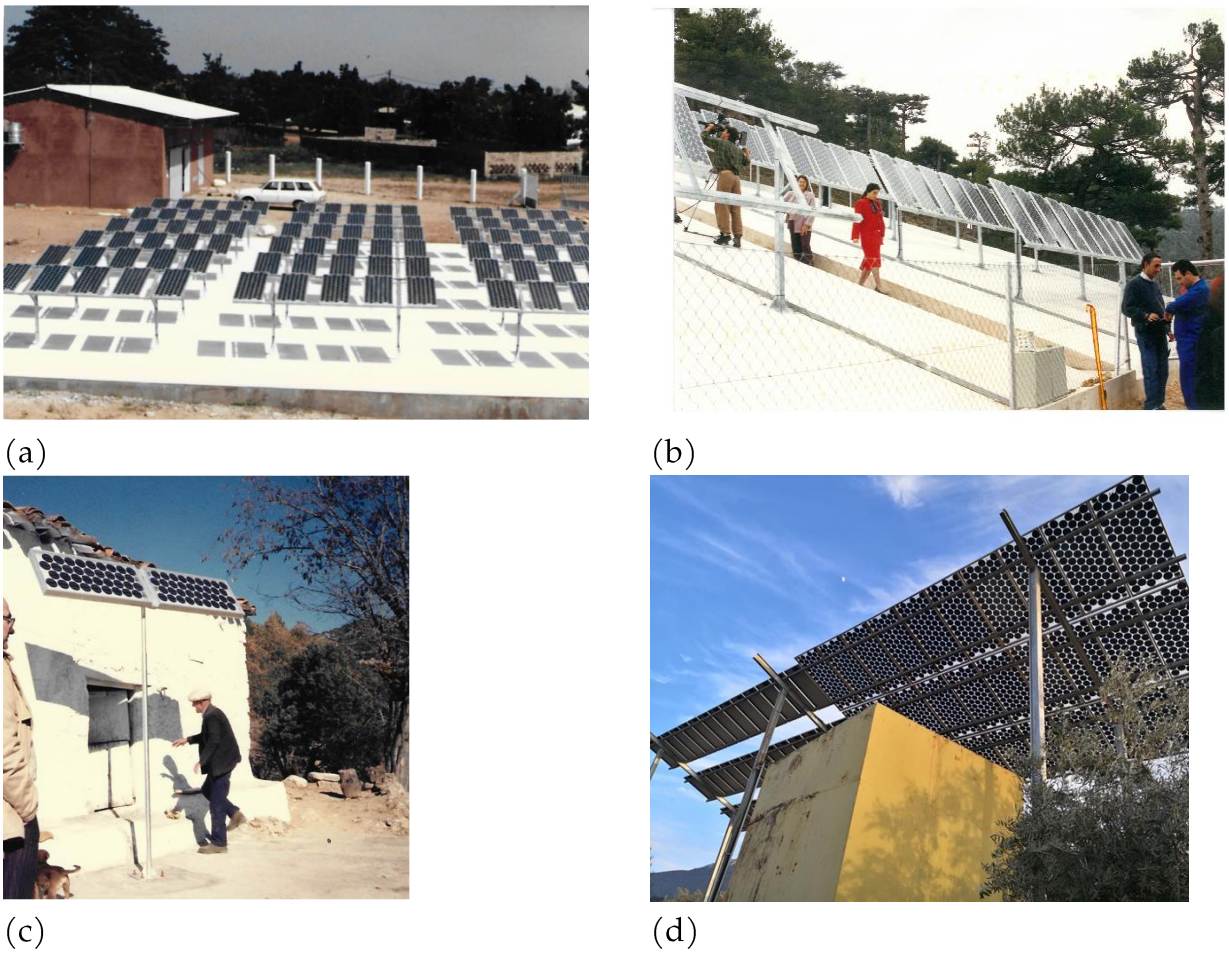
A SIMULATION MODEL OF THE IRRADIATION AND ENERGY YIELD OF LARGE BIFACIAL PV PLANTS ON FLAT TERRAIN

"Y el Sol es una lágrima en un ojo que no sabe llorar" (Joaquín Sabina)

2.1 Introduction

The research of bifacial PV technology dates back to 1960 (Hiroshi, 1966) and received a rush of attention in the late 1970s and early 1980s when a certain number of papers on high-efficiency bifacial solar cells were published. This early chapter of the bifacial PV history is widely known and often referred to in current publications (Cuevas, 2005),(Liang et al., 2019). In contrast, it is largely unknown that this early research on bifacial cells also led to the first industrial production of bifacial modules, which were released in Spain by Isofoton Inc. from 1984 to 1989. They were mainly installed in stand-alone PV systems for the rural electrification market, and on a 40 kW_p bifacial array of a 100 kW_p PV plant demonstrator connected to the grid (Solera, 1985). Figure 2.1 pays homage to this early chapter of bifacial PV industrial production, showing bifacial PV plants installed at that time. Even more, we have recently learned about bifacial modules produced at that time that are still in operation, as the one shown in Figure 2.1-d. However, this early industrial production and practical use of bifacial PV modules has

passed into oblivion. For example, a recent IEA report (IEA-PVPS Task13 2017) asserts that the first commercial bifacial modules were released by Sanyo in 2009. Other publications set back this date to 2000 (Podlowski, 2019; Chunduri & Schmela, 2017). On similar lines, other recent reviews say that the concept of bifaciality lived on after the early research on solar cells with no more than some propositions for several niche applications (noise barriers (Nordmann et al., 2012)[1], shades and fences) during the 1990s and early 2000s (Liang et al., 2019); or that bifacial systems construction started in Japan in 2013 (H. ; K. Nussbaumer, 2019).



(a) (b)

(c) (d)

Figure 2.1 PV plants with bifacial modules produced in the 1980s. (a) A 8.1 kW_p one installed in Noto (Senegal) in 1986 (Lorenzo et al., 1988); (b) a 9.9 kW_p one installed in Rio

[1] The first bifacial PV noise barrier was built in 1997 along a highway in Zürich, according to (Nordmann et al., 2012).

Madera (Spain) in 1989 (Lancho, 1989); (c) Rural Andalusian houses and (d) a 5 kW_p PV pump still in operation[2] in Jaen (Spain). Photos belong to IES-UPM own collection.

Not surprisingly, the use of bifacial modules in the 1980s created interest in examining the radiation reflected by the ground or other surroundings (the albedo), and the first energy-yield simulation models were also developed and published at this time. In 1984 (Luque et al., 1984) inaugurated both the calculation of the irradiance received at the rear of the modules, G_{REAR}, by means of the "view factor" commonly found in heat transfer text books (McAdams, 1954), and the assumption that ground and surroundings are ideal diffuse (i.e. Lambertian) reflector surfaces in the sense that the intensity of the reflected radiation is uniformly distributed irrespective of the nature of the incident radiation. Two years later, (Egido & Lorenzo, 1986) extended the application of this model to single-axis and two-axes trackers and, finally, (Krenzinger & Lorenzo, 1986) improved the model and enlarged its application to the case of modules surrounded by several diffusely reflecting surfaces, considering the effect of the interreflections among them.

We could not find publications dealing with bifacial radiation modeling up to 2014 (Yusufoglu et al., 2014). It is opportune mentioning that, in those early days of PV bifacial use in the 1980s, we spent quite some time experiencing with specific preparations to increase the albedo of the ground under the bifacial PV plants, as show in Figure 2.1-a, Figure 2.1-b and Figure 2.1-c. The general result was that, mainly because horizontal or low tilted surfaces are prone to accumulating dust, artificial increases of albedo usually last for a short time (a few months). Hence, these experiences suggest that the only practical solution for nowadays commercial bifacial PV plants entails just relaying on natural grounds, whose albedo (Iqbal, 1983) typically stays below 30% and more often below 20%. Outstanding exceptions are snow and vertical reflectors, as the one shown in Figure 2.1-c. In this latter case, we profited from the traditional yearly routine of whitening the walls by means of a coat of quicklime, widely extended in rural Andalusian homes. The vertical reflectors increase the *GBR* in winter, which is just the worst period for rural applications.

[2] Isofoton production of bifacial PV modules ceased in 2000. The modules in this system were part of a remaining stock and have been installed in 2013.

Currently, several companies are already offering industrial bifacial PV modules, and the corresponding market share is expected to grow to about 40% by 2028 (VDMA, 2018). And, again, this is increasing interest in rear radiation modelling, as shown by the corresponding rush of related publications[3] since 2015 and the recent inclusion of bifacial modelling capabilities in commercial PV simulation software[4]. In essence, there are two different approaches to model the radiation received by the rear-side of the PV module (Deline et al., 2017): the classic view factors, as described above, and ray-tracing simulation by means of specific software like Radiance (Asgharzadeh et al., 2017; Lo et al., 2015) or TracePro (Soria et al., 2016). In general, ray-tracing is more suitable for exploring the effects of detailed features, such as spacing between modules and/or cells, rack, etc. However, view factors are less demanding computationally and are found to be easier for analyzing large and regular arrays(Hansen et al., 2016), which are typically deployed in large-scale PV plants. That helps to explain why the view factors approach is the most extensively used today (Catena et al., 2018; Marion et al., 2017; Shoukry et al., 2016; S. Wang et al., 2015). Even more, simplified two-dimensional view factors can effectively model PV arrays formed by a large number of relatively long rows of PV modules equally spaced over the ground plane. Because shading ends at the edges of a PV array, the rear irradiance on the modules located close to the edges increases. However, some studies suggest that this is scarcely relevant in the case of large PV arrays. For example, it has been shown that, for single-axis trackers, 5 rows with 10 modules each bring the rear irradiance within 5% of the here considered 2D assumption(Hansen et al., 2016; Pelaez et al., 2018). The same reason has been argued by other authors in order to justify the option for 2D models (Marion et al., 2017).

Despite all this valuable work, an agreement on engineering practices for dealing with large bifacial PV plants has still not been reached. In particular, open questions remain in how to link the modelling of the energetic yield with further on-site measurement campaigns, i.e. on performance indexes definition and testing. This is in part due to the

[3] Several Workshops specifically devoted to Bifacial PV are being regularly held. Corresponding presentations can be found at https://pvpmc.sandia.gov/pv-research/bifacial-pv-project/; http://bifipv-workshop.com/;

[4] Bifacial modelling is available in PVsyst since 2017

non-uniformity of the rear irradiance that raises the question of the representativeness of the observed value at any given point and the question of associated mismatch losses. These impact both the estimation of energy yield and the determination of the Performance Ratio (PR).

This thesis aims to contribute on the establishment of such bifacial engineering practices. First, a simplified two-dimensional view factor optical model (section 2.2) and a bifacial power model have been developed and integrated in SISIFO --an open software for general PV system performance simulations freely available at www.sisifo.info. 2D view factor models have the advantage of being particularly simple to implement in already existing energy yield simulation tools for standard monofacial plants. In particular, only three additional items of data are required: the albedo, the height of the mounting structures and the power bifacial coefficient of the PV modules. The validity of the bifacial power model and the convenience of two different performance ratio PR formulations have been assessed in light of the experimental observations on a 6.6 kW_p bifacial PV array connected to the grid on the terrace of the IES-UPM since May 2019. Finally, we have analyzed the impact of the mounting structure layout of both static and horizontal single-axis trackers on yearly in-plane global irradiation (front plus rear) and on energy yield of a hypothetical PV plant located in Madrid.

2.2 The 2D bifacial radiation model

2.2.1 Shaded and unshaded segments of ground

Figure 2.2 shows a projection onto a vertical plane orthogonal to the rows composing a PV array with bifacial modules (i.e. forming an angle with the meridian plane equal to the azimuth of the rows). The ground is flat and parallel to the edge of the rows (but not necessarily horizontal). PV array geometry is defined by tilt angle, β, row-to-row space, L, and row center height, H. Note that L and H are normalized to the row width, so that the Ground Cover Ratio is equal to 1/L. The angle between the horizontal and the projection onto this vertical plane of the line drawn between the center of the Sun and the center of the Earth forms an angle γ_S', that is sometimes called profile angle (IEA-PVPS Task13 2017). That the length of the rows is infinite and that the number of rows is

also infinite are basic hypotheses of this model. That is, the edges of each row and of the PV array are not considered. The key is to realize that the regular disposition of the rows translates into a basic pattern, composed by a shaded and an unshaded segment, which repeats with a period equal to *L*. Note that this projection plane typically coincides with the North-South direction in the case of static arrays but with the East-West direction in the case of one-axis tracked ones.

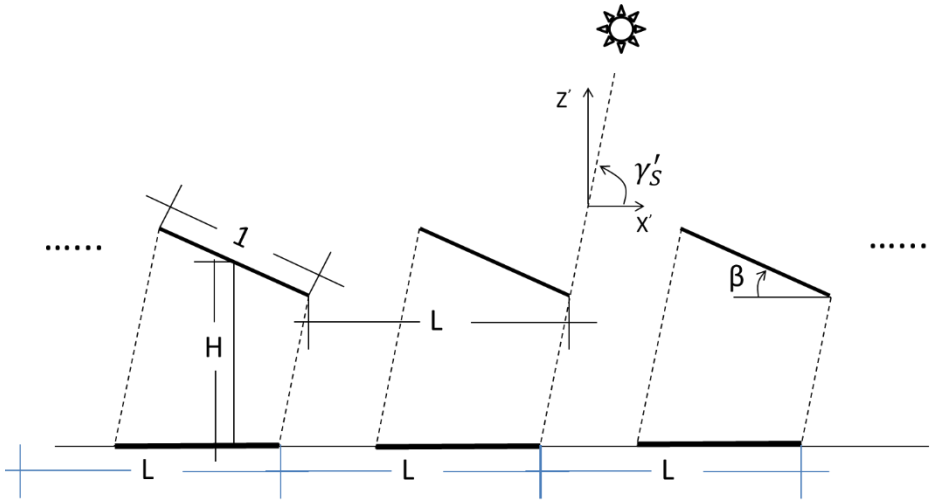


Figure 2.2. Two-dimension (2D) geometry of a bifacial PV array.

As a second step in the explanation of this model, let us imagine the hypothetical case of a ground made by an infinite and homogenous Lambertian reflector uniformly illuminated with irradiance,G_{GROUND}, and an infinitesimal flat receptor, dR, parallel to it (Figure 2.3). Independently of the nature (direct or diffuse) of the incident radiation on the reflector, the rear surface of the receptor becomes isotropically illuminated with irradiance G_{REAR} equal to

$$G_{\mathrm{REAR}} = \rho G_{\mathrm{GROUND}} \tag{1}$$

being ρ the albedo of the reflector. The contribution of a reflector segment L_1L_2 to this irradiance, G_{REAR}^{L12} is given by

$$G_{\mathrm{REAR}}^{L12} = \int_{\phi_1}^{\phi_2} c \times \cos\theta d\theta = c \times \sin\theta|_{\phi_1}^{\phi_2} = c \times (\sin\phi_2 - \sin\phi_1) \tag{2}$$

where *c* is the 2D radiance intensity (radiant flux emitted per unit angle) and $(\sin\phi_2 - \sin\phi_1)$ is the 2D view factor from the segment L_1L_2 to dR. The integral over the whole reflector $\phi_2 = \frac{\pi}{2}$; $\phi_1 = -\frac{\pi}{2}$ must be equal to G_{REAR}, hence:

$$c = \rho G_{\mathrm{GROUND}}/2 \tag{3}$$

On the other hand, if the infinitesimal receptor is not parallel to the reflector but forms an angle β, the irradiance is the same but the view factor changes. Now, the contribution of the segment L_1L_2 to the irradiance at the receptor, $G(\beta)_{\mathrm{REAR}}^{L12}$ is given by

$$G(\beta)_{\mathrm{REAR}}^{L12} = c \times [\sin(\phi_2 - \beta) - \sin(\phi_1 - \beta)] \tag{4}$$

In turn, establishing the origin of coordinates at the projection of dR on the reflector

$$\phi_1 = \operatorname{atan}\left(\frac{L_1}{H}\right) \quad and \quad \phi_2 = \operatorname{atan}\left(\frac{L_2}{H}\right) \tag{5}$$

where H is the height of dR.

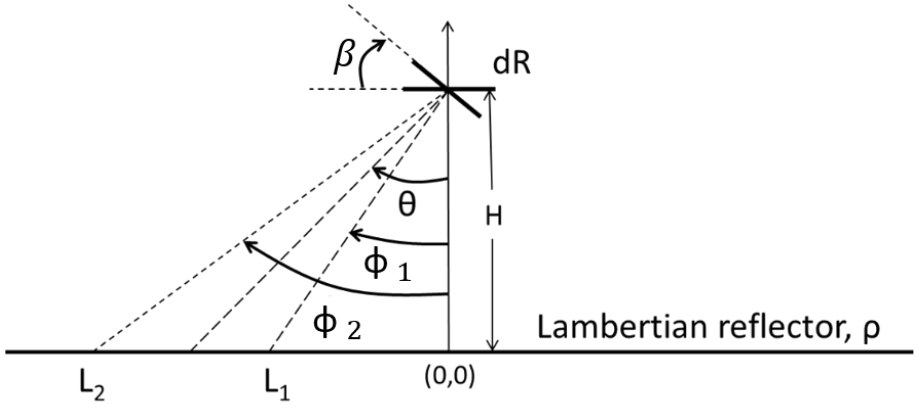


Figure 2.3. Geometry of the view factor from the segment L_1L_2 to a surface element dR.

These equations can be extended to calculate the contribution of the ground to the rear irradiance, $G_{\mathrm{REAR}}^{\mathrm{GROUND}}$, which is given by the sum of the contributions from all of the individual basic patterns described above (each composed by the combination of a shaded and an unshaded segment) and seen by the point of concern X_F at the rear side of the PV module. Figure 2.4 helps to explain such calculation for the center of the PV module (X_F=0). The coordinates of the shade cast by the own module, numbered as 0, are

$$S_1^0 \left[\frac{1}{2}cos\beta - \frac{H - \frac{1}{2}sin\beta}{tan\gamma_S'}; 0\right] \quad and \quad S_2^0 \left[-\frac{1}{2}cos\beta - \frac{H + \frac{1}{2}sin\beta}{tan\gamma_S'}; 0\right] \tag{6}$$

Because of the periodicity of the shade pattern, the coordinates of shade N are given by

$$S_1^N \left[\frac{1}{2}cos\beta - \frac{H-\frac{1}{2}sin\beta}{tan\gamma_S'} + NL; 0\right] \; and \; S_2^N \left[-\frac{1}{2}cos\beta - \frac{H+\frac{1}{2}sin\beta}{tan\gamma_S'} + NL; 0\right] \quad (7)$$

where N is a positive or negative integer. $G_{\mathrm{REAR}}^{\mathrm{GROUND}}$ is calculated as the sum of the contributions corresponding to all segments inside the field of view defined by the extreme angles given by

$$\phi_{E1} = \frac{\pi}{2} - \beta \qquad and \qquad \phi_{E2} = \mathrm{atan}\left[\frac{\left(L - \frac{1}{2}cos\beta\right)}{\frac{1}{2}sin\beta}\right] \quad (8)$$

and considering that G^{GROUND} is composed by three different components: a direct, B_{GROUND}, a circumsolar diffuse, $D_{\mathrm{CIR,GROUND}}$, and an isotropic diffuse, $D_{\mathrm{ISO,GROUND}}$. In this work, we assume that unshaded and shaded segments are illuminated by G_{GROUND} and $D_{\mathrm{ISO,GROUND}}$, respectively. In case of somewhat transparent PV arrays (spaced cells or modules), the incident irradiance on shaded segments also includes a direct and a circumsolar component, both weighted by the transparency factor, F_{T}, i.e., the ratio between uncovered and total areas of the row. That is:

$$G_{\mathrm{UNSHADED}} = G_{\mathrm{GROUND}}$$
$$G_{\mathrm{SHADED}} = D_{\mathrm{ISO,GROUND}} + \left(D_{\mathrm{CIR,GROUND}} + B_{\mathrm{GROUND}}\right) x \, F_{\mathrm{T}} \quad (9)$$

Note that when the PV modules become parallel to the ground, the number of viewed segments is infinite. A simple solution to the consequent calculation problem lies in slightly restricting the view field, for example, from -89º to 89º. The corresponding error is negligible, even more when the angle correction factors are applied (Martin & Ruiz, 2005). It must be noted that considering that every ground segment is uniformly illuminated is a simplification. In fact, $D_{\mathrm{ISO,GROUND}}$ should be affected by the shading of the row, which implies a different view factor of the sky for each point on the ground. The diffuse irradiance is, indeed, not uniformly distributed on the ground. However, the relative weight of this component in the total (front plus rear) in-plane irradiance is generally low (the error associated to this assumption is further discussed in section 2.2.3), so the error derived from such non-uniformity in terms of energy yield must be much lower.

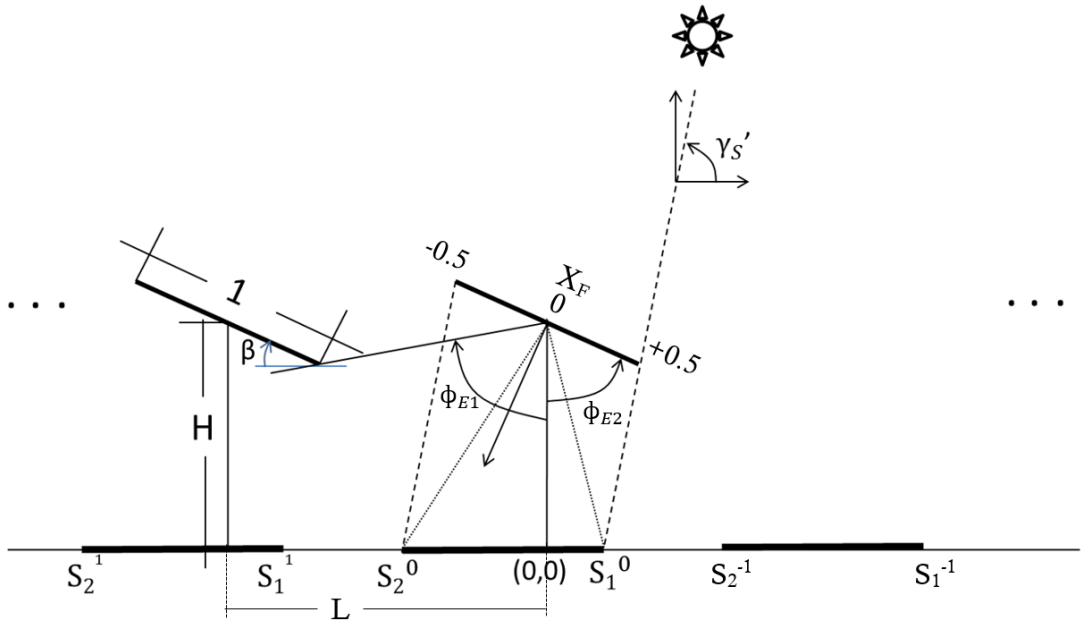


Figure 2.4. Limit angles of the view field from a rear point of a PV array.

More often, the term *albedo* refers to a ratio (upwelling/downwelling) of *broadband* irradiances or visible irradiances(Gueymard et al., 2019; LG Electronics Inc, 2019). However, where PV devices are concerned it is important to consider their angular and spectral responses. On the one hand, leveling rays with an angle of incidence greater than 60º are strongly reflected by a module. On the other hand, depending on the color of the ground, reflection can change the spectral distribution of irradiance, which in turns affects the power output (Brennan et al., 2014).

2.2.2 Other rear irradiance components

Besides the ground reflected component, $G_{\mathrm{REAR}}^{\mathrm{GROUND}}$, the rear side of a rack-mounted module receives also irradiance reflected by the rear row, $G_{\mathrm{REAR}}^{\mathrm{ROW}}$, and from a portion of the sky, $G_{\mathrm{REAR}}^{\mathrm{SKY}}$, as depicted in Figure 2.5. Hence, the total rear irradiance, G_{REAR}, is calculated as:

$$G_{\mathrm{REAR}} = G_{\mathrm{REAR}}^{\mathrm{GROUND}} + G_{\mathrm{REAR}}^{\mathrm{ROW}} + G_{\mathrm{REAR}}^{\mathrm{SKY}} \quad (10)$$

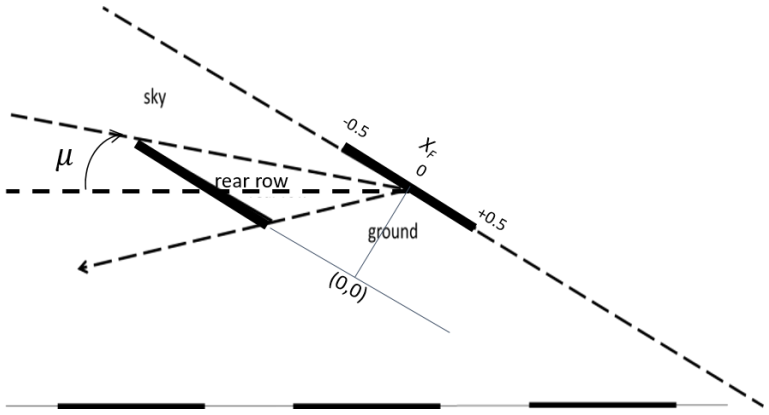


Figure 2.5. Ground, rear row and sky contributions to the rear irradiance.

The sky contribution, $G_{\mathrm{REAR}}^{\mathrm{SKY}}$, comes from direct irradiation ($B_{\mathrm{REAR}}^{\mathrm{SKY}}$) at the beginning and end of some days of the year (typically only in static structures) and from diffuse irradiation ($D_{\mathrm{REAR}}^{\mathrm{SKY}}$). The corresponding equations are:

$$G_{\mathrm{REAR}}^{\mathrm{SKY}} = B_{\mathrm{REAR}}^{\mathrm{SKY}} + D_{\mathrm{REAR}}^{\mathrm{SKY}}$$
$$D_{\mathrm{REAR}}^{\mathrm{SKY}} = \frac{1}{2}\, D_{\mathrm{ISO}}^{\mathrm{GROUND}}(1-k_1)(\cos\mu - \cos\beta) \qquad (11)$$

where μ is the angle of the top edge of the rear row with the horizontal from X_F. At the center (X_F=0) it can be calculated as:

$$\mu = atan\ \left(\frac{\frac{1}{2}\cdot\sin\beta}{L+\frac{1}{2}\cdot\cos\beta}\right) \qquad (12)$$

Both $B_{\mathrm{REAR}}^{\mathrm{SKY}}$ and $D_{\mathrm{REAR}}^{\mathrm{SKY}}$, as well as $G_{\mathrm{REAR}}^{\mathrm{GROUND}}$, and $G_{\mathrm{REAR}}^{\mathrm{ROW}}$, are corrected by the angle of incidence as explained in (Martin & Ruiz, 2005).

The irradiance reflected by the rear row is also calculated based on a view factor. Here, the receptor is always parallel to the reflector, so --see eq. (2) and (3):

$$G_{\mathrm{REAR}}^{\mathrm{ROW}} = c \times [\sin(\phi_2) - \sin(\phi_1)] \qquad (13)$$

where $(\sin\phi_2 - \sin\phi_1)$ is the 2D view factor from the rear row to the center of the rear side of the row, and c is the radiance:

$$c = \rho G_{\mathrm{FRONT}}/2 \qquad (14)$$

being G_{FRONT} the irradiance on the front side of the row, and ρ value corresponds in this case to the reflectance of the module glass (typically around 2.5% in an anti-reflective

treated glass), assuming that it is a lambertian reflector. Establishing the origin of coordinates at the projection of the surface element dR on the rear row plane as shown in Figure 2.3,

$$\phi_1 = \operatorname{atan}\left(\frac{L \cdot \cos\beta + 0.5}{L \cdot \sin\beta}\right) \quad and \quad \phi_2 = \operatorname{atan}\left(\frac{L \cdot \cos\beta - 0.5}{L \cdot \sin\beta}\right) \tag{15}$$

2.2.3 Non-uniformity

Equations (4) to (15) are only valid for the central point of the row. Equations for any other point are easily deduced in an analogous way. This is useful to analyze the non-uniformity of G_{REAR}, the irradiance on the rear side of the row. The view factor from the ground to the calculation point decreases as this point moves from the bottom to the upper edge. Consequently, G_{REAR} calculated at each point is not constant. It depends more on a larger view factor from the unshaded ground segments. With the sun at the position shown in Figure 4, the maximum value of G_{REAR} occurs at the bottom edge of the row (X_F=0.5) because this point has a larger view factor especially from the nearest unshaded segment (S_1^0-S_2^{-1}), but the minimum value of G_{REAR} is located around the midpoint of the row because the upper edge has a larger view factor from the nearest unshaded segment (S_2^0-S_1^1) than the center of the row.

Non-uniformity of G_{REAR} can be quantified by the irradiance non-uniformity index (Deline et al., 2016), *GNU*, as:

$$GNU = \frac{G_{MAX} - G_{MIN}}{G_{MAX} + G_{MIN}} \tag{16}$$

where G_{MAX} and G_{MIN} are, respectively, the maximum and minimum values of irradiance along the rear side of the row.

As a representative example of static PV plants, we have simulated the G_{REAR} distribution in Madrid (40.3877º N, -3.6298º W) for PV arrays characterized by β=30º, H=0.8 (2.5 m height) and L=2 (6.2 m length), south-oriented (this set of values can be found in some examples of the current market of static-structure monofacial PV plants). Simulations have been performed for 21 points (at X_F position) equally distributed between both edges of the back-side row. X_F=-0.5 corresponds to the top edge and X_F=+0.5 to the bottom edge of the row. The synthetic radiation series used as input have been generated from daily average data provided by PVGIS (Aguiar & Collares-Pereira,

1992). Figure 2.6-a shows the values of G_{REAR} at noon for those 21 points throughout the year, and Figure 2.6-b adds details for three representative days: the two solstices and the equinox. Note that, in summer, the minimum value of the rear irradiance is near the center of the row. Therefore, measuring irradiance at this point will underestimate G_{REAR}, as we discuss below.

This simulation exercise has also been extended to calculate the *GNU* distribution throughout the year, which is depicted in Figure 2.6-c and Figure 2.6-d. The magnitude of *GNU* varies greatly throughout the year. *GNU* reaches its maximum intraday value when solar radiation is highest throughout most of the year. The maximum and average values are GNU_{MAX}=0.34 and $\overline{GNU}$=0.13, respectively, and the *GNU* average weighted by G_{REAR} at the center of the row is $\overline{WGNU}$=0.15. Note that weighting by the irradiance gives each value a relative importance in energy yield terms.

Non-uniformity of G_{REAR} rises two issues of practical relevance. The first one concerns mismatch losses due to the differences in the generated current. Estimating these losses is an open question today. Hence, trying to shed some light on this question, we also consider a current non-uniformity index, *INU*. Assuming that the generated current is directly proportional to the sum of the front and rear irradiances weighted by the respective efficiencies, the *INU* is calculated as:

$$INU = \frac{\varphi_I (G_{\mathrm{MAX}} - G_{\mathrm{MIN}})}{2G_{FRONT} + \varphi_I (G_{\mathrm{MAX}} + G_{\mathrm{MIN}})} \tag{17}$$

where

$$\varphi_I = \frac{I^*_{\mathrm{SC,REAR}}}{I^*_{\mathrm{SC,FRONT}}} \tag{18}$$

is the bifacial short-circuit current coefficient of the PV module defined in the technical specification IEC TS 60904-1-2:2019, i.e., the ratio between the Standard Test Conditions, STC, short-circuit current of the rear-side to the STC short-circuit current of the front-side of the concerned PV modules, $I^*_{\mathrm{SC,REAR}}$ and $I^*_{\mathrm{SC,FRONT}}$, respectively. *INU* can provide some insight about power losses. Note that mismatch losses depend not only on the here concerned non-uniformity of G_{REAR} but also on the electrical configuration of the PV array (number of modules in the row width, portrait or landscape mounting, and series and parallel associations) and on the shading cast onto the back of the modules by the support structures, torque tubes, etc. The estimation of these losses is an open question today.

Current available studies (Lopez-Garcia et al., 2019; Bailey & Jaubert, 2018; Buß et al., 2018; Pelaez, Deline, Stein, et al., 2019) suggests that practical mismatch losses are rather low, typically below 1%. We currently do not have a model capable of quantifying power losses from *INU* values. However, simulations show that the *INU* values are typically one order of magnitude smaller than *GNU* values, which is coherent with such low mismatch losses. Resuming the example, the maximum and average values of this static-structure PV plant are INU_{MAX}= 0.047, $\overline{INU}$= 0.016 and $\overline{WINU}$= 0.018. Note that the INU value is relative to total irradiance, while the GNU is calculated relative to rear irradiance. In this example, the ratio of rear to total irradiance is about 0.08.

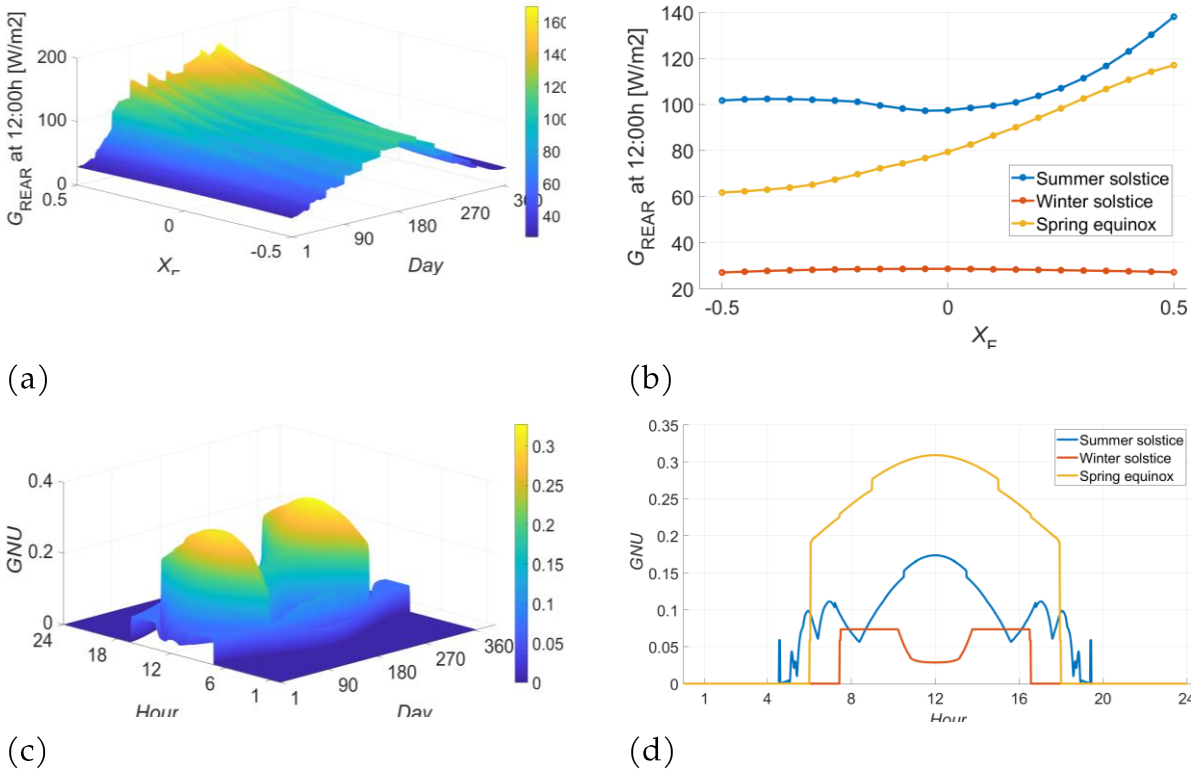


Figure 2.6. Simulated distributions of G_{REAR} along a row (X_F is -0.5 for its top edge and +0.5 for its bottom edge) for a static PV plant located in Madrid (a) at noon throughout the year (b) at noon of the two solstices and spring equinox (c) GNU throughout the year (d) GNU along the two solstices and spring equinox.

Figure 2.7 shows, in this case, the view factor from unshaded ground segments (VF_{NS}) and view factor from shaded ground segments (VF_S) to the center point of the rear side of the row throughout the year (Figure 2.7-a and Figure 2.7-c, respectively) and throughout the two solstices and spring equinox (Figure 2.7-b and Figure 2.7-d,

respectively) are exposed. The sum of both view factors is equal to 1.72 which corresponds to the view factor from the whole view field --its limits given by equation (8). Note that the maximum value of the sum of both VF_{NS} and VF_S is equal to 2 (in case of the maximum 180º view field from the whole-ground segment). Both view factors are constant values in equinox days, as expected. From the spring equinox to the autumn equinox the maximum value of VF_{NS} is reached when the sun is positioned in the true east and true west, respectively, as there is a non-shaded segment under the collector. In winter, the ground is completely shaded (VF_{NS}=0) except for the central hours of the day.

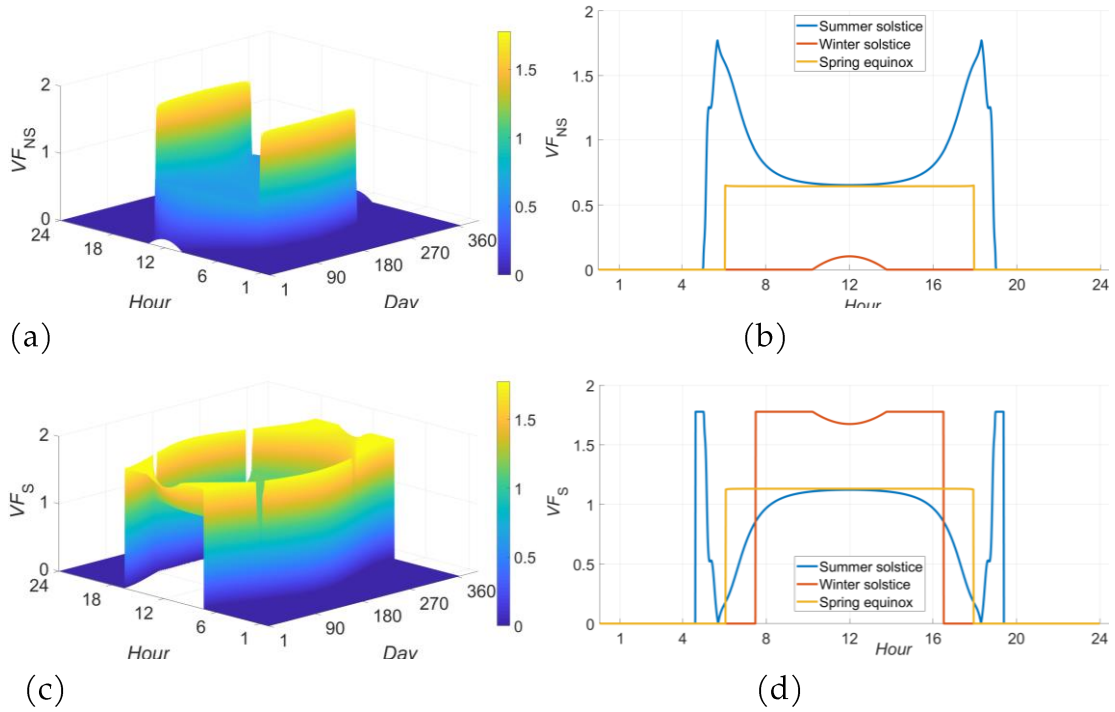


Figure 2.7. View factor from unshaded segments, VF_{NS}, to the center point of the row (a) throughout the year (b) throughout the two solstices and spring equinox. View factor from shaded segments, VF_S, to the center point of the row (c) throughout the year (d) throughout both solstices and spring equinox.

As a representative example of tracking PV plants, Figure 2.8 presents the results of a new simulation at the same location, using the same synthetic radiation series as input data, but this time for a horizontal north-south single-axis tracking PV plant characterized by H=0.8 and L=3. Note that, in case of rows whose section includes a single portrait-

mounted module of 2 m in length, this length corresponds to the cross width of the row and means the height of the axis is 1.6 m and the pitch is 6 m, which is a commonly found configuration in commercial PV plants. *GNU* has a relative minimum every day at noon. It reaches its maximum intraday value when the solar radiation is relatively low compared to the central hours of the day. Unlike the case of static structures, the daily *GNU* is fairly constant throughout the year. The maximum and average values are GNU_{MAX}=0.40, $\overline{GNU}$=0.14 and $\overline{WGNU}$=0.17. Corresponding values of *INU* are INU_{MAX}=0.032, $\overline{INU}$=0.015 and $\overline{WINU}$=0.019. Again, the *INU* values are one order of magnitude smaller than *GNU* values.

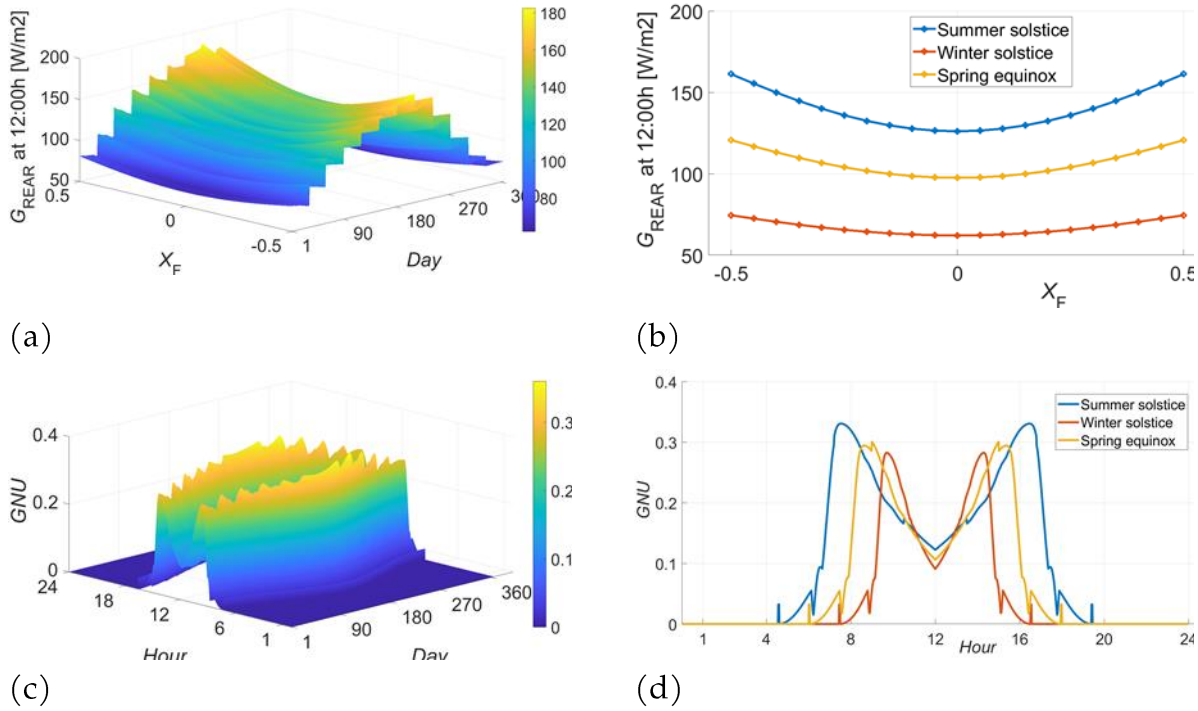


Figure 2.8. Simulated distributions of G_{REAR} along a row (X_F is -0.5 for its top edge and +0.5 for its bottom edge) for a horizontal single-axis tracking PV plant located in Madrid and characterized by H=0.8 and L=3 (a) at noon throughout the year (b) at noon of the two solstices and spring equinox (c) GNU throughout the year (d) GNU along the two solstices and spring equinox.

The non-uniformity of G_{REAR} also raises the issue of the representativeness of the G_{REAR} value observed at a given point, which is of practical relevance for the estimation of energy yield. The center of the row is just the point receiving the lowest G_{REAR} for both

the trackers and the static-structure cases throughout the period of greatest solar radiation, and many simulation exercises have led us to suspect this is a rather general situation. The saddle-shaped pattern in Figure 2.6-a and Figure 2.7-a indicates that energy yield estimates based on G_{REAR} at the center of the row must be somewhat pessimistic. This is particularly important when these estimates are part of the technical due diligence associated with the bankability of PV plants. Section 2.5 pays further attention to this issue.

2.3 Electrical and thermal models

We rely on a MPP (Maximum Power Point) model for calculating the DC power delivered by a PV plant, P_{MPP}, and on a NOCT (Nominal Operating Cell Temperature) model for calculating the PV module temperature, T_C.

$$P_{MPP} = P^* G' (1 + \gamma T'_C) \frac{\eta(G)}{\eta^*} \tag{19}$$

$$\frac{\eta(G)}{\eta^*} = (a_1 + a_2 G' + a_3 ln G') \tag{20}$$

with

$$G' = \frac{G}{G^*} \; ; \; T'_C = T_C - T_C^* \tag{21}$$

where γ is the power temperature coefficient, the asterisk* refers to STC conditions; and a_1, a_2 and a_3 are empirically adjusted parameters for considering the irradiance-dependent efficiency (de la Parra et al., 2017). The factor $(1 + \gamma T'_C)$ corrects for the effect of temperature. The factor $(\eta(G)/\eta^*)$ corrects for the effect of irradiance. The irradiance value considered in these equations for monofacial plants is just the frontal one, $G = G_{\text{FRONT}}$. Now, for bifacial PV plants, we simply add G_{REAR} to G_{FRONT}, and weights G_{REAR} by the power bifaciality coefficient, φ_P. That is:

$$G = G_{\text{FRONT}}(1 + \varphi_P \times GBR) \tag{22}$$

where

$$\varphi_P = \frac{P^*_{\text{REAR}}}{P^*_{\text{FRONT}}} \tag{23}$$

and

$$GBR = \frac{G_{\mathrm{REAR}}}{G_{\mathrm{FRONT}}} \tag{24}$$

GBR is the so-called irradiance bifacial ratio. It should be stressed that all the irradiance values in equations (19) to (24) must be "effective" values, G^{ef}, i.e. corrected by the angular and spectral responses of the PV modules. Models for such corrections are well stablished in the available literature (Moretón et al., 2017; Martin & Ruiz, 2005) will not be discussed here any further.

Besides, we rely on a NOCT (Nominal Operating Cell Temperature) model for calculating the PV module temperature, T_{C}.

$$T_C = T_A + \mathrm{C_T} G \tag{25}$$

where T_{A} is the ambient temperature and $\mathrm{C_T}$ the variation coefficient of T_{C} with *G*, which is related to the *NOCT* characteristic of the PV module:

$$\mathrm{C_T} = \frac{NOCT - 20^o C}{800\ W/m^2} \times 0.9 \tag{26}$$

NOCT is defined under the condition of a wind speed below 1 m/s, which is lower than that normally observed in fields. 0.9 is just an empirical factor to approximate the cooling effect of real winds when wind information is not available. It has been adjusted in accordance with IES-UPM experimental T_{C} observations in real PV plants, aiming at concordance with the observed yearly thermal losses (Moretón, 2016). Now, for bifacial PV plants, we simply assume that solar cell heating caused by irradiance is independent of the incident side. That leads to:

$$T_C = T_A + \mathrm{C_T}(G_{\mathrm{FRONT}} + G_{\mathrm{REAR}}) \tag{27}$$

This particular model selection aims to facilitate the comparison between the actual operational data (often, in terms of *G*, T_{C} and P_{MPP}) and the initial estimates, and has been experimentally justified for standard monofacial PV plants in past work (de la Parra et al., 2017). The estimation of T_{C} in bifacial modules is an open question that is receiving the attention of several authors (Lamers et al., 2018; Lopez-Garcia et al., 2018; H. Wang et al., 2020) with, in some cases, contradictory results. We have opted to consider the sum of the front and rear irradiances as input to the NOCT model --Eq. (25) and (27), because

we think this is consistent with the fact that the near-white rear of white backsheet modules tend to reflect G_{REAR} while near-black cells in bifacial modules tend to absorb it.

2.4 Performance ratio

The *PR* concept plays a key role in due diligence procedures, mainly because it is a key metric for acceptance/rejection decisions based on on-site Commissioning tests. The classic *PR* as defined in IEC 61724:1998 is given by

$$PR = \frac{E_{AC}}{P^{*}_{\mathrm{FRONT}} \int_{T} G' dt} \tag{28}$$

where E_{AC} is the energy output and the integral is the in-plane irradiation (in equivalent hours) both over the considered time span T. In practice, they are calculated as sums of the discrete power and irradiance values, respectively, recorded in the operation database, multiplied by the recording time step (hourly or sub-hourly).

Where bifacial PV plants are concerned, the *PR* can be referred to only the front irradiation ($G = G_{\mathrm{FRONT}}$) or to the sum of front and rear irradiations, the latter weighted by the bifacial power coefficient of the modules --*G* as given per eq. (22). The "*PR* front", PR_{F} is often used not only for monofacial PV plants but also for bifacial ones (Ayala et al., 2018; Singh et al., 2012) mainly because it is conservative of standard practice on conventional monofacial PV plants. However, its physical meaning is doubtful, because it disregards the rear irradiation contribution to the energy yield. Instead, the "*PR* bifacial", PR_{B}, allows assessing the technical quality of the PV plant itself, irrespectively of the ground reflectance conditions. This is at the cost of measuring two irradiations instead of just one. Nevertheless, this has been the preferred option, especially for Engineering-Procurement-Commissioning (EPC) companies, in some due diligences of the IES-UPM experience.

2.5 Experimental observations

2.5.1 Experimental set-up

Figure 2.9 shows front and rear views of the bifacial PV plant located at the IES-UPM roof, which is routinely injecting energy into the grid since May 14th 2019, with the aim of adding to the set of reference bifacial facilities of European institutions (Bonilla-Castro et al., 2018; Gracia-Amillo et al., 2019; Reise et al., 2018; H. Nussbaumer et al., 2020). PV modules are TRINA DUOMAX TWIN TSM (Nominal values: P^*_{FRONT}=345 W –positive tolerance up to +5 W–and φ_{P}=0.70; Dimensions: 2 m x 1 m). Before installation, both sides of all the modules have been independently measured at the IES-UPM solar simulator, in accordance with IEC-TS 60904-1-2. Besides, 4 modules have been measured again after a Sun exposition of more than 60 kWh/m^2, to determine their Light Induced Degradation, LID. Average testing result values (P^*_{FRONT}=353 W, LID=2% and φ_{P}=0.69) essentially confirmed the in-plate data. The modules are placed in landscape position, and the PV array table is made up of 3 (width) x 7 (length) modules. The PV array is a single string of 19 modules (nominal P^*_{FRONT}= 6.6 kW). The PV modules are connected to each other by means of "T" shaped quick connectors, which allow monitoring of the operating voltage of all the modules. The PV array delivers power to a 10 kW three-phase transformed-based inverter with a measured European efficiency of 91.6%.

Besides, a bifacial reference module (constitution and operation described in the Annex A) is placed at the center and an inactive module completes the surface of the rectangle. The geometry is defined by β=20º, H=0.47 (1.4 m), south oriented. The ground under the table is covered by white bricks (ρ=0.45). The rest of the ground is covered by gravel stone (ρ=0.22). A strip of about 4 m wide is from time to time (approximately every two months) coated with quicklime (ρ evolves from 0.6 at the beginning to 0.25 at the end). This ground arrangement provides an irradiance bifacial ratio above 20%, which is rather larger than expected in most commercial PV systems, but adequate for observing some bifaciality related phenomena. The reference module placed at the center measures G_{FRONT}, G_{REAR} and T_{C}. Besides, since October 5th 2019, three reference cells measure G_{REAR} at the center and at two edges (upper-right and lower-left, rear view) of the PV array. P_{DC} is also measured with standard electrical instruments. Values are periodically recorded every 5 minutes.

Because of both edge effects and non-homogenous albedo, this PV array does not fit totally with the 2D G_{REAR} model considered in this work. However, it is still useful to analyze the validity of the electrical model described by equations (19) to (24) and to analyze the representativeness of the G_{REAR} value observed in the center and of the average of the three observations, in the center and in the edges.



(a) (b)

Figure 2.9. Front (a) and rear (b) views of the bifacial PV plant operating at the IES-UPM roof.

Figure 2.10-a presents the evolution throughout October 5th 2019, a clear day, of G_{REAR} measured at the center and at the two edges of the PV array. Corresponding *GNU* is also depicted. G_{REAR} reaches 250 W/m^2 in the lower-left edge (G_{FRONT} reaches 825 W/m^2 at the same time) and *GNU* remains relatively constant throughout the day at around 0.45. These Figures are indicative of rather large and non-uniform rear-irradiance. However, the corresponding *INU* values are always kept below 0.08, which can help to explain why we never observed significant anomalies in the distribution of the operating voltages of the modules. This is also coherent with low mismatch losses reported by other authors, as mentioned above. Figure 2.10-b presents the same parameters but for October 22th 2019, a cloudy day. As expected, rear irradiance becomes lower ($G_{REAR} \leq 50$ W/m^2) and more uniform ($GNU \leq 0.15$).

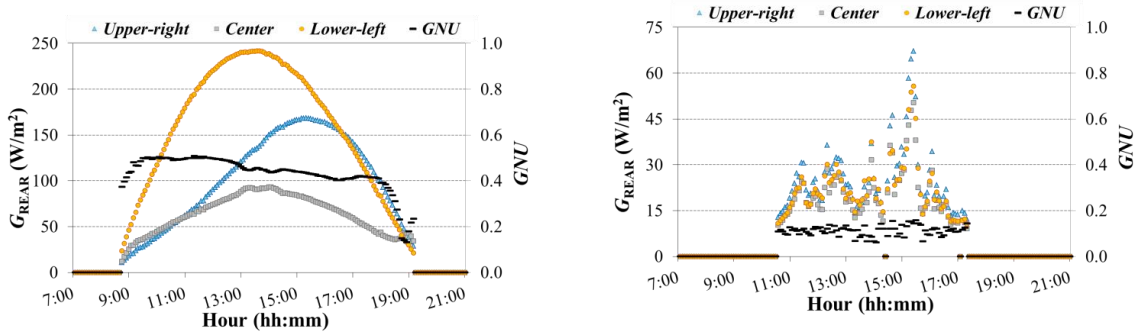
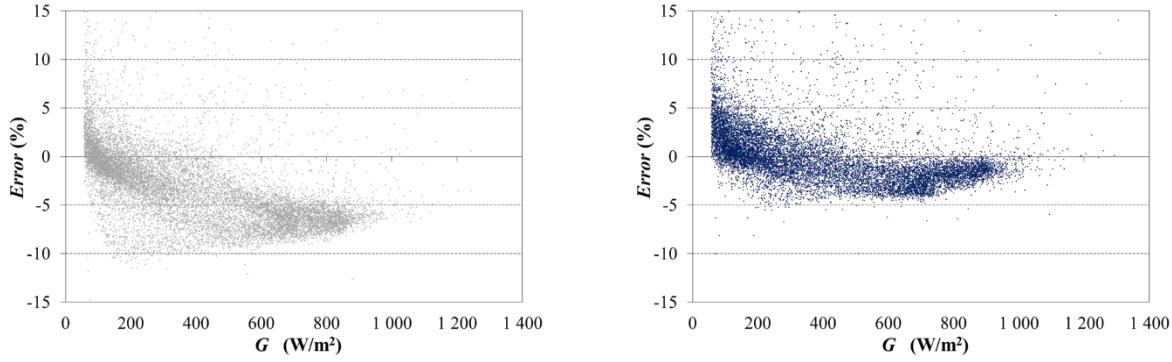


Figure 2.10. Daily evolution of the rear irradiance values measured at the center and in two edges of the PV array throughout (a) a clear day (October 5th 2019), and (b) a cloudy day (November 22th 2019). Note that the range of left-'y'-axis is different in the graphics.

2.5.2 Errors in P_{DC} estimates

Figure 2.11 shows the errors of the P_{DC} estimates from equations (19) (21) and (22) with respect to the measured values. The left and right sides of the figure correspond to errors when using $G_{REAR,CENTER}$ and $G_{REAR,AVERAGE}$, respectively. The statistical parameters corresponding to these errors, and to the errors weighted by the respective G_{REAR} in each case, are presented in Table 2.1. Figure 2.11-a and Figure 2.11-d plot the errors versus the total effective irradiance (as per equation (22)); Figure 2.11-b and Figure 2.11-e plot the errors versus *GNU* (as derived from the three reference cells at the rear of the PV array), and Figure 2.11-c and Figure 2.11-f present the error histograms. The module datasheet provides the value γ=–0.39%/°C, and we have adjusted the irradiance coefficients value a_1=1.1, a_2=-0.1 and a_3=0.05, using the data of a clear day. The analyzed period is from October 5th 2019 to March 9th 2020. It can be observed that errors are greatly reduced when using $G_{REAR,AVERAGE}$ instead of $G_{REAR,CENTER}$.



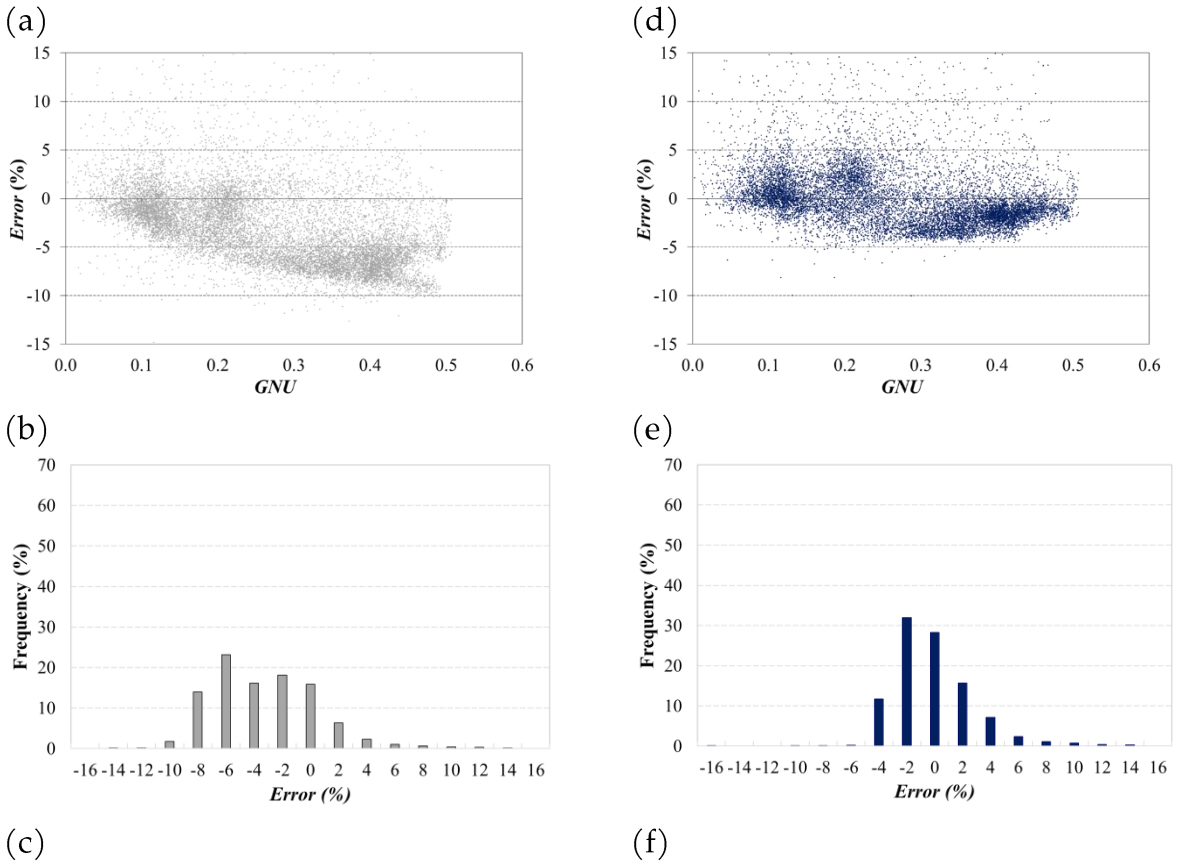


Figure 2.11. Errors in P_{DC} estimates. The left and right columns correspond to errors when using $G_{REAR,CENTER}$ and $G_{REAR,AVERAGE}$, respectively. The upper row plots errors versus irradiance. The middle row plots errors versus GNU, and the lower row presents the error histograms.

Table 2.1. Statistical parameters of errors in P_{DC} estimates in %.

		Mean	Standard deviation	Median
$G_{REAR,CENTER}$	errors	--1.8	2.3	-1.1
	weighted	-4.5	5.7	-2.8
$G_{REAR,AVERAGE}$	errors	-0.1	2.9	-0.7
	weighted	-0.8	4.0	-0.5

2.5.3 Performance and PR values

Above referred real module characteristics adhering to nominal values, sunny location, higher than usual albedo, and low mismatch losses prelude a good energy performance. In fact, the AC energy yield of the PV array for the 10-month period covered by this work has been 1,257 kWh per kW_p. Table 2.2 presents the mean and standard deviation values of the weekly front and rear irradiations, $G_{FRONT,w}$, $G_{REAR,CENTER,w}$ and $G_{REAR,AVERAGE,w}$, and of the weekly AC energy. It is worth remembering that a week is a representative period in today PV engineering practices. For example, *PR* Commissioning Tests are often performed in weekly terms (IEA-PVPS Task13 2014b; 2014a). The following comments apply:

(c) - PR_F ranges from 0.93 to 1.06. This is very high when compared to typical values for conventional monofacial PV plants. However, this means nothing regarding technical quality. Simply, the PR_F considers the bifacial contribution as free, which is meaningless in reality.

(d)- PR_B solves this lack of meaning. It ranges from 0.82 to 0.93, which is directly comparable with the *PR* of a conventional monofacial plant of similar quality. This is particularly true when considering $G_{REAR,AVERAGE}$.

(e)- The PR_B when considering $G_{REAR,CENTER}$ is about 3 percent points higher that when considering $G_{REAR,AVERAGE}$. This represents another facet of the same issue that leads to simulation underestimates commented in Section 2.3. This time, the consequent practical problem is that a PV plant with real specifications lower than expected can still pass a *PR* test based on $G_{REAR,CENTER}$ whose passing criteria fits the simulated values.

Table 2.2. Statistical parameters of the weekly results of measured AC energy, front and rear (center, and three-points average) irradiations and the corresponding front and bifacial PRs.

	E_{AC} [kWh]	$G_{FRONT,w}$ [kWh/m²]	$G_{REAR,CENTER,w}$ [kWh/m²]	$G_{REAR,AVERAGE,w}$ [kWh/m²]	PR_F	$PR_{B,CENTER}$	$PR_{B,AVERAGE}$
From May 14th 2019 to March 9th 2020 (43 weeks)							

Mean	193	30.0	4.2	N.A.	0.99	0.90	N.A.
Standard deviation	93	15.0	2.1	N.A.	0.04	0.03	N.A.
TOTAL	8,296	1,289.2	179.7	N.A.	0.98	0.89	N.A.
From October 8th 2019 to March 9th 2020 (22 weeks)							
Mean	120	18.1	2.6	3.8	1.01	0.92	0.89
Standard deviation	52	7.7	1.0	1.8	0.03	0.03	0.03
TOTAL	2,648	397.4	58	82.7	1.02	0.92	0.89

2.6 Implementation in SISIFO: bifacial PV performance model

SISIFO is a PV simulation software (freely accessible at https://www.sisifo.info) developed by the IES-UPM under the umbrella of the European projects PVCROPS (European Commission, CORDIS, 2012) and MASLOWATEN (European Commission, CORDIS, 2015). Main models used in SISIFO for irradiance distribution, decomposition, transposition and spectral correction were presented in (Muñoz et al., 2013) and can be found in (Lorenzo, 2010; Hay & McKay, 1985; Perez et al., 1987; Martín & Ruiz, 1999; Lorenzo et al., 2011). SISIFO allows dealing with mutual shading (Martínez-Moreno et al., 2011), different tracking types (Narvarte & Lorenzo, 2008), and both grid-connected and pumping PV systems. Bifacial PV capabilities for static structures and horizontal single-axis trackers are also available since February 27th 2019 following the G_{REAR}, $\underline{P}_{MPP}$ and T_C models described in section 2.3 and the *PR* calculations in section 2.4, and considering large PV generators and, therefore, neglecting edge effects. Since then, 34% of those simulations were on bifacial PV systems. The current free version considers only G_{REAR} at the center of the row. This may lead to somewhat underestimating the energy yield, as commented previously. Besides, mismatching losses due to non-uniform G_{REAR} are disregarded. Future versions will try to improve the treatment of these issues.

This section completes the two representative examples, a static-structure and a horizontal single-axis tracking PV plant, connected to the grid in Madrid, which were introduced in Section 2.2. Yearly solar irradiation, $G_y(0)$=1,794 kWh/m2 and $D_y(0)$=536

kWh/m, and ambient temperature data were obtained from PVGIS. A common ground with ρ=30% (constant value throughout the year), PV modules with φ_P=70%, *NOCT*=45º C, γ=-0.38%/°C, and 1% soiling losses have been considered. Power losses at STC, from the nominal value (i.e., the product of the number of modules by the corresponding in-plate power) to the inverter entry, are 3.6 % (mainly due to effects like LID, PID, temperature mismatching, strings mismatching, or losses in the DC wiring). Self-shading, and its impact on efficiency, has also been considered (Martínez-Moreno et al., 2010). The connection to the grid is accomplished through a transformer-less inverter with a European efficiency of 98.7%, an AC line with 1% losses at STC, and both low-to-medium voltage and medium-to-high voltage transformers. If the reader wishes to reproduce these simulations or to consult additional details, it is possible to do so as the SISIFO tool is available on line.

2.6.1 Static structure

The static-structure PV plant presented above and characterized by β=30º, *H*=0.8 (2.5 m) and *L*=2 (3.1 m), south-oriented, is first evaluated. Table 2.3 summarizes the most relevant annual results and Figure 2.12 depicts a Sankey diagram to further illustrate the distribution of energy losses.

Table 2.3. Results of the simulation for a representative static-structure PV plant.

Irradiations [kWh/m2 per year]		
Horizontal: Global (*GHI*): 1,794 Diffuse (*DHI*): 536	In-plane front: Broadband (G_{FRONT}): 2,044 In-plane rear: Broadband (G_{REAR}): 254	(*GyBR*: 12%)
Specific energy yields [(kWh per kWp and per year]		
Reference (G_{FRONT}+G_{REAR}): 2,298	DC: 1,865 AC: 1,813	
Performance parameters [%]		
Capture losses:	$PR_{F:}$ 88.7	

Front: 7.3	$PR_{B:}$ 81.6
Rear: 37.8	
System losses: 2.3	

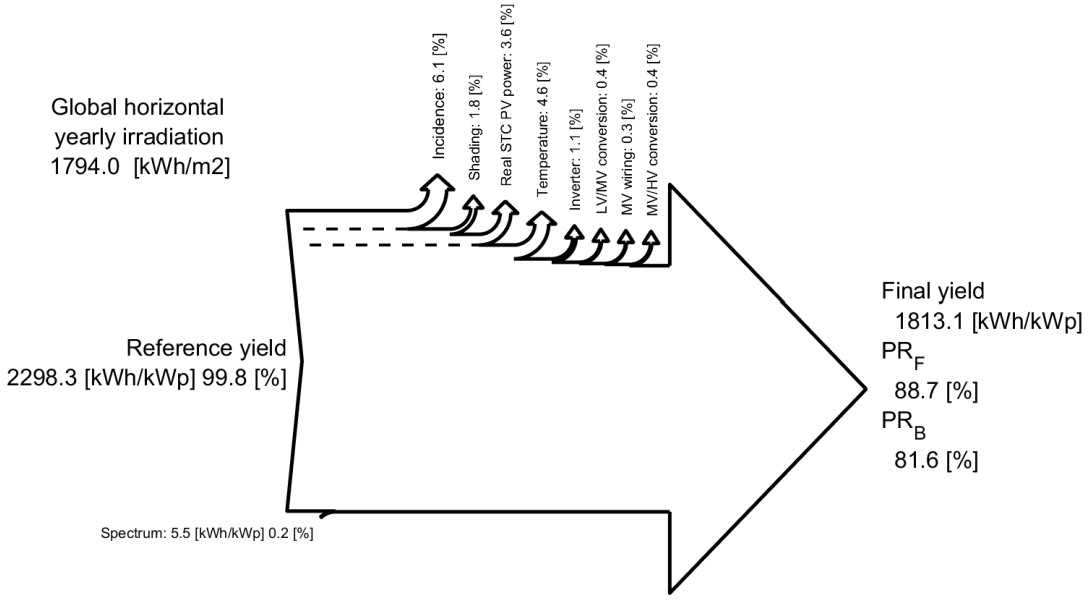


Figure 2.12. Sankey diagram corresponding to a representative bifacial static-structure PV plant.

Different values of the design parameters of the PV plant, H and L, were simulated and the results in terms of yearly irradiation bifacial ratio, G_yBR, can be seen in Figure 2.13. Increased H, or increased L, lead to increased G_yBR.

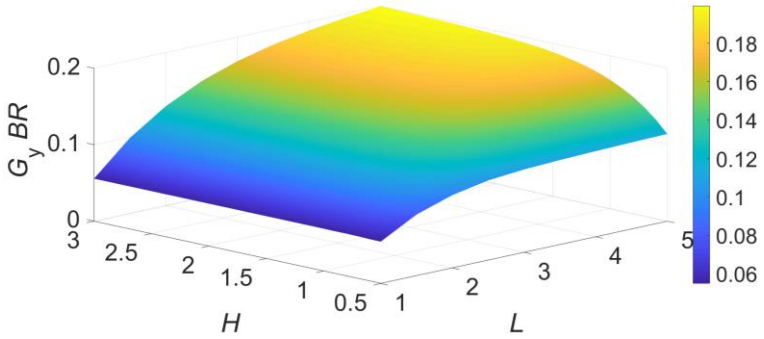


Figure 2.13. Yearly irradiation bifacial ratio, G_yBR, depending on H and L.

As a reference, Table 2.4 includes the improvement ratio of different PV plant designs in relation to the analyzed case. The influence of H is lower than that of L. Compared to the base case, doubling L produces about 5% additional DC energy yield, - a part of it

corresponding to an improvement in DC energy yield from the front side of the PV module due to the shorter actuation time of the backtracking mechanism -, while doubling *H* leads to a very small or negligible DC energy yield gain. Therefore, variations on the support structure and on the geometry design with respect to corresponding setups in traditional monofacial plants are scarcely justified and need detailed cost calculations.

Table 2.4. Yearly in-plane irradiation G_y=G_{FRONT}+G_{REAR} and yearly DC energy yield improvement ratios in relation to the analyzed (H=0.8, L=2) case.

In-plane *Gy* improvement ratio			
	H		
L	0.8	1.6	3
1.5	0.87	0.88	0.88
2	1.00	1.01	1.01
3	1.05	1.07	1.07
5	1.06	1.09	1.10

E_{DC} yield improvement ratio			
	H		
L	0.8	1.6	3
1.5	0.87	0.88	0.88
2	1.00	1.00	1.00
3	1.04	1.05	1.05
5	1.05	1.07	1.08

2.6.2 Horizontal single-axis trackers

For the presented above north-south horizontal single-axis tracking PV plant, with no axis inclination and ±45º back-tracking capability, *H*=0.8 (1.6m) and *L*=3 (6 m) were considered as they probably are the most established values in the current PV plant market. Table 2.5 summarizes the most relevant yearly results and Figure 2.14 depicts a Sankey diagram.

Table 2.5. Yearly results of the simulation for a representative bifacial horizontal one-axis tracking PV plant.

Irradiations [kWh/m2 per year]		
Horizontal: **Global (*GHI*): 1,794** **Diffuse (*DHI*): 536**	In-plane front: Broadband (G_{FRONT}): 2,390 In-plane rear Broadband (G_{REAR}): 265	(*GyBR*: 11%)

Specific energy yields [kWh per kWp and per year]	
Reference ($G_{FRONT}+G_{REAR}$): 2,655	DC: 2,231 AC: 2,171
Performance parameters [%]	
Capture losses: Front: 3.5 Rear: 36.2 System losses: 2.3	 $PR_{F:}$ 90.9 $PR_{B:}$ 84.3

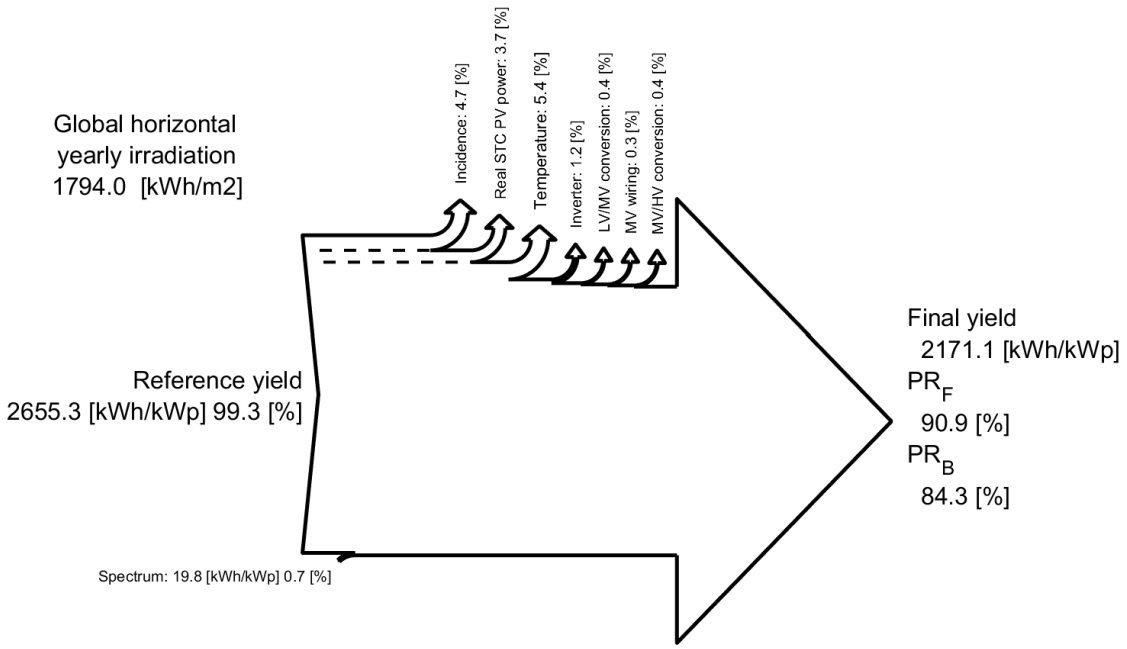


Figure 2.14. Sankey diagram corresponding to a representative bifacial horizontal north-south one-axis tracking PV plant.

Finally, we have varied L and H, and observed its impact on yearly G_yBR (Figure 2.15), and DC energy yield. It is observed that values increase both with the increase of H and L. For H=0.8 and L=3, the DC energy yield is 2,231 kWh per kWp and G_yBR is 0.11. With equal H and L=5, the increase in DC energy yield is less than 5%, and G_yBR only increases to 0.13. Considering L=2, DC energy yield is 7% lower than with L=3 and G_yBR decreases to 0.09.

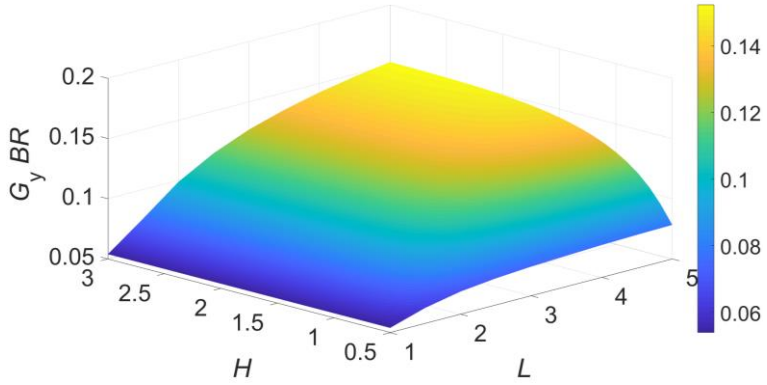


Figure 2.15. Yearly irradiance bifacial ratio, G_yBR, depending on H and L.

As a reference, Table 2.6 shows the improvement ratio of different PV plant designs in relation to the analyzed case. As in the case of static structures, the influence of *H* is lower than that of *L*. Same comments as for the static case also apply.

Table 2.6. Yearly in-plane irradiation $G_y=G_{FRONT}+G_{REAR}$ and yearly DC energy yield improvement ratios in relation to the analyzed (H=0.8, L=3) case.

Effective in-plane G_y improvement ratio			
	H		
L	0.8	1.6	3
2	0.93	0.94	0.94
3	1.00	1.02	1.02
5	1.05	1.07	1.08

E_{DC} yield improvement ratio			
	H		
L	0.8	1.6	3
2	0.93	0.94	0.94
3	1.00	1.01	1.01
5	1.04	1.06	1.06

In this case, 2.3% of the total in-plane irradiance comes from the horizontal diffuse irradiance in shaded segments. Therefore, the non-uniform nature of the latter has little influence on the result.

In both representative cases, results express rather modest *GyBR* and DC energy yield increases (well below 20%), which is in accordance with previously reported work (Chudinzow et al., 2019; Gueymard et al., 2019; LG Electronics Inc, 2019; Pelaez, Deline, Greenberg, et al., 2019; Sun et al., 2018).

2.7 Blind PV modelling intercomparison

By 2022, more simulation tools capable of modelling and estimating the bifacial contribution were available. We then participated in a blind PV performance modelling intercomparison organised by the PV Performance Modelling Collaborative (PVPMC) to allow PV modellers to blindly test their models and modelling capabilities against real system data.

In this intercomparison, the characteristics of fixed-tilt and single-axis tracking PV systems (6 scenarios) in two locations with different climates - Albuquerque (New Mexico) and Roskilde (Denmark) - and hourly experimental values of relevant meteorological data (irradiance, ambient temperature, wind) were provided. Each participant, using a simulation tool of their choice and based on their experience, defined a derating scenario and estimated the plane-of-array irradiance, module temperature and DC electrical power at the inverter input for each proposed PV system. The organiser then compared each expectation with the observed reality.

Some findings of this intercomparison are presented in (Theristis et al., 2022, 2023). In direct relation to the work presented in this thesis, the following conclusions are highlighted:

(a) The error in predicting back irradiance is high. In some cases, it exceeded $\pm$100%. It is worth noting that its influence on the final estimate is small, as the back irradiance is at least one order of magnitude smaller than the front irradiance, in line with the results presented in the previous section.

(b) Several participants use the same commercial tool, PVsyst, and the same models, but the spread of energy yield estimate is ~6% (it was ~33% in a previous intercomparison in 2010).

(c) The participants' derating scenario mostly underpredicts DC energy.

However, there are a number of considerations that may explain or qualify the above conclusions of the inter-comparison:

(a) Only two of the 6 simulated PV systems are bifacial.

(b) The proposed bifacial PV systems are small experimental systems (25.96 kW_p), much smaller than a real PV system. In particular, the participants were asked to estimate the DC power generated by a string in PV systems consisting of 4 parallel strings. Compared to the same string in a PV plant, a higher production would be expected in these small systems due to several effects: 1) higher irradiance (diffuse and/or reflected on the ground) occurs in the rows (or modules) at or near the edges of the PV system, 2) the lower number of strings per inverter leads to lower mismatch losses (wiring, modules) and to more optimal tracking of the maximum power point.

(c) Relevant aspects of the derating scenario, such as soiling or electrical losses, were not specified. Compared to the same string in a PV plant, its cleanliness in an experimental installation is likely to be higher on both sides of the generator.

(d) In both bifacial PV scenarios, the angular response of the module or its response at low irradiance is unknown (its commercial datasheet is provided). In addition, the site (Denmark) is likely to experience snow events (only a monthly average albedo was provided)

(e) It is not known which participants applied a derating scenario tailored to large PV systems, or instead developed an adapted scenario that tried to incorporate some or all of the above effects.

Given the above, it seems reasonable to deduce that those applying a derating scenario and models devised for large PV plants should underestimate the expected output of the proposed experimental systems. This was the case in our involvement with SISIFO using the large PV plant loss scenario and conservative values for angular response, low irradiance response, etc. It should also be noted that the uncertainty of the measurements (irradiance, ...) provided was not taken into account.

2.8 Conclusions

As a contribution to the general history of photovoltaics, a pioneering industrial production and commercial use of bifacial PV modules that took place in Spain from 1984

to 1989 and which gave rise to an early and currently scarcely known bifacial PV modelling episode three decades ago, has been recollected. As far as we know, the "view-factor" concept, imported from traditional heat transfer analysis, which is the basis for many current models, was applied then for the first time.

A view-factor based two-dimensional model for calculating the rear irradiance in large bifacial PV plants has been developed now, and was integrated in SISIFO for static structures and also for horizontal single-axis trackers. The steps for defining such model are, first, idealizing the geometry of a large PV array as a regular disposition of an infinite number of rows of infinite length, second, realizing that the regular disposition of the rows translates into a basic pattern, composed by a shaded and an unshaded segment, which repeats with a period equal to the row-to-row space, and third, calculating the irradiance reflected from the ground by applying the concept of view factor from such segments to a given point of the rear of a row. Two additional irradiance components, the reflected by the rear row and the coming from a portion of the sky, are also considered. That allows calculating the rear irradiance at any point in the row.

Errors in corresponding power estimation derived from the non-uniformities of rear irradiance considering either just a particular point at the center, or the average between that center and two borders, as a representative value of the whole row, have been discussed in the light of ten-month experimental observations in a 6.6 kW_p (in-plate front power) bifacial PV system in routine operation at the IES-UPM roof. Two indexes for respectively characterizing the non-uniformity of the rear irradiance and of the generated current have been introduced. Values of the latter are typically one order of magnitude smaller than values of the former, which is coherent with low mismatch for rear irradiance losses reported by other authors.

A bifacial performance ratio *PR* referred to the sum of front and rear irradiation, the latter weighted by the bifacial power coefficient of the modules has been proposed and integrated in SISIFO. It keeps the meaning of the standard *PR* for conventional monofacial plants, as defined in IEC 61724:1998, and can be interpreted as an indicator of the general technical quality of a bifacial PV plant with values similar to those of a monofacial one. In fact, the IES-UPM PV system described above has produced close to 11 MWh in ten months of operation. When referred to the STC front power that means more than about 1650 kWh per kW, which leads to a PR above 100%. This is much more

than expected from a monofacial PV plant. In contrast, the bifacial *PR* considered here is slightly lower than 90%, which is similar to what can be expected from a good monofacial PV plant if incident irradiation is measured with a PV reference device.

Finally, in order to present what can reasonably be expected when adding the bifacial qualifier, the energy yield for two representative static and tracked PV plants in Madrid has been simulated using SISIFO. In these cases, increasing the structure height is less relevant to improve DC energy yield than increasing the row-to-row spacing. Results express rather modest yearly irradiation and DC energy yield increases (well below 20%), which is in accordance with previously reported work. A recent Photovoltaics Institute Berlin white paper (Podlowski, 2019) says "*There are many publications where energy gains with bifacial modules of more than 30% are claimed. Be careful! A lot of these studies are from the early years of bifacial PV research and have been conducted under circumstances which are not realistic for commercial systems.*" We agree.

Chapter 3

SINGLE-AXIS TRACKING AND BIFACIAL GAIN ON SLOPING TERRAIN

"Everything should be made as simple as possible, but not simpler." (Albert Einstein)

3.1 Introduction

Existing PV simulation software has built-in single-axis tracking and backtracking functionality typically assuming that the tracker axes are contained within a horizontal plane (Kankiewicz, 2021). This has often been a valid assumption for real-world systems until now. However, as the PV market grows, single-axis trackers are beginning to settle in sloping terrain. A recent report on solar financing (kWh Analytics, 2021) reveals that, on average, solar projects underperform their target production (P50) estimates by 6.3%, and points out that 'uneven terrain often causes losses for north-south aligned single-axis trackers on east-west slopes' as a common factor contributing to the observed energy shortfall. This motivates the enhancement of PV software capabilities to overcome the horizontal constraint.

This mainly requires modifications in the calculation of two different aspects: the backtracking geometry and the ground shading scenes needed to estimate the rear irradiance, G_{REAR}, in the case of bifacial generators. In addition, slopes affect the horizon which, in turn, affects the components of the front irradiance, G_{FRONT}. Slope-aware backtracking has been explored by (Schneider, 2012), (Nascimento et al., 2015), and

(Anderson & Mikofski, 2020), so backtracking formulations that consider both horizontal and vertical row offsets are available. However, to the best of our knowledge, such formulations have never been incorporated into available PV energy yield simulation software. Current PV software has relied on 2D to define the shading scenes required for G_{REAR} calculations and seems to be moving towards 3D scenes to deal with complex terrains. The 3D approach is likely to entail a significant increase in mathematical complexity, input information and computing time. This leads us to deal with sloping terrain while still relying on a 2D scene. This has been implemented in SISIFO, which allows to deal with sloping terrain since June 2022.

This thesis first outlines some relevant assumptions that standard PV software relies on to simplify the energy yield simulation, and pinpoints the horizontal constraint, which does not necessarily require the ground to be horizontal, only that its cross-axis slope angle be zero. The mathematical basis for modifications to overcome the horizontal constraint while preserving these assumptions is then described. Finally, the sensitivity of the annual energy yield to the slope of the terrain is analysed in the light of simulation exercises performed with SISIFO for commercial PV plants, and a calculation procedure for dealing with complex orography is proposed.

3.2 Tracking software background

The software available today to simulating tracking PV plants is based on two assumptions that greatly simplify the task. On the one hand, it is assumed that the axis length is infinite (in practice much larger than the tracker width) and that the axis height above the ground is constant along its entire length. This leads to relying on 2D modelling, which reduces the description of the geometry to a projection onto a plane normal to the tracker axes, i.e. the cross-axis plane. On the other hand, it is assumed that the number of axes is infinite (practically more than ten) and that the axes are periodically arranged so that they all lie in the same plane, parallel to the ground, and equidistantly spaced. This leads to neglect all edge effects and to restrict the calculations to only one representative tracker row. Note that this is compatible with considering shading: mutual shading between adjacent tracker rows for back-tracking algorithms and ground shading for estimating G_{REAR}. Both conditions together, 2D modelling and restricting the calculations to only one tracker row, allow for a significant reduction of the simulation

burden, both in terms of the amount of input parameters needed to define the PV array configuration and the computing time.

Available PV software is continuously evolving but usually does not disclose the internal details of the model or submit its procedures to peer-reviewed scientific journals. This makes it difficult to know exactly what the state-of-the-art is. However, it appears that such a 2D approach is followed by most of the software currently used by the PV industry to simulate the energy yield of large PV plants. In addition, any software may have additional constraints. As far as we know, at the time of writing (February, 2023), most industry-standard software is limited by the horizontal constraint. PVsyst has announced[5] plans to overcome such constraint based on 3D modelling. DNV's Solar Farmer software claims to be able to simulate complex terrain using 2D and 3D modelling (Leung et al., 2022). We use SISIFO, as mentioned in the previous chapters. For the purposes of this work, it is sufficient to know that, although their details differ, all these software are essentially compatible, so that they lead to similar results by providing the same input data and loss scenario. In any case, the transition from 2D to 3D scenes is likely to involve a significant increase in mathematical complexity and simulation overhead. This motivates extending the capabilities of SISIFO to overcome the horizontal constraint but still relying on 2D modelling and a single tracker representative row. Interestingly, Solar Farmer authors seem to think that this is a convenient approach. Indeed, (Leung et al., 2022) say that "... *we observed that using a simple geometric shading approach for trackers provides sufficient accuracy for tracker shade, while 3D approach can be used for shade obstacle* ..." .

It is worth taking a moment to introduce the relevant reference frames and coordinate systems involved in the calculations of a tracked PV system. Figure 3.1(left) shows the position of both the sun and the tracker in a site reference frame, using a right-handed three-dimensional Cartesian coordinate system with the X-axis pointing West, the Y-axis pointing South and the Z-axis pointing upwards. The tracker axes are shown as dotted and dashed lines. The coincidence with the Y axis, in red, is the representative row for which calculations are made. Figure 3.1(right) shows the projection of both positions onto a cross-axis plane (a tracker reference frame) with a Cartesian coordinate system

[5] https://www.pvsyst.com/help/

where the X axis contains the tracker axis points. Note the latter is a 2D scene. The depicted cases are:

(f) The traditional case of horizontal ground and north-south oriented axes, implemented in all the current PV software that we know of. The position of the sun in the global reference frame, i.e., the solar coordinate vector (x_S, y_S, z_S) is easily derived from the latitude and time. It should be noted that the position of the sun in the 2D scene, i.e. the vector (x_S, z_S) determines both the angle of rotation of the trackers and the shading scene cast on the ground by the tracker rows. These issues are discussed in the next section.

(g) The case of axes with given azimuth, α_A, on flat terrain. The relevant change from the previous case is the position of the sun in the cross-axis plane. The new sun position can be obtained from the former by applying a basic rotation matrix, rotating the sun position vector counter-clockwise by an angle α_A about the Z-axis:

$$\begin{pmatrix} x'_S \\ y'_S \\ z'_S \end{pmatrix} = \begin{pmatrix} cos\,\alpha_A & -sin\,\alpha_A & 0 \\ sin\,\alpha_A & cos\,\alpha_A & 0 \\ 0 & 0 & 1 \end{pmatrix} \begin{pmatrix} x_S \\ y_S \\ z_S \end{pmatrix} \tag{29}$$

(h) The case of both ground and axes with given azimuth and tilt. That is, here $\alpha_A = \alpha_G$ and $\beta_A = \beta_G$, where α and β are azimuth and tilt respectively, and the subscripts 'A' and 'G' denote axis and ground respectively. The new sun position, by rotating the sun position vector counter-clockwise by an angle β_A about the X' axis, is:

$$\begin{pmatrix} x''_S \\ y''_S \\ z''_S \end{pmatrix} = \begin{pmatrix} 1 & 0 & 0 \\ 0 & \cos\beta_A & -\sin\beta_A \\ 0 & \sin\beta_A & \cos\beta_A \end{pmatrix} \begin{pmatrix} x'_S \\ y'_S \\ z'_S \end{pmatrix} \tag{30}$$

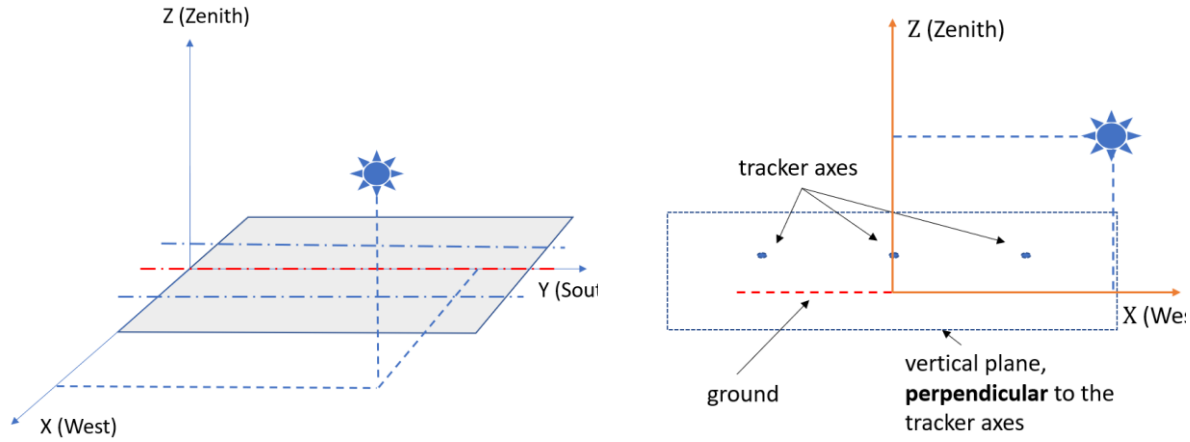
Note that although the ground plane is not horizontal, the intersection of the ground with the cross-axis plane is. Therefore, the axes line, the line that connects the axes crosswise, is also horizontal in the 2D-scene. This is why we say that in this case the horizontal constraint is still respected. SISIFO incorporates this feature from previous versions.

(i) The case where the horizontal and the axes line have, irrespective of α and β, a non-zero cross-axis slope angle, β_{CS}. The axes are not parallel to the steepest line

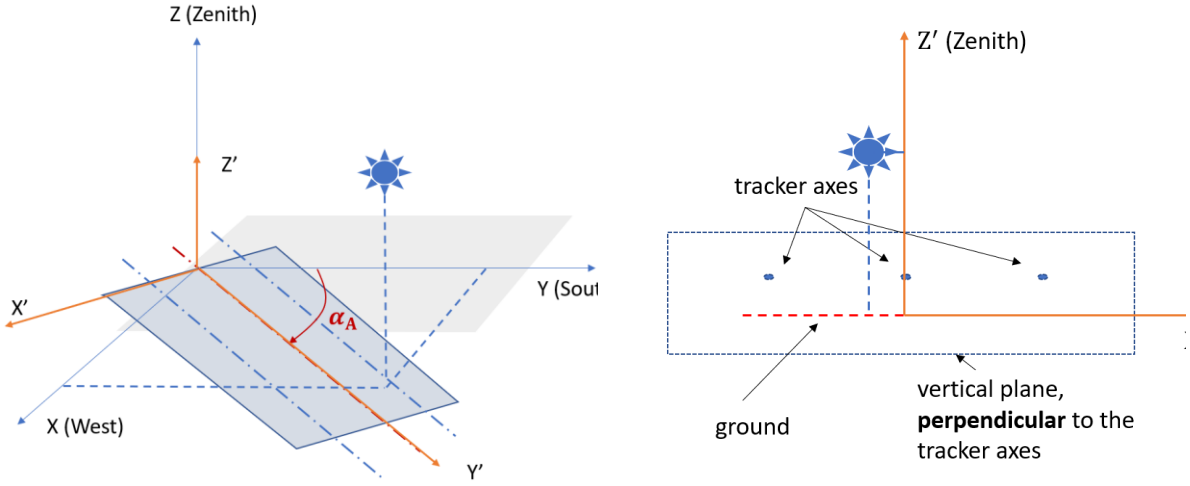
of the terrain and, therefore, $\alpha_A \neq \alpha_G$ and $\beta_A \neq \beta_G$. Again, this implies a change in the position of the sun in the cross-axis plane, and the new position can be obtained by rotating the sun vector counter-clockwise by an angle β_{CS} about the Y'' axis:

$$\begin{pmatrix} x_S''' \\ y_S''' \\ z_S''' \end{pmatrix} = \begin{pmatrix} \cos\beta_{CS} & 0 & \sin\beta_{CS} \\ 0 & 1 & 0 \\ -\sin\beta_{CS} & 0 & \cos\beta_{CS} \end{pmatrix} \begin{pmatrix} x_S'' \\ y_S'' \\ z_S'' \end{pmatrix} \tag{31}$$

SISIFO features this capability from June 2022.



(a)



(b)

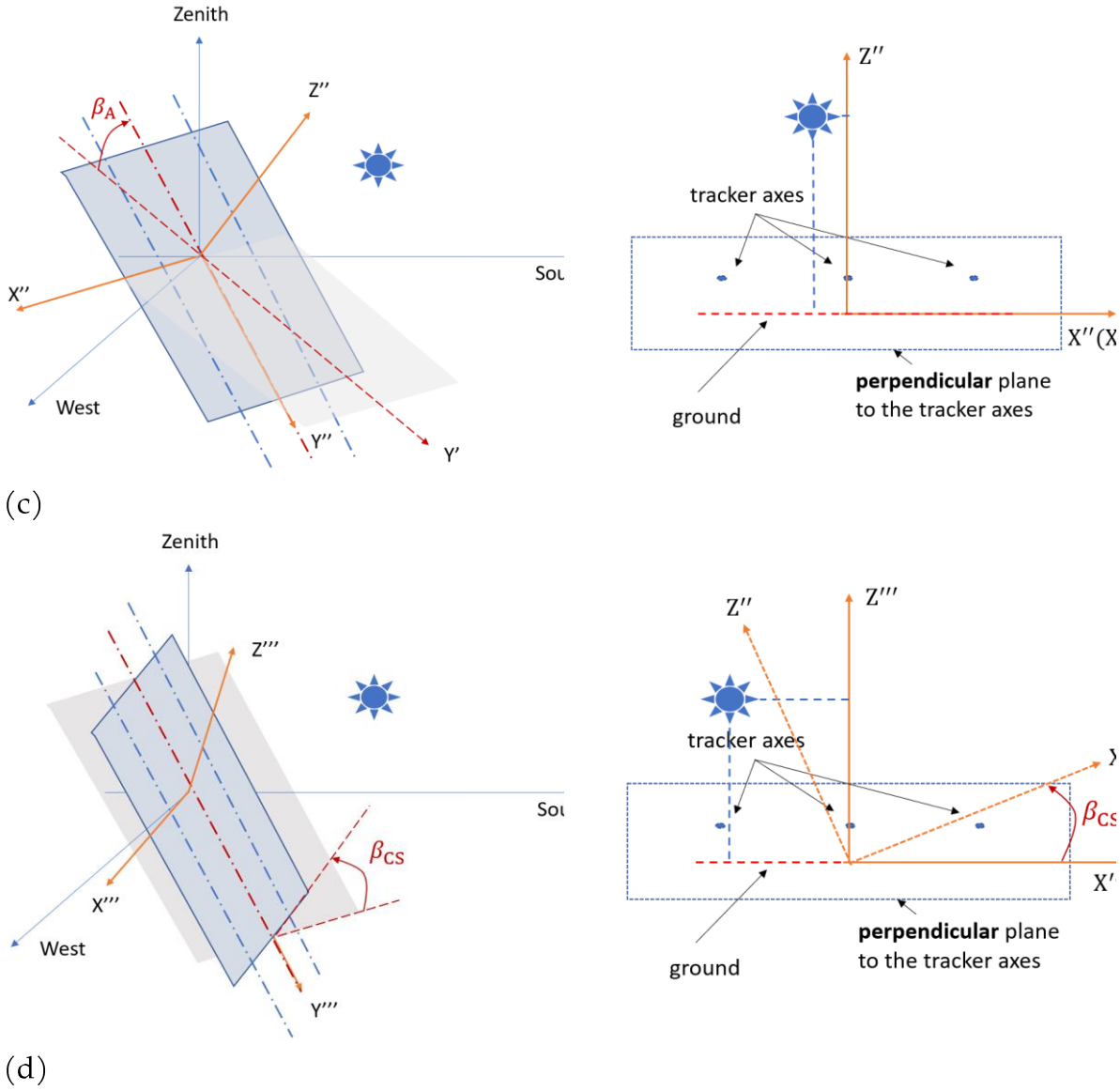


Figure 3.1. Sun and tracker positions in site (left) and tracker (right) reference frames. Depicted cases are: ***(a)*** *Horizontal ground and north-south oriented axes;* ***(b)*** *Axes with given azimuth, α_A, on flat terrain.* ***(c)*** *Ground and axes with given azimuth, $\alpha_A = \alpha_G$, and tilt, $\beta_A = \beta_G$;* ***(d)*** *Ground and axes with different azimuth, $\alpha_A \neq \alpha_G$, and tilt, $\beta_A \neq \beta_G$, leading to a non-zero cross-axis slope angle, β_{CS}, between horizontal and the axes line.*

It should be stressed that the tracker axes must be parallel to the ground in order to preserve the 2D scenes. It is worth noting that this is the current state of the art for industrial single-axis tracker products. Furthermore, equation (31) gives the principle for solving the mathematical problem of cross-axis sloping ground, as it allows the system to be treated as if it were a simple north-south horizontal axis system. However, it is also

interesting to approach the problem in a more intuitive way, as is done in the following two sections.

3.3 The backtracking geometry

Figure 3.2-a shows the principle of the backtracking calculation under horizontal constraint for PV arrays consisting of many relatively long rows of PV trackers equally spaced across the ground plane, i.e. for the case described above (c). The horizontal distance between two adjacent rows and relative to the row width is L_{C0}, where the subscript 'C' means 'crosswise', consistent with the drawing plane being orthogonal to the tracker rows, and the subscript '0' indicates that the distance is considered to be in the horizontal plane. Note that the horizontal constraint means that there is no vertical offset between rows in this plane.

Following the description presented in a previous paper (Lorenzo et al., 2011), the rotation angle of the tracker, ω, is defined as a clockwise angle around the tracker axis, being zero at the horizontal position in the 2-D scene (at noon, in the case of $\alpha = 0$). The "ideal" value, ω_{ID}, which minimizes the angle of incidence of the beam irradiance on the array surface is given by:

$$\tan \omega_{ID} = x''_S / z''_S \tag{32}$$

Other authors refer ω_{ID} as the "true-tracking" angle (Anderson & Mikofski, 2020). The shadow length, s_{ID}, is given by:

$$s_{ID} = \frac{1}{\cos \omega_{ID}} \tag{33}$$

If s_{ID} is larger than L_{C0}, a backtracking correction angle, ω_C, is required to avoid mutual shading. The final resulting rotation angle, ω_{IDC}, is:

$$\omega_{IDC} = \omega_{ID} - \omega_C \tag{34}$$

being

$$\cos(\omega_C) = L_{C0} . \cos \omega_{ID} \tag{35}$$

Figure 3.2-b shows that in the case where the terrain has a cross-axis slope angle, β_{CS}. The point now is to realise that this situation is equivalent to the previous one, that is,

both lead to the same ω_{IDC}, given the horizontal distance between the rows, $L_{\mathrm{C}\beta}$, by adjusting L_{C0} to satisfy the condition:

$$L_{\mathrm{C0}} = L_{\mathrm{C}\beta} + \Delta L_{\mathrm{C}} = L_{\mathrm{C}\beta}(1 + \tan(\omega_{\mathrm{ID}})\tan(\beta_{\mathrm{CS}})) \tag{36}$$

Applying the compound angle cosine identity[6], another way of expressing equation (36) is:

$$\cos(\omega_{\mathrm{C}}) = L_{\mathrm{C}\beta}\left(\frac{\cos(\omega_{\mathrm{ID}} - \beta_{\mathrm{CS}})}{\cos(\beta_{\mathrm{CS}})}\right) \tag{37}$$

(Anderson & Mikofski, 2020) achieves a similar result to that obtained here in a different way.

Note that for horizontal and south-oriented trackers ($\alpha_{\mathrm{A}} = \beta_{\mathrm{A}} = 0$), ground slopes pointing West ($\beta_{\mathrm{CS}} > 0$) result in backtracking starting earlier in the morning and later in the evening than on horizontal ground, for the same ground coverage ratio, *GCR*. Because the distances are normalised to the cross section of the tracker row, the *GCR* is given by:

$$GCR = \frac{1}{L_{\mathrm{C}\beta}} \tag{38}$$

As a representative example, Figure 3.3-left shows the evolution of ω_{ID} and ω_{IDC} for β_{CS}=0° of a tracker with a maximum rotation angle of 55° throughout a June day at a location at 40.38°N latitude. Figure 3.3-right does so for β_{CS}=15° and shows that the correction angle, ω_{IDC}, exceeds 90° after visible sunrise and the backtracking time is shorter in the morning but partly compensated by a longer stay at the limit rotation angle before sunset.

It is worth noting that equation (36) provides a simple way of upgrading tracker controllers *originally* designed for NS-oriented axes and horizontal terrain, in such a way that they can be extended to EW-sloping terrain. A direct way (Lorenzo & Macagnan, 1994) to obtain $\tan\omega_{\mathrm{ID}}$ for equation (36) is:

$$\tan\omega_{\mathrm{ID}} = \frac{\sin\alpha_{\mathrm{S}}}{\tan\gamma_{\mathrm{S}}} \tag{39}$$

[6] Fifth Theorem as chronicled by Copernicus following Ptolemy in Almagest.

where α_S and γ_S are the solar azimuth and solar elevation respectively. Both are easily found in *different* web applications, so the original controller only needs to implement equations (33) to (36). A corresponding closed formulation for the upgrade, using equation (36) for L_{C0}, is:

$$\omega_{IDC} = \omega_{ID} - sign(\omega_{ID} - \beta_{CS}) \cos^{-1}[\min(1, L_{C0}.\cos\omega_{ID})] \quad (40)$$

Note that this does not require the use of matrices or a significant increase in the computing power of the controller. Tracker manufacturers do not usually reveal the internal details of their controllers. However, it is conceivable that this may be the way some tracker manufacturers implement the somewhat bombastically named *"adaptive backtracking 3D"*.

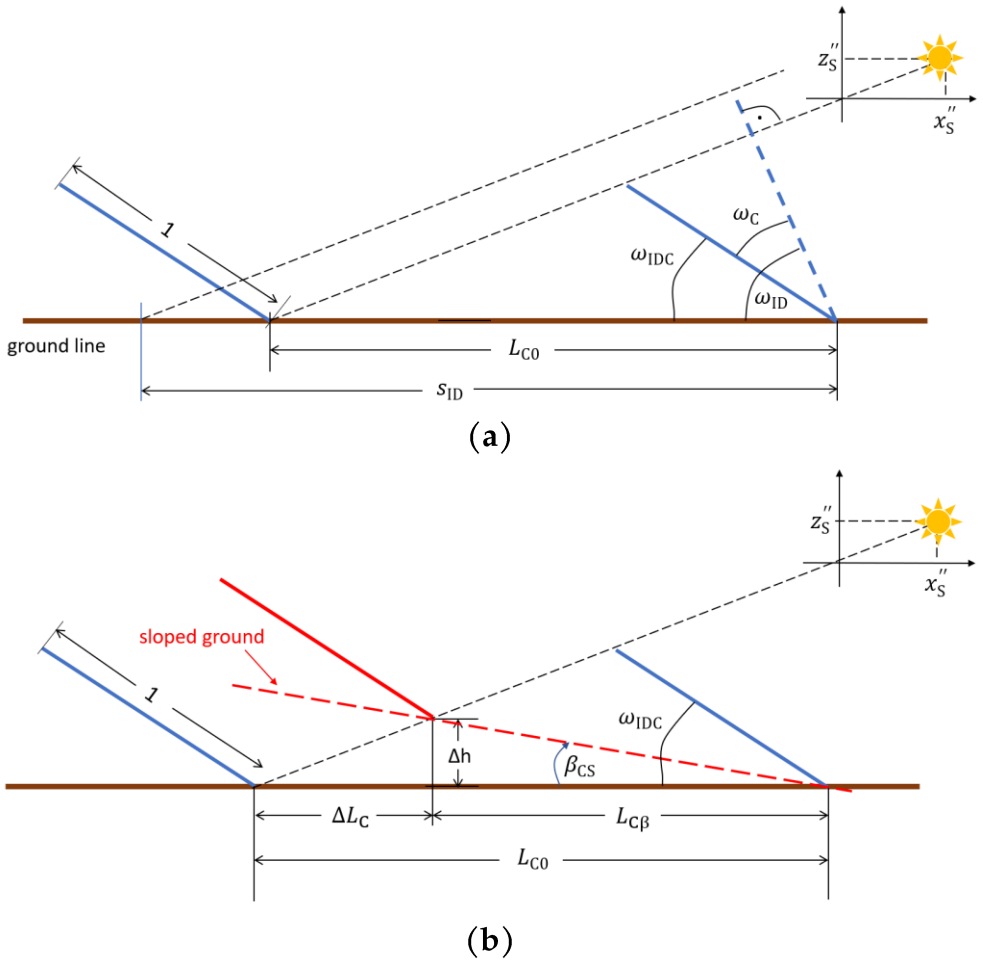


Figure 3.2. Geometry of backtracking for ***(a)*** *horizontal and* ***(b)*** *sloping terrain. Both are equivalent, i.e. lead to the same rotation angle if* $\Delta L_C = L_{C0}\, tan(\omega_{ID})\, tan(\beta_{CS})$.

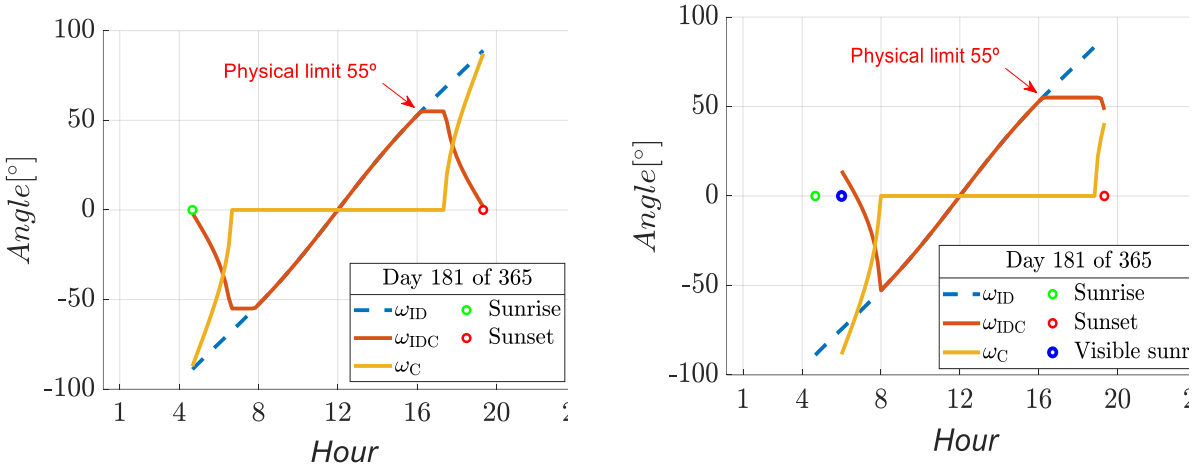


Figure 3.3. Evolution of ω_{ID} and ω_{IDC} for β_{CS}=0° (left) and β_{CS}=15° (right) of a tracker with a limit rotation angle of 55° throughout a June day at a location at 40.38°N latitude.

There are two different approaches to model G_{REAR}: view factors and ray-tracing (Deline et al., 2017). View factors are less computationally demanding and are easier to analyse large and regular arrays typically found in large-scale PV plants. Even more, simplified 2D view factors can effectively model G_{REAR} in these PV arrays (Liang et al., 2019)′(Kopecek & Libal, 2021). This explains why the most widely used PV simulation tools today rely on 2D view factor models. This is the case of PVsyst and SISIFO.

The following explanation is based on the view factor model of SISIFO under horizontal constraint described in a former paper (Ledesma et al., 2020). Figure 3.4-a shows again a projection on the plane orthogonal to the rows. The geometry is defined by ω_{IDC}, L_{C0} and the row centre height, H. The key is to realise that the regular arrangement of the rows translates into a basic pattern consisting of a shaded and an unshaded segment, repeated with a period equal to L_{C0}. Then, assuming that the ground is a Lambertian reflector, the contribution of a ground segment $\overline{L_1L_2}$ to G_{REAR}, is given by:

$$G(\omega_{\mathrm{IDC}})_{\mathrm{REAR}}^{L12} = \frac{\rho\, G_{\mathrm{GROUND}}}{2}[\sin(\phi_2 - \omega_{\mathrm{IDC}}) - \sin(\phi_1 - \omega_{\mathrm{IDC}}) \tag{41}$$

where G_{GROUND} is the incident irradiance in the segment concerned (unshaded and shaded segments can be assumed to be illuminated by the global irradiance and the isotropic component of the diffuse irradiance, respectively), ρ is the albedo of the reflector, $[\sin(\phi_2 - \omega_{\mathrm{ID}}) - \sin(\phi_1 - \omega_{\mathrm{ID}})]$ is the 2D view factor from the reflector segment

to the receiver point, and $\phi_1$and ϕ_2 are the angles between the vertical (in the drawing plane) passing through the receiver point and the lines connecting it to the end of the segment, L_1 an L_2, respectively, as shown in Figure 3.4-b. The total ground reflection component of G_{REAR} is calculated as the sum of the contributions corresponding to all the segments within the rear field of view. Two comments are opportune:

(a) On the one hand, proper estimation of G_{REAR} requires taking in account its non-uniformity over the receiver segment. This can be done in two different ways. One is the surface-to-point approach which consists of first calculating for different receiver points and then averaging the corresponding results. This is the approach used in SISIFO. It brings the advantage of preserving the information about non-uniformity, which is important for further testing purposes, and the inconvenience of having to repeat the G_{REAR} calculations as many times as the number of points considered. For the sake of clarity, all the drawings of this chapter refer only to the centre point of the receiver. The other way is the surface-to-surface approach which consists of integrating directly along the receiver surface. The so-called crossed string method helps. We presume that this is the approach used by PVsyst. Advantages and disadvantages are exchanged. Whatever the approach, the core of the view factor calculation is the determination of the extremes of shaded and unshaded segments. The periodicity of the shaded patterns helps. Figure 3.5-a shows how β_{CS} affects such calculations for a generic L_{i}. The law of sines applied to the triangle $0\widehat{L_{\iota o}L_{\iota\beta}}$ leads to

$$\frac{L_{i\beta}}{\sin\gamma_{\mathrm{S}}''} = \frac{L_{i0}}{\sin\left(\pi - \gamma_{\mathrm{S}}'' - \beta_{\mathrm{CS}}\right)} \tag{42}$$

and

$$\tan\phi_{i\beta} = \frac{L_{i\beta}\ \cos\beta_{\mathrm{CS}}}{\mathrm{h} - L_{i\beta}\ \sin\beta_{\mathrm{CS}}} \tag{43}$$

The purpose of bringing equations (42) and (43) here is no more than to show how the view factors are affected by the slope of the terrain. It should be remembered that these equations are not needed for PV simulation software, provided that the rotation matrices defined in equations (30) and (31) are implemented.

b) The use of the view factors method is extended to the calculation of the reflected component of G_{FRONT}. Figure 3.5-b shows that equations (42) and (43) are again applicable.

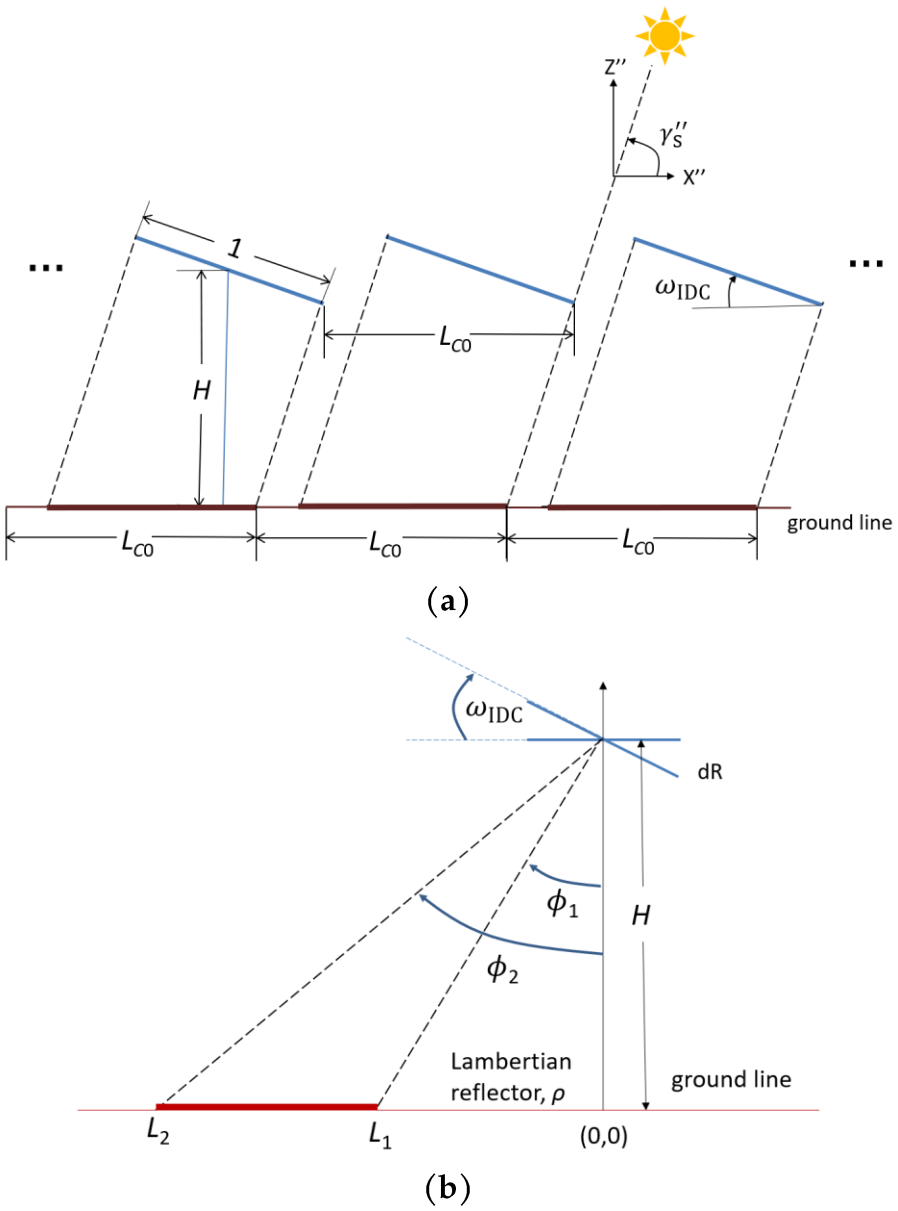


Figure 3.4. Two-dimensional geometry of the ***(a)*** *a bifacial PV array formed by equally spaced rows of and* ***(b)*** *the view factor from the segment* $\overline{L_1L_2}$ *to the receiver surface element.*

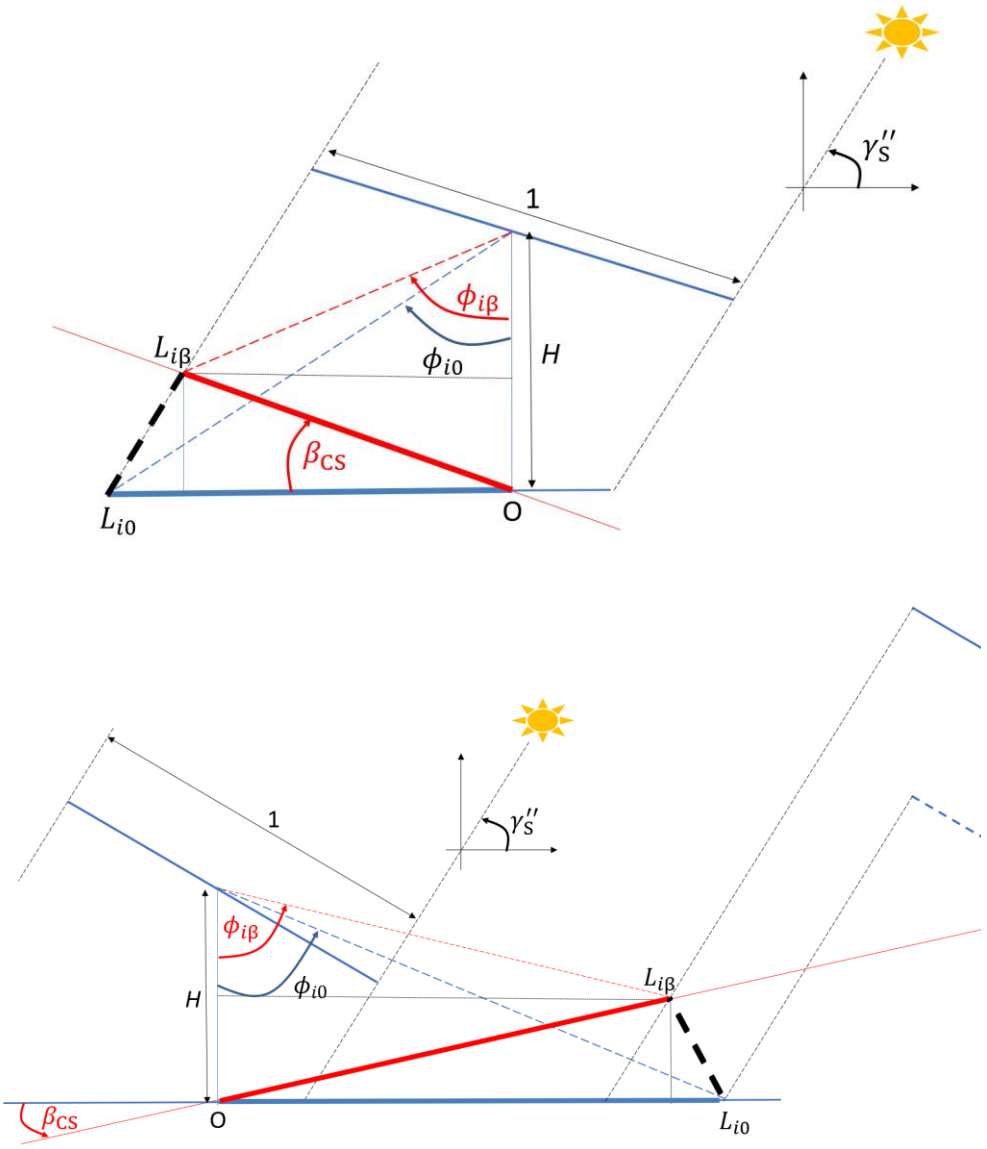


*Figure 3.5. β_{CS} affectation on a generic view factor edge for **(a)** G_{REAR} and **(b)** G_{FRONT}.*

3.4 Implementation in SISIFO

SISIFO is a PV simulation software (freely available at https://sisifo.info) developed by IES-UPM under the umbrella of the European projects PVCROPS (European Commission, 2015), MASLOWATEN (European Commission, 2018) and SOLAQUA(European Commission,2021). Bifacial capabilities for static structures and horizontal single-axis trackers have been available since February 2019, and modelling of

sloped terrain overcoming the horizontal constraint has been available since June 2022. For the latter, the internal modelling had to be modified to incorporate the new rotation matrix defined by equation (2). To introduce the use of this software it is useful to comment on the input data defining the position of the ground surface and of the tracker axes, as well as the irradiance components.

1.1 Input data for the ground surface and the direction of the tracker axis

It is worth remembering that in order to keep on 2D shading scenes, the axes plane must be parallel to the ground plane which in turn implies that for a given ground plane there is only one degree of freedom for fixing the direction of the axes. The image of the axes plane rotating around the normal to the ground plane, introduced in section 2, can help to understand the nature of this degree of freedom. In practice, in order to adapt to the availability of geographical data, SISIFO defines the position of the ground surface in terms of the slope of the ground in the east-west direction, β_{EW}, and in the north-south direction, β_{NS}, and the position of the tracker axes in terms of their azimuth, α_{A}.

Therefore, to use equations (30) and (31), β_{A} and β_{CS} must first be calculated. This is done by first determining the Cartesian coordinates of the unit normal vector to the ground plane in the global reference frame:

$$\begin{pmatrix} x_{\mathrm{G}} \\ y_{\mathrm{G}} \\ z_{\mathrm{G}} \end{pmatrix} = \begin{pmatrix} \cos\beta_{\mathrm{EW}} \\ 0 \\ -\sin\beta_{\mathrm{EW}} \end{pmatrix} \times \begin{pmatrix} 0 \\ \cos\beta_{\mathrm{NS}} \\ -\sin\beta_{\mathrm{NS}} \end{pmatrix} = \begin{pmatrix} \sin\beta_{\mathrm{EW}}\cos\beta_{\mathrm{NS}} \\ \cos\beta_{\mathrm{EW}}\sin\beta_{\mathrm{NS}} \\ \cos\beta_{\mathrm{EW}}\cos\beta_{\mathrm{NS}} \end{pmatrix} \tag{44}$$

then, a rotation about the Z axis by α_{A} results in:

$$\begin{pmatrix} x'_{\mathrm{G}} \\ y'_{\mathrm{G}} \\ z'_{\mathrm{G}} \end{pmatrix} = \begin{pmatrix} x_{\mathrm{G}}\cos\alpha_{\mathrm{A}} - y_{\mathrm{G}}\sin\alpha_{\mathrm{A}} \\ x_{\mathrm{G}}\sin\alpha_{\mathrm{A}} + y_{\mathrm{G}}\cos\alpha_{\mathrm{A}} \\ z_{\mathrm{G}} \end{pmatrix} \tag{45}$$

and β_{A} is given by:

$$\beta_{\mathrm{A}} = \frac{\pi}{2} - \cos^{-1} y'_{\mathrm{G}} \tag{46}$$

A further rotation, this time around the X′ axis by β_{A}, leads to:

$$\begin{pmatrix} x''_{\mathrm{G}} \\ y''_{\mathrm{G}} \\ z''_{\mathrm{G}} \end{pmatrix} = \begin{pmatrix} x'_{\mathrm{G}} \\ y'_{\mathrm{G}}\cos\beta_{\mathrm{A}} - z'_{\mathrm{G}}\sin\beta_{\mathrm{A}} \\ y'_{\mathrm{G}}\sin\beta_{\mathrm{A}} + z'_{\mathrm{G}}\cos\beta_{\mathrm{A}} \end{pmatrix} \tag{47}$$

and β_{CS} is given by:

$$\beta_{CS} = \tan^{-1}(x''_G / z''_G) \tag{48}$$

It is worth to mention that sometimes the position of the ground surface is given using spherical coordinates, in terms of the azimuth, α_G, and tilt, β_G, of its maximum inclination path. Then, β_{EW} and β_{NS} can be obtained by:

$$\begin{aligned} \beta_{EW} &= \tan^{-1}(\sin\alpha_G \tan\beta_G) \\ \beta_{NS} &= \tan^{-1}(\cos\alpha_G \tan\beta_G) \end{aligned} \tag{49}$$

3.4.1 Irradiance components

Typically, software authors tend to model as many details as possible, regardless of their weight in the results. We are no exception. SISIFO takes into account the seven irradiance components listed in Table 3.1, despite four of them: G^{RG}_{FRONT}, G^{B}_{REAR}, G^{DS}_{REAR} and G^{RG}_{REAR} are almost irrelevant to the annual radiation in most practical cases. The table includes comments on how β_{CS} affects each component.

G_{FRONT}	G_{REAR}
Beam, G^{B}_{FRONT} β_{CS} affects the skyline.	**Beam, G^{B}_{REAR}** This component is zero for trackers.
Diffuse from the sky, G^{DS}_{FRONT} β_{CS} entails a vertical offset between the rows. This in turn affects the amount of sky covered by the adjacent frontal row.	**Diffuse from the sky, G^{DS}_{REAR}** β_{CS} entails a vertical offset between the rows. This in turns affects the amount of sky covered by the adjacent rear row.
	Reflected by the rear row, G^{RR}_{REAR} β_{CS} entails a vertical offset between rows. This in turn affects the view factor from the adjacent rear row.
Reflected by the ground, G^{RG}_{FRONT} β_{CS} affects the view factor from the shaded and unshaded areas of the ground.	**Reflected by the ground, G^{RG}_{REAR}** β_{CS} affects the view factor from the shaded and unshaded areas of the ground.

Table 3.1. Influence of β_{CS} on the different irradiance components.

3.5 A representative example

We have proceeded with SISIFO to analyse a single-axis tracking bifacial PV plant over a ground that slopes only in the EW direction. Each particular case is defined by the ground inclinations and the axis azimuth, $(\beta_{\mathrm{NS}}, \beta_{\mathrm{EW}}, \alpha_{\mathrm{A}})$. First, we have simulated the reference PV plant, understood as the horizontal terrain and NS oriented axis (0,0,0). Then, we have dealt with a different ground slope but keeping the NS orientation of the axes $(0, \beta_{\mathrm{EW}} \neq 0, 0)$ and finally we have also varied this orientation $(0, \beta_{\mathrm{EW}} \neq 0, \alpha_{\mathrm{A}} \neq 0)$. Note that this reference PV plant has the same STC power and *GCR* as all other cases considered. The baseline site and constructive details are given in Table 3.2. It is worth noting that for the irradiances observed at the site, the inverter and transformer load ratio ensures continuous operation of the PV array at the maximum power point.

It should be pointed out that the current SISIFO free version only considers G_{REAR} at the centre of the row, whereas the full-version averages the G_{REAR} calculated at several points of the row, chosen according to the physical and electrical layout of the PV array. The case simulated here is a 2P (portrait) layout where there is no separation between the two halves and all PV modules in the same string belong to the same tracker half. We have used four points along the row cross as shown in Figure 3.6. Note that in order to show that the selected points coincide with the top and bottom edges of the solar cells, this figure is unfolded along the tracker axis to show the two PV modules that define the 2P layout. However, it is important to remember that in the simulated 2D scene, the relevant parameter is only the distance from the axis to the points. In our case $\pm$0.03 and $\pm$0.47. The final $G_{\mathrm{REAR}}$for power calculation is the average of the values corresponding to these four points. Bifacial illumination is characterised by the "irradiance bifacial ratio", *GBR*, and by the "equivalent bifacial irradiance", G_{B}, defined respectively as:

$$GBR = \frac{G_{\mathrm{REAR}}}{G_{\mathrm{FRONT}}} \tag{50}$$

and

$$G_{\mathrm{B}} = \mathrm{G}_{\mathrm{FRONT}}(1 + \varphi_{\mathrm{P}}\, GBR) \tag{51}$$

where φ_{P} is the so-called "power bifacial coefficient", i.e. the ratio between the STC powers of the rear and front side of the PV modules (the superscript '*' denotes STC conditions).

$$\varphi_{\mathrm{P}} = \frac{P^*_{\mathrm{REAR}}}{P^*_{\mathrm{FRONT}}} \tag{52}$$

Final energy yield, $Y_{\mathrm{F,y}}$, and the radiation components are given in annual terms, symbolised by the subscript 'y'. Table 3.3 shows the results for the reference PV plant. For the other cases, differences to the reference are indicated by prefixing the corresponding variable with 'Δ'. For example:

$$\Delta Y_{\mathrm{F,y}} = \frac{Y_{\mathrm{F,y}}(\beta_{\mathrm{NS}}, \beta_{\mathrm{EW}}, \alpha_{\mathrm{A}}) - Y_{\mathrm{F,y}}(0,0,0)}{Y_{\mathrm{F,y}}(0,0,0)} \tag{53}$$

Table 3.2. Characteristics of the baseline simulated case.

Site	
Latitude and Longitude	39.9273º and -2.4374 º
Solar radiation, ambient temperature and wind data - Global horizontal radiation - Diffuse/global radiation ratio - Mean daytime ambient temperature, wind speed	10-year TMY from PVGIS (2021/10/27) 1798 kWh/m^2 0.294 16.6 °C, 2.9 m/s
Albedo, ρ	0.2
Terrain:	
Slope in the north-south direction, β_{NS}	0
Slope in the north-south direction, β_{EW}	Variable ($\beta_{\mathrm{EW}} = \beta_{\mathrm{CS}}$)
PV system baseline	
Modules:	
Temperature power coefficient	-0.34%/°C
Bifacial coefficient of power	0.7
ar coefficient	0.075

Transparency factor	0
Trackers:	
Layout	2 Portrait
Axis orientation, α_A	0°
Axis height normalized to cross row section, H	0.552
Ground Coverage Ratio, *GCR*	0.38
Max. rotation angle	±55º
Rest of the system:	
Inverter Load Ratio	1
Transformers Load Ratio	1
Losses scenario:	
STC power losses at the inverter input (LID, PID, front mismatching, DC ohmic losses)	4.0%
Soiling (front side, with normal incidence)	2%
Soiling (rear side, with normal incidence)	0.5%
Structure shading factor	6.4%
Rear mismatching	4.5%

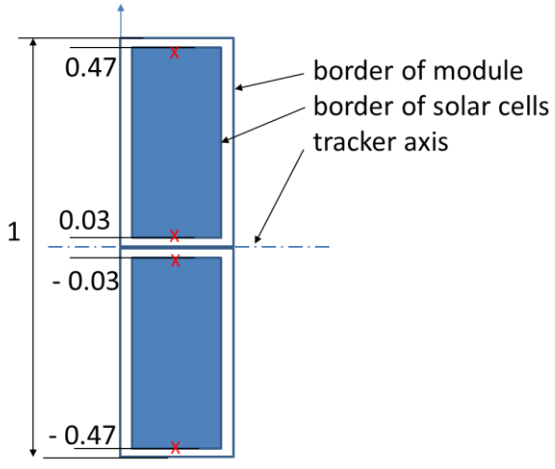


Figure 3.6 Points selected for G_{REAR} calculation. The average of the irradiance calculated for these four points is then used as an input for the power calculation

Table 3.3. Simulation results for the reference PV plant.

Final yield, $Y_{F,y}(0,0,0)$ [kWh/kW$_p$]	2,092				
Annual radiations $[kWh/m^2]$					
Frontal	$G^{B}_{FRONT,y}$	$G^{DS}_{FRONT,y}$	$G^{RG}_{FRONT,y}$		$G_{FRONT,y}$
	1,795	590	14		2,399
Rear	$G^{B}_{REAR,y}$	$G^{DS}_{REAR,y}$	$G^{RR}_{REAR,y}$	$G^{RG}_{REAR,y}$	$G_{REAR,y}$
	0	26	<1	153	179
Equivalent Bifacial					$G_{B,y}$
					2,525
Performance Ratio [%]					
Monofacial ($G_{FRONT,y}$ as refer.)	87.2				
Bifacial ($G_{B,y}$ as refer.)	82.8				

3.5.1 Relationship between terrain slope and energy yield for horizontal NS oriented axis trackers.

Figure 3.7-left illustrates the sensitivity of $\Delta Y_{F,y}$, $\Delta G_{FRONT,y}$ $\Delta G_{REAR,y}$ and $\Delta G_{B,y}$ to β_{EW} for the case of horizontal NS-oriented single-axis trackers, and Figure 3.7-right does the same for the significant radiation components: $\Delta G^{B}_{FRONT,y}$; $\Delta G^{DS}_{FRONT,y}$; $\Delta G^{RG}_{FRONT,y}$; $\Delta G^{RG}_{REAR,y}$ and $\Delta G^{DS}_{REAR,y}$. Note that $\beta_{NS} = 0$ and $\alpha_A = 0$ lead to $\beta_A = 0$ and $\beta_{CS} = \beta_{EW}$. The range considered, $\pm 20^o$, covers most practical cases. Related comments are:

(a) $\Delta Y_{F,y}$ is accurately described by a polynomial. SISIFO systematically uses a 15th-order polynomial for better accuracy, but above 4° tilt a quadratic function is accurate enough. For this case, $\Delta Y_{F,y}(5^o) = -0.002$, $\Delta Y_{F,y}(10^o) = -0.017$, and $\Delta Y_{F,y}(15^o) = -0.040$. This means that $\beta_{CS} \neq 0$ always implies losses. Later, we will see that the same is not necessarily true for the cases $\alpha_A \neq 0$.

(b) The difference in the shape of $\Delta Y_{\mathrm{F,y}}$ and $\Delta G_{\mathrm{B,y}}$, due to temperature and load effects on the efficiency of PV modules, inverters, and transformers, is small. In the following, we will stick to yield for the derivation of analytical expressions because they allow to obtain final energy results, which are the ultimate interest of the PV engineer. However, we will present additional drawings for the radiation components, as they better reflect the physical phenomena caused by the slopes.

(c) $\Delta G_{\mathrm{B,y}}$ is dominated by $\Delta G_{\mathrm{FRONT,y}}$ (blue and yellow lines on the left chart practically coincide) which, in turn, is dominated by $G^{\mathrm{B}}_{\mathrm{FRONT,y}}$ (blue lines in both charts are very similar). In other words, the main effect of the sloping terrain is to modify the horizon by hiding part of the sky.

(d) $\Delta G^{\mathrm{RG}}_{\mathrm{REAR,y}}$ is significantly less sensitive than $G^{\mathrm{B}}_{\mathrm{FRONT,y}}$ (green and blue lines at the right). This is probably due to the averaging of shaded and unshaded ground areas within the field of view of the rear side of the PV array. β_{CS} affects the position of each area --as shown by equations (42) and (43), but the resulting average remains relatively constant.

Quantitatively less important but still interesting:

(a) $\Delta G^{\mathrm{DS}}_{\mathrm{REAR,y}}$ is the most sensitive component to β_{CS} (purple blue at the right). $G^{\mathrm{DS}}_{\mathrm{REAR,y}}$ is almost insignificant for $G_{\mathrm{B,y}}$ (26x0.7/2525 ≈ 0.7%) but not for $G_{\mathrm{REAR,y}}$ (26/179 ≈ 15%). This explains why the shape of $\Delta G_{\mathrm{REAR,y}}$ (red line in the left graph) is more acute than the shape of $\Delta G^{\mathrm{RG}}_{\mathrm{REAR,y}}$.

(b) $\Delta G^{\mathrm{DS}}_{\mathrm{FRONT,y}}$ is nearly constant and even shows a slight increase (≈0.5%) for β_{CS} within $\pm 15^{\mathrm{o}}$. This seems to be due to non-linear effects of β_{CS} on the fraction of sky hidden by the adjacent frontal row.

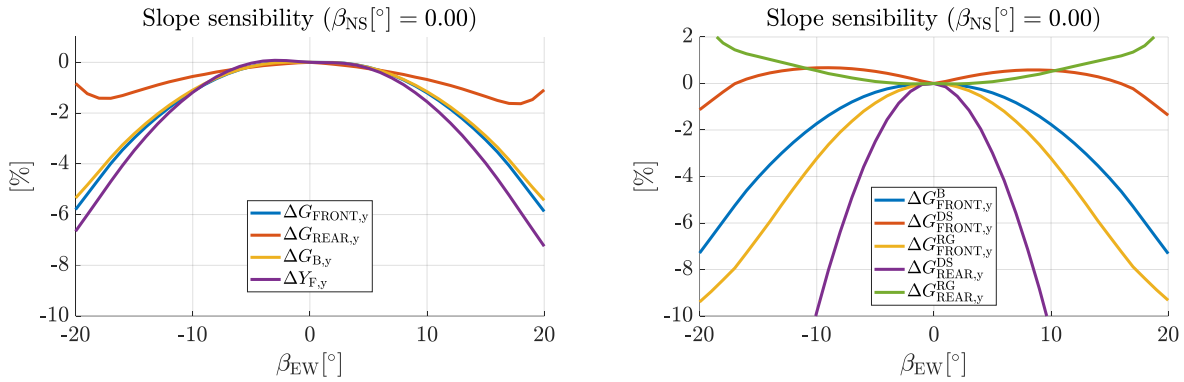


Figure 3.7. (Left) $\Delta Y_{F,y}$, $\Delta G_{FRONT,y}$, $\Delta G_{REAR,y}$ and $\Delta G_{B,y}$ versus β_{EW} for the case of horizontal NS oriented axis. (Right) The same for the significant radiation components: $\Delta G^{B}_{FRONT,y}$; $\Delta G^{DS}_{FRONT,y}$; $\Delta G^{RG}_{FRONT,y}$; $\Delta G^{RG}_{REAR,y}$ and $\Delta G^{DS}_{REAR,y}$.

3.5.2 Influence of other parameters: GCR, ρ and H

Figure 3.8-left, again for the case of NS oriented horizontal single-axis trackers where therefore $\beta_{CS} = \beta_{EW}$, plots $Y_{F,y}$ versus β_{CS} and three other PV system parameters: *GCR*, ρ and *H*. Each of these parameters is varied within a range that covers most practical projects, while the other two are held constant at their baseline values. Figure 3.8-centre shows the bifacial radiation, $G_{B,y}$, versus *GCR*, ρ and *H* for some β_{EW} values and Figure 3.8-right shows the corresponding EW slope sensitivity for the bifacial radiation, $\Delta G_{B,y}(\beta_{CS})$. The relevant observation is that these three parameters affect $Y_{F,y}$ but not $\Delta Y_{F,y}(\beta_{CS})$. Furthermore, Figure 3.8-centre shows that the observed influence is essentially linear with respect to irradiance and therefore with respect to yield. This suggests an analytical expression for $Y_{F,y}$:

$$Y_{F,y}(\beta_{CS}, GCR, \rho, H) = Y_{F0,y}\left[1 + \Delta Y_{F,y}(\beta_{CS})\right][1 + m_{GCR}(GCR - GCR_0)][1 + m_{\rho}(\rho - \rho_0)][1 + m_{H}(H - H_0)] \quad (54)$$

where $Y_{F0,y}$ equals $Y_{F,y}(0,0,0)$ and m_{GCR}, m_{ρ} and m_{H} are the slopes of the relationships between $Y_{F,y}$ and the varying parameters. Note that this equation implicitly assumes independence between those parameters.

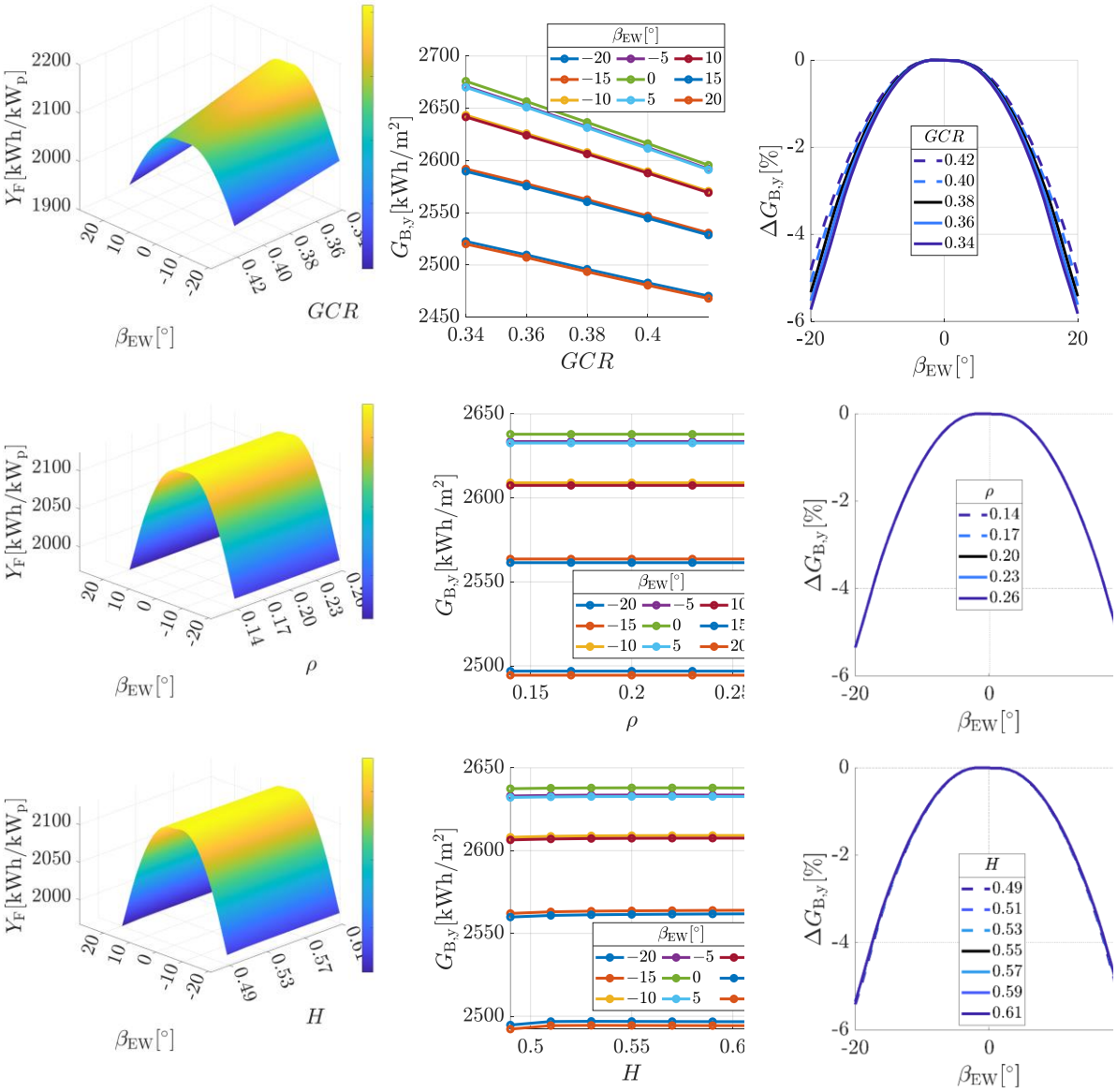


Figure 3.8. (left) Annual final energy yield, (center) annual bifacial radiation and (right) corresponding sensitivity to β_{EW} versus (upper) GCR, *(center)* ρ *and (bottom)* H.

3.5.3 NS oriented non-horizontal axes.

Figure 3.9 presents the same as Figure 3.8, but for the case of NS oriented but not horizontal axes. That is, $\alpha_A = 0 \rightarrow \beta_A = \beta_{NS}$, $\beta_{CS} = \beta_{EW}$. Note that, again, the EW slope implies annual energy losses. But, at the same time, NS slope of the axis entails energy gains, at least for some β_{NS} range narrower than the latitude of the site. Again, β_{NS} affects to $Y_{F,y}$ but essentially not $\Delta Y_{F,y}$, which only depends on β_{EW}.This time, the influence is not

linear but quadratic. Then a new term $[1 + \Delta Y_{F,y}(\beta_{NS})]$ can be added to equation (54)where $\Delta Y_{F,y}(\beta_{NS})$ is a fitted polynomial function.

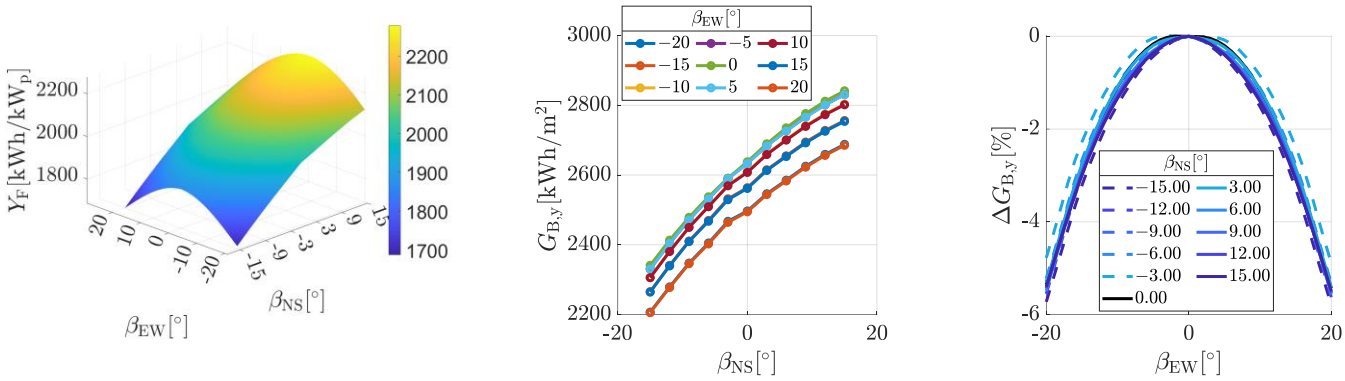


Figure 3.9. (left) Annual final energy yield, (center) annual bifacial radiation and (right) corresponding sensitivity to β_{EW} versus β_{NS}.

3.5.4 Other than NS oriented axes

As an example, Figure 3.10-left shows a terrain with a slope only in the EW direction and a tracker axis with a given azimuth. That is, $\beta_{NS} = 0$; $\beta_{EW} \neq 0$; $\alpha_A \neq 0$. Figure 3.10-right shows the resulting β_A and β_{CS} for $0 \leq \alpha_A \leq \pi/2$. Note that this means varying the axis from the horizontal ($\alpha_A = \beta_{NS} = 0 \rightarrow \beta_A = 0, \beta_{CS} = \beta_{EW}$) to match the maximum terrain slope ($\alpha_A = \pi/2, \ \beta_{NS} = 0 \rightarrow \beta_A = \beta_{EW} = 0$). Intuitively such a variation involves two opposite phenomena in terms of annual radiation gain: $\alpha_A \neq 0$ means losses due to deviation from noon, but the consequent increase in β_A means gains. Interestingly, the combined result is that on this type of terrain aligning the tracker axes in the NS direction is not necessarily the best practical solution. Figure 3.11-a plots $Y_{F,y}$ versus β_{EW} and α_A. The point is that for $\beta_{EW} \neq 0$, the maximum $Y_{F,y}$ appears for $\alpha_A \neq 0$. For example, for $\beta_{EW} = 16^o$ and $\alpha_A = 30°$, the gain is 0.9%. We do not consider the feasibility of mechanical structures to support the stress in the axial direction since $\beta_A > 0$ (about 8° for this example). Figure 3.11-b shows a peculiar shape with peaks and valleys, detailing the front radiation contribution, $G_{FRONT,y}$, and Figure 3.1-c shows the rear radiation $G_{REAR,y}$. They allow to observe that the front radiation behaviour is essentially opposite to the rear one, and therefore in some cases even greater gains could be achieved with monofacial PV plants than with bifacial PV plants.

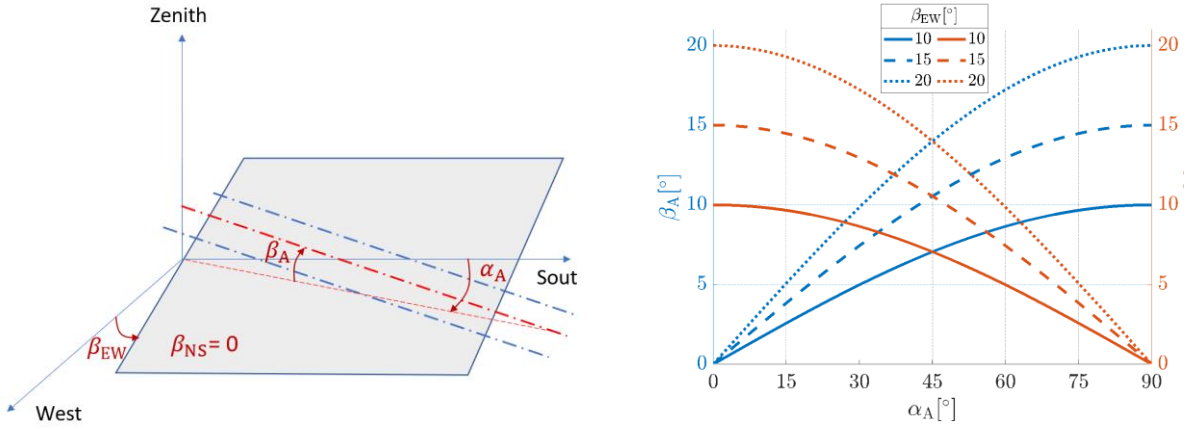
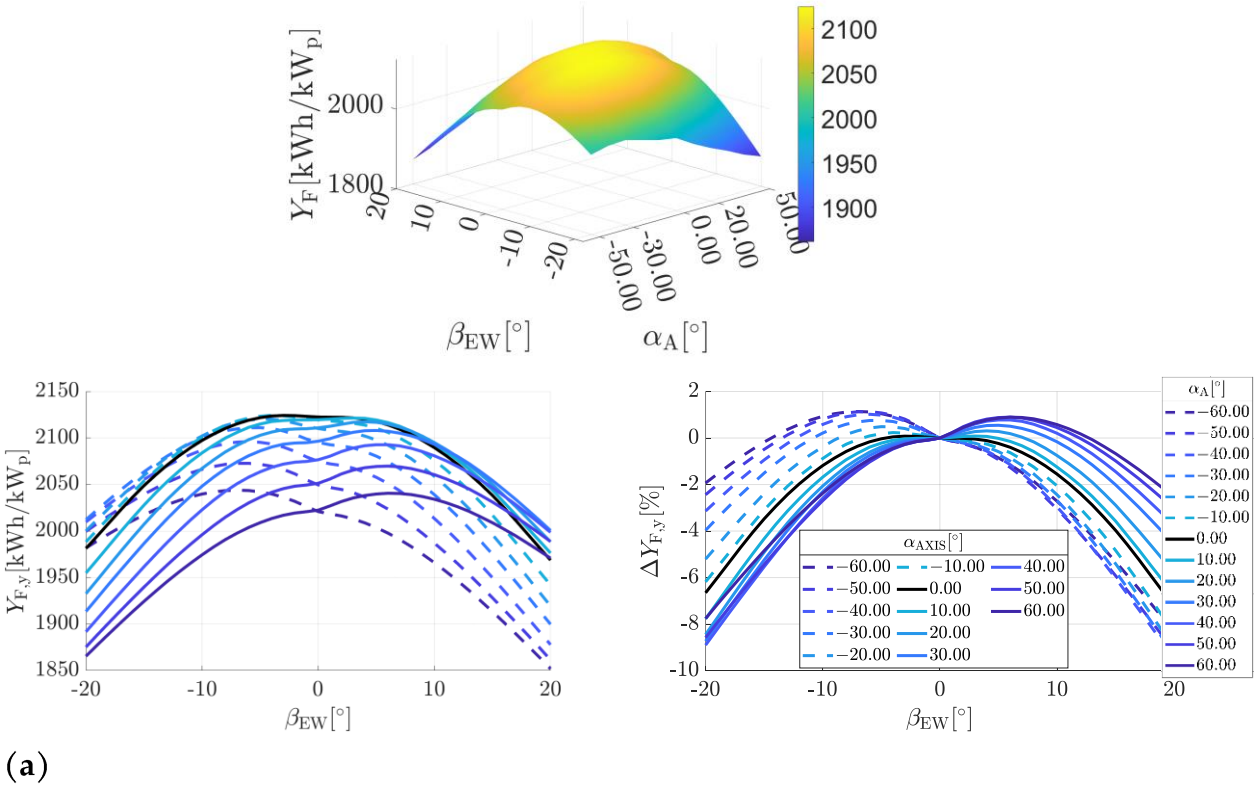


Figure 3.10 (left) A terrain with a slope, β_{EW}, only in the EW direction and a tracker axis with a given azimuth, α_A; (right) the resulting axis slope β_A and cross-axis slope β_{CS} as a function of α_A for three β_{EW} values



(a)

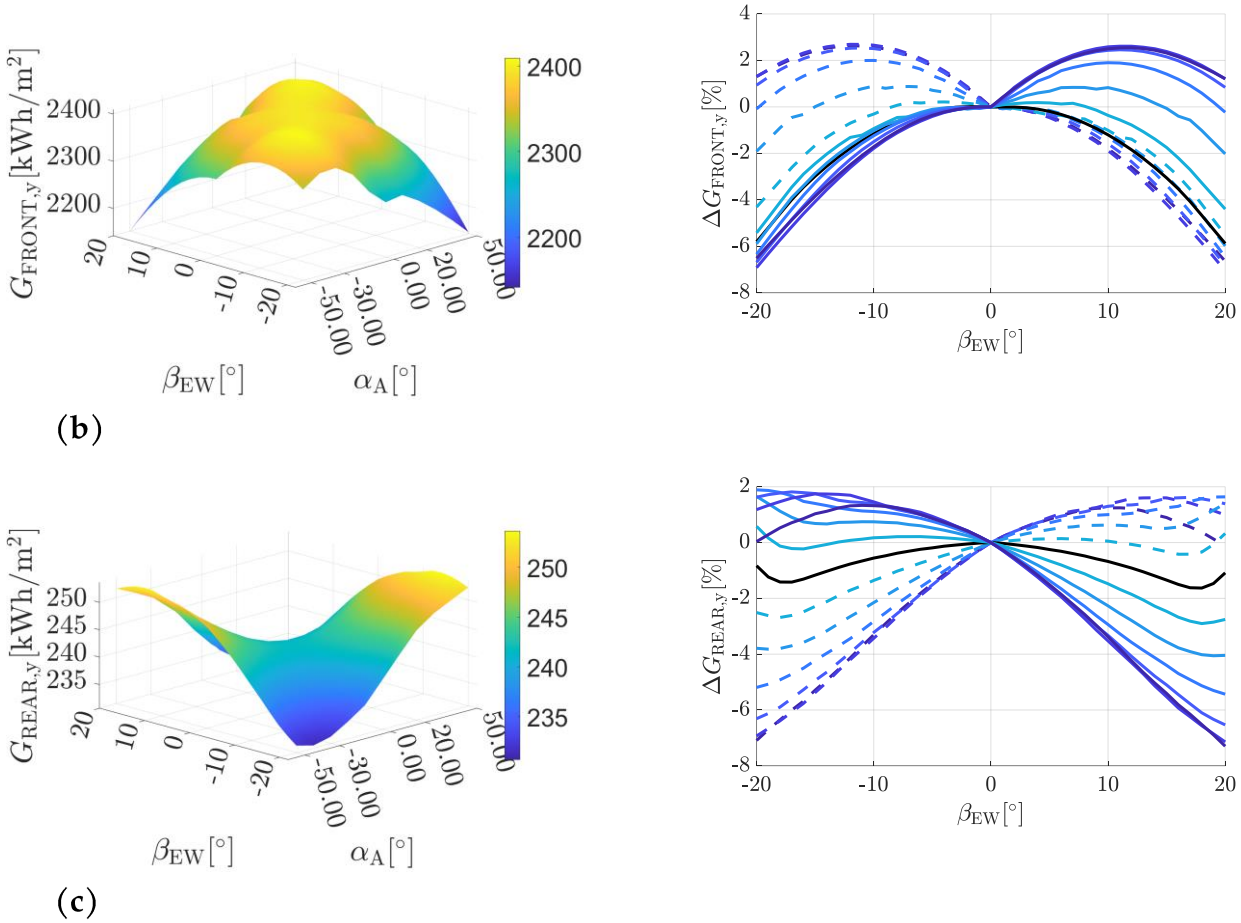


Figure 3.11. ***(a)*** *(top)* $Y_{F,y}$ *versus* β_{EW} *and* α_A*; (left)* $Y_{F,y}$*detail for some* α_A*values; (right) EW slope sensitivity with respect to* $Y_{F,y}(\beta_{NS}=0,\beta_{EW}=0,\alpha_A)$ *for each* α_A*.* ***(b)*** *Front and* ***(c)*** *rear (left) annual radiation versus* β_{EW} *and* α_A*, and (right) EW slope sensitivity with respect to* $(\beta_{NS}=0,\beta_{EW}=0,\alpha_A)$ *radiation for each considered* α_A

3.6 Uneven terrains

For explanation purposes, let us imagine the simple case of a PV plant in an uneven terrain whose East-West topography has translational symmetry in the North-South direction ($\beta_{\mathrm{NS}}=0$). The PV plant is composed of NS oriented horizontal tracker rows ($\alpha_{\mathrm{A}}=0$), equally spaced ($L^i=cte=1/GCR_0$) and equally high above the ground ($H^i=cte=H_0$), as shown in Figure 3.12. Each row "i" is on a point on the ground with slope β_{EW}^i. The range between zero and the maximum observed slope, $\beta_{\mathrm{EW}}^{\max}$, is divided into k

bins of equal size. The ground geometry is defined by the relative frequency of each bin, $n(\beta_{\mathrm{EW}}^{i})$, i.e.

$$1 = \sum_{1}^{k} n(\beta_{\mathrm{EW}}^{i}) \tag{26}$$

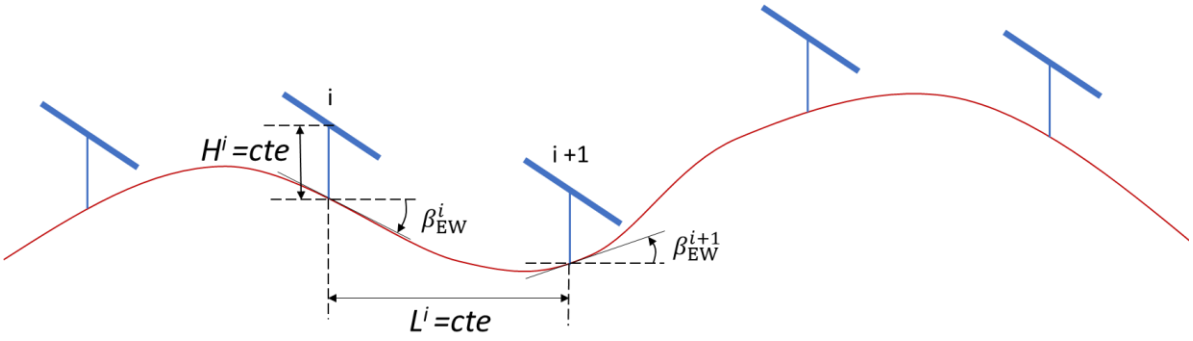


Figure 3.12. EW profile of an uneven terrain with translational symmetry in NS direction.

Assuming that the rotation of each axis is controlled by an adaptive backtracking algorithm, as given by equation (41), a convenient procedure for estimating the energy yield of this plant is:

$$Y_{\mathrm{F,y}} = Y_{\mathrm{F0,y}}[1 - \textstyle\sum_{1}^{k} n(\beta_{\mathrm{EW}}^{i})\Delta Y_{\mathrm{F,y}}(\beta_{\mathrm{EW}}^{i})] \tag{55}$$

where $Y_{\mathrm{F0,y}}$ and $\Delta Y_{\mathrm{F,y}}(\beta_{\mathrm{EW}}^{i})$ are calculated by appropriate simulation exercises. In practice, it may be useful to perform a systematic preliminary simulation campaign leading to the determination of the coefficients of the polynomial $\Delta Y_{\mathrm{F,y}}(\beta_{\mathrm{CS}})$ and then to use equation (25) to determine $\Delta Y_{\mathrm{F,y}}(\beta_{\mathrm{EW}}^{i})$. In any case, this procedure entails the error derived from the implicit assumption that each calculation step of β_{EW}^{i} corresponds to a flat terrain, whereas the real terrain profile is usually a succession of concave and convex zones. Figure 3.13. Real (red) ground profiles, with concave and convex zones, versus implicitly assumed (blue) ones.helps to explain that this procedure tends to overestimate $Y_{\mathrm{F,y}}$ for concave zones (the adjoining tracker rows cast more shadow than in the case of flat terrain) and to underestimate for convex zones. It is to be expected that in most real cases there will be a near balance between concave and convex zones so the resulting global error will be very small.

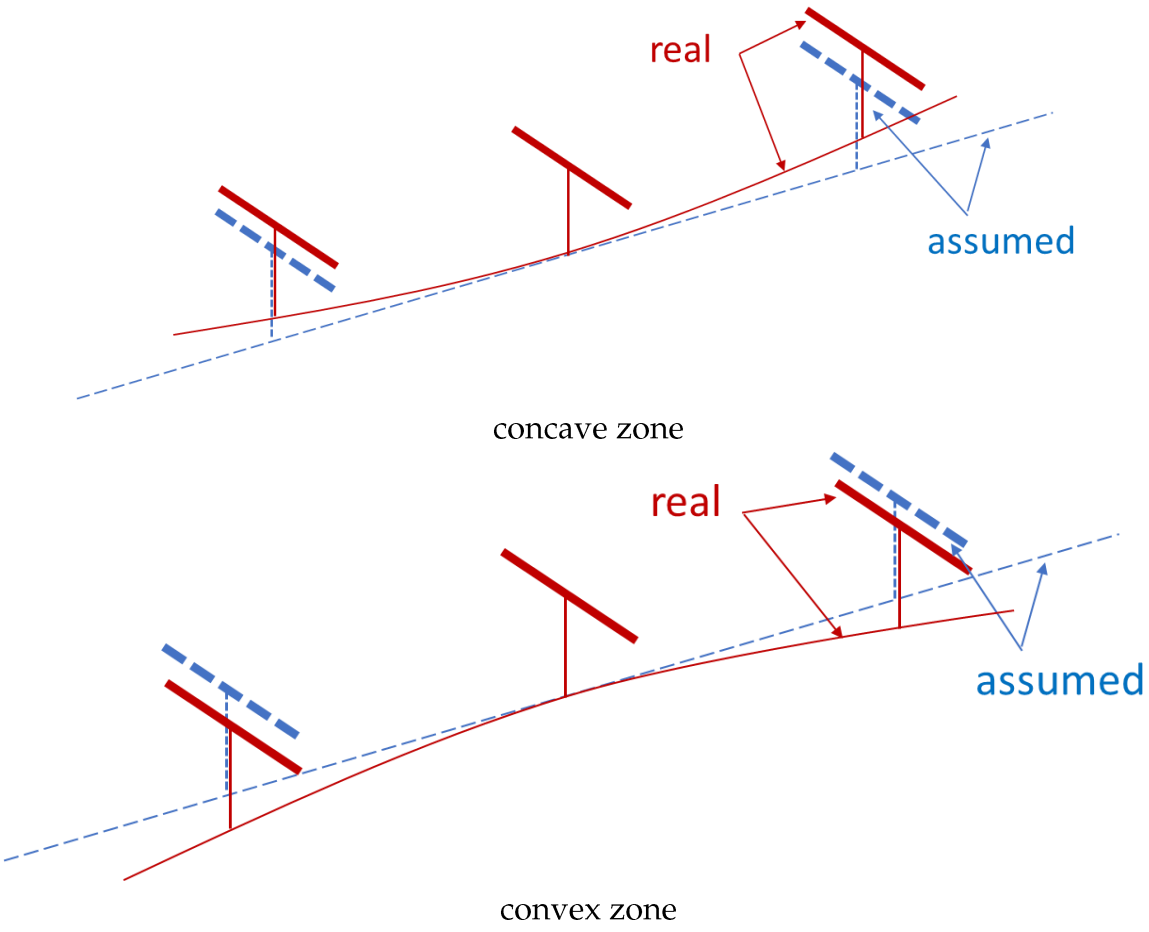


Figure 3.13. Real (red) ground profiles, with concave and convex zones, versus implicitly assumed (blue) ones.

A further step towards real PV plants is to consider unevenly spaced rows, i.e. $L^i \neq cte$. This time the adaptive backtracking algorithm must consider a different distance in the morning and in the afternoon, L^{i-1} and L^i, respectively, and the terrain losses are estimated as:

$$\Delta Y_{\mathrm{F,y}}\left(\beta_{\mathrm{EW}}^{i}\right) = \frac{\Delta Y_{\mathrm{F,y}}\left(\beta_{\mathrm{EW}}^{i}, L^{i-1}\right) + \Delta Y_{\mathrm{F,y}}\left(\beta_{\mathrm{EW}}^{i}, L^{i}\right)}{2} \tag{56}$$

That implicitly assumes that the TMY is symmetric around noon, which is often the case on an annual basis. Again, the preliminary simulation campaign can be extended to determine the coefficient m_{GCR} and then equation (54)can be used for $\Delta Y_{\mathrm{F,y}}\left(\beta_{\mathrm{EW}}^{i}, L^{i-1}\right)$ and $\Delta Y_{\mathrm{F,y}}\left(\beta_{\mathrm{EW}}^{i}, L^{i}\right)$. And similar procedures can be imagined to deal with other real situations, such as tracker rows at different heights ($H^i \neq cte$) and terrains with different relief. To

the best knowledge of the authors, experimental $\Delta Y_{F,y}$ values are not available today, neither in the literature nor by any other means within our reach, so the experimental validation of the procedures proposed here is still not possible. Nevertheless, a hypothetical example is still interesting.

3.6.1 Example

Figure 3.14 shows the orography of a site where a 90 MW NS-oriented single-axis tracker commercial PV plant is currently being installed. The location and other constitutive details are confidential, but not relevant for our present purposes. On the left side of the figure is the original land map. The colour indicates α_G (yellow for $120^o \leq |\alpha_G|$ –north orientation; pink for $60^o \geq |\alpha_G|$—south orientation, blue for west orientation, green for east orientation) and the colour intensity indicates β_G, which is always positive. The right side of this figure shows the final NS oriented axis arrangement after partial earth movement. It can be seen that the PV plant designers have tried to take advantage of the pink areas, as the NS inclination tends to favour the collection of solar radiation, as discussed above (Section 6.3). In addition, the tracker axes are equally spaced (GCR= 0.408). The associated numerical information comes to us in terms of the STC power corresponding to the total number of single-axis trackers located in each (α_G, β_G) bin, as shown in Table 3.4-left, once translated into relative frequency terms. Note that the bin width is 30^o in α_G and 5^o in β_G.

We first calculated the yield of the reference plant, $Y_{F0,y} = 1{,}948.3$ kWh/kW, and the associated differences, $\Delta Y_{F0,y}(\alpha_G, \beta_G)$, for the centre of each bin, to derive the terrain gain/loss map, as shown in Table 3.4-right. The final yield is obtained by combining these two parts of Table 3.4, through an equation formally similar to Eq. (27). The result is an overall increase of 0.16% over $Y_{F0,y}$. This may be surprising, as there is a widespread belief that sloping terrain always means energy losses for large PV plants. However, as this case shows, large terrains usually consist of a combination of areas with a favourable slope and areas with an unfavourable slope. The final PV layout can result in energy gains provided that it is deployed mainly on favourable areas. This comes at the cost of reducing the STC power of the plant that could otherwise be installed on these terrains. Figure 3.14 shows that about 40% of the available land has been discarded in this case.

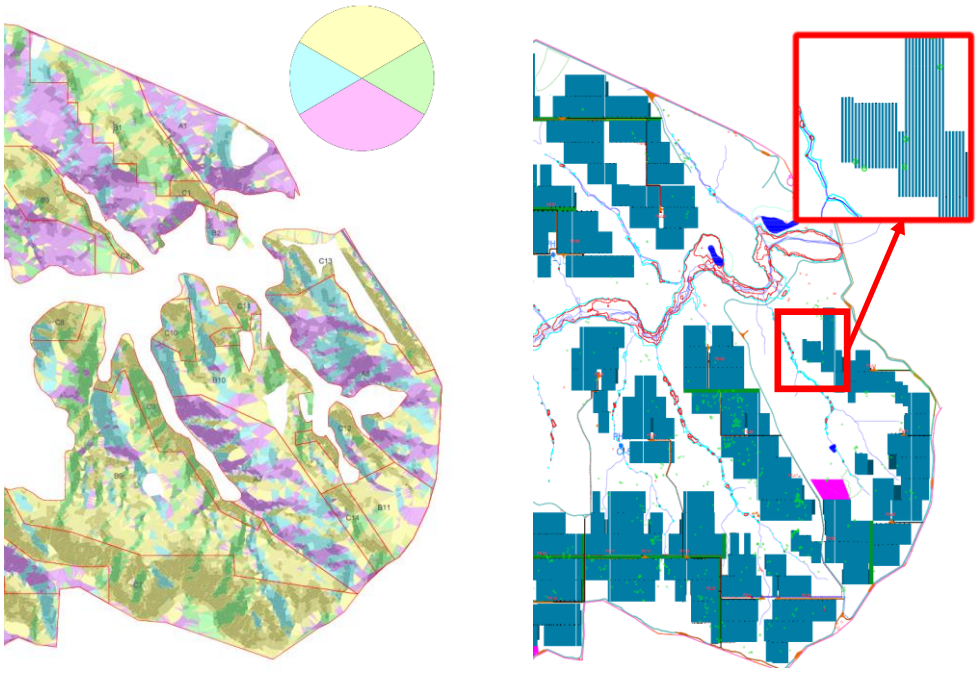


Figure 3.14. Orography of the land on which a commercial PV plant will be built. On the left is the original state of the land (the explanation of the colour code is given in the text), and on the right is the arrangement of the tracker axes after a partial earth movement. It is clear that the PV designer has tried to make the most of the pink areas with favourable slopes.

	Slope				
Azimuth	0	(0,5]	(5,10]	(10,15]	(15
(-165,-195)					
(-135,-165]		1.2%			
(-105,-135]		8.7%	4.7%		
(-75,-105]		7.9%	6.3%	1.6%	
(-45,-75]		2.4%	7.7%		
(-15,-45]		4.9%	3.0%		
(-15,15]	6.3%	3.4%			
(15,45]		6.8%	5.3%	2.7%	
(45,75]		6.2%			
(75,105]		7.1%	4.6%		
(105,135]		4.7%	4.5%		
(135,165]					
(-165,195)					

	Slope				
Azimuth	0	2.5	7.5	12.5	1
-180	0.0%	-1.6%	-5.4%	-9.8%	-15
-150	0.0%	-1.4%	-4.9%	-9.2%	-14
-120	0.0%	-0.9%	-3.4%	-6.9%	-11
-90	0.0%	-0.1%	-1.1%	-3.0%	-5.
-60	0.0%	0.6%	1.2%	0.9%	-0.
-30	0.0%	1.3%	3.2%	4.5%	5.
0	0.0%	1.5%	4.0%	6.0%	7.
30	0.0%	1.3%	3.4%	4.7%	5.
60	0.0%	0.7%	1.5%	1.3%	0.
90	0.0%	0.0%	-0.8%	-2.7%	-5.
120	0.0%	-0.8%	-3.2%	-6.6%	-10
150	0.0%	-1.4%	-4.8%	-9.1%	-14
180	0.0%	-1.6%	-5.4%	-9.8%	-15

Table 3.4 (left) Relative frequency of STC power for each (α_G, β_G) bean. (right) Corresponding gain/loss relative to the reference horizontal case. Azimuth and slope values are in degrees.

3.7 Conclusions

Existing PV simulation tools have built-in single-axis tracking and backtracking functionality, typically assuming that the tracker axes are contained within a horizontal plane. However, real PV plants are often placed on uneven terrain. This chapter describes a mathematical model for dealing with large bifacial one-axis tracking PV plants over terrains of arbitrary orientation and slope. The only constraint is that the ground surface and the plane of the tracker axes must be parallel. This allows the 2D modelling of the ground shading scene required for backtracking geometry and G_{REAR} calculations. The model is based on three rotation matrices that allow the arbitrarily oriented ground-tracking system to be treated as if it was a simple north-south horizontal axis system. We have implemented this model to upgrade SISIFO, an open PV simulation tool developed by IES-UPM, which becomes slope aware in June 2022. In addition, simple equations have been developed that are strictly dedicated to tracking motion control and do not need to consider the bifacial aspects of the PV arrays, but only the relative position (distance and height difference) of the two adjacent trackers of the considered array. These equations provide a simple way to upgrade earlier commercial north-south horizontal axis controllers which are still based on the published two rotation matrices solution (Lorenzo et al., 2011), or no rotation matrices at all, to make them slope aware.

The sensitivity of the energy yield to the ground cross-axis tilt angle, β_{CS}, has been analysed with SISIFO using a representative simulation exercise for a PV plant near Madrid. That leads us to realise that β_{CS} always translates into energy losses, since this angle intrinsically implies a reduction in the field of view of the sky which in turn implies a reduction in frontal radiation. Interestingly, the annual losses with respect to the null slope are well described by a fitted polynomial equation with two coefficients (but the SISIFO tool uses a 15^{th} order polynomial for better accuracy). However, this does not necessarily mean that a PV plant on an uneven surface always lose energy compared to the same plant on a horizontal surface. This is because uneven terrain typically involves β_{CS}, but also tilt-axis angles, β_A, which can favour the collection of solar radiation with respect to the horizontal. Along the same lines, in terrains sloping only in a EW direction ($\beta_{NS} = 0;\ \beta_{EW} \neq 0$), the maximum energy yield corresponds to a tracker axis oriented in

a direction other than NS. The reason for this is that, in order to keep the tracker axes parallel to the ground, the NS axis misalignment with respect to the noon entails $\beta_A > 0$. In this way, the energy losses associated with the axis misalignment are overcome by the corresponding gains associated with the axis tilt.

In practice, when dealing with PV plants in uneven terrain, we understand such terrains as composed of a set of facets, each with a given azimuth, α_G, and slope, β_G. In principle, each facet can host one or more tracker axes with given axis azimuth, α_A. In this way, the PV plant is described by dividing the space (α_G, β_G) into bins of equal size and giving the relative frequency distribution of the STC power over these bins. A dedicated simulation exercise (using as input α_G, β_G and α_A) is then performed for the central position of each bin and the yield of the entire PV plant is calculated as the weighted average of the results, with the relative frequency being the averaging factor. This methodology has been applied to a real 90 MW PV plant with NS-oriented single-axis trackers. This STC power is distributed over 20 (α_G, β_G) bins of size 30º in α_G and 5º in β_G. With respect to the horizontal case, some bins entail energy losses, while other entail energy gains. For example, the bin $(0° \leq \alpha_G \leq 30°, 5° \leq \beta_G \leq 10°)$, simulated with α_G =15°, $\beta_G = 7.5°$ and $\alpha_A = 0°$ as input data leads to a 4.3% increase in yield. However, the bin $(60° \leq \alpha_G \leq 90°, 10° \leq \beta_G \leq 15°)$, simulated with α_G =75°, $\beta_G = 12.5°$ and $\alpha_A = 0°$, leads to a 3.9% decrease in yield. The PV designer can take advantage of placing the plant mainly on favourable facets. This allows a global energy yield similar to, or even slightly higher than, that corresponding to a horizontal terrain, at the cost of reducing the use of available land. In fact, in this case, a global increase of 0.4% has been achieved at the cost of discarding about 40% of the available land.

Chapter 4

MODELLING AND SIMULATION OF MULTIPUMPING PV IRRIGATION SYSTEMS

"It is the obvious which is so difficult to see most of the time." (Isaac Asimov)

4.1 Introduction

PV pumping is a mature technology that has a long history. The first systems date from the 1970s (Palz, 2001), and, since then, it has been widely disseminated in different PV pumping programs. Newkirk, according to (Enochian, 1982), created a bibliography of the published material on PV water pumping systems and found seven publications about systems in the Soviet Union, two in France, one in Germany, and three in the USA. Those outside the USA had peak powers ranging from 300 W_p to 1 kW_p, while for those in the USA, detailed information was only available for a 25 kW_p system. Between 1979 and 1981, the United Nations Development Program, with the support of the World Bank and the Intermediate Technology Development Group, implemented a pilot project to test and evaluate PV pumping systems with powers ranging from 100 to 300 W_p used in small-scale irrigation systems in Mali, Philippines, and Sudan (Halcrow, 1981). Between 1977 and 1990, around 200 systems were installed in Mali, with a total installed power of 220 kW_p (Barlow et al., 1993; Fedrizzi & Sauer, 2002). Following the experience in Mali, the Permanent Interstate Committee for Drought Control in Sahel countries, in cooperation with the European Commission, launched the Solar Regional Program in the

early 1990s (Van Campen et al., 2000), which allowed the installation of 1040 systems, with a total PV power of 1.3 MW_p (Fedrizzi & Sauer, 2002; Van Campen et al., 2000).

These pumping systems have a relatively small power (<40 kW_p), and their technical configuration consists of a PV generator, a frequency converter, and a standard centrifugal pump (Alonso-Abella et al., 2003) (Figure 4.1). Normally there is a water pool where the motor pump raises the water. The motor pump works at a variable frequency that depends on the instantaneous PV power available.

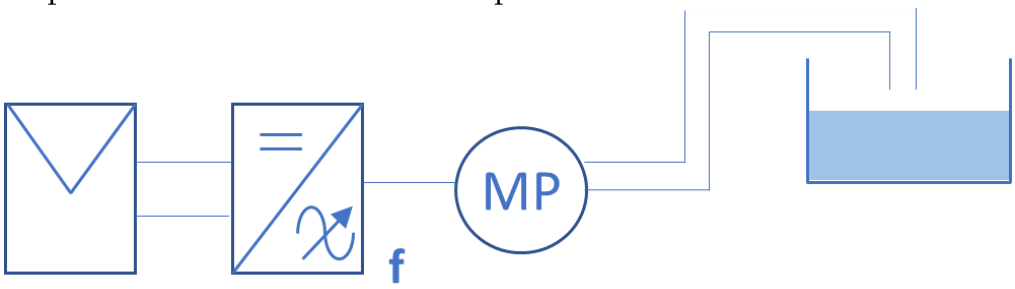


Figure 4.1. Configuration of a PV pumping system: PV generator, frequency converter, centrifugal motor pump, and water pool.

Despite being small systems, much research effort has been devoted to developing sizing methods and optimizing their design. For example, in (Ghoneim, 2006), a simulation program was developed to determine the performance of a direct-coupled PV pumping system while in (Campana et al., 2013), a dynamic modeling tool was used to design a system by combining the models of the water demand, the solar PV power, and the pumping system. In (Renu et al., 2017), a methodology for the performance optimization of solar PV pumps based on the height of the water table and operating point of the pump using the most frequent conditions of a site was proposed. In (Muhsen et al., 2016), a differential evolution-based multiobjective optimization algorithm was proposed to optimally size a PV pumping system considering three weighted individual objectives—loss of load probability, life-cycle cost, and the volume of excess water. Considering some of these objectives, a new method based on the de-termination of loss of power supply probability was used in (Bouzidi, 2013), a sizing model to optimize the sizes of the different components of a system with a water storage tank considering the loss of power supply probability and the life-cycle cost was recommended in (Bakelli et al., 2011), a technique for order performance by similarity to ideal solution method integrated with the analytic hierarchy process method was proposed to optimally size PV

pumping systems based on the loss of load probability, the excess water volume, and the life-cycle cost (Muhsen et al., 2018). Similarly, a techno-economic optimization model was recommended to deter-mine optimally the capacity of the components of a system with a water storage tank (considering the deficiency of power supply probability and life-cycle costs) (Olcan, 2015). In (Yahyaoui et al., 2017), an approach to size the optimal surface of the PV modules, the optimal capacity of the battery bank, and the volume of the water storage tank was proposed. Finally, in (Monís et al., 2020), a heuristic method based on the hybrid approach that uses search space reduction was developed and adapted to the optimal design of small off-grid PV irrigation systems with storage tanks.

On the other hand, as the pumping systems make the motor pumps operate at variable frequency, research work has also been dedicated to their modeling in this working condition: in (Suehrcke et al., 1997), the application of pump similarity laws and the equations to calculate PV yields allowed a relationship between solar radiation and pump flow rate for a given pipeline; in (Hamidat & Benyoucef, 2008), two mathematical models that linked the operating electrical power to the water flow rate of the pump versus total head were proposed; and in (Djoudi Gherbi et al., 2017), two mathematical motor-pump models for PV applications were improved and validated.

There are also numerous simulation tools that make it possible to predict the productivity of PV pumping systems. The most relevant are mentioned here: DASTPVPS is a simulation tool developed by the Universität der Bundeswehr München (Mayer et al., 1995); PVsyst is the simulation tool probably most used in the professional world of photovoltaics (it is integrated with the solar radiation database METEONORM and it also offers the possibility of simulating PV pumping systems (Mermoud & Wittmer, 2017)); WinCAPS is the tool of the main Danish pump manufacturer (Grundfos, n.d.); COMPASS (*COMPASS*, n.d.) is the tool of the main German pump manufacturer, and it is integrated with the solar radiation database provided by NASA; SOLARPAK is the tool of another world leader manufacturer of submersible motors (Franklin Electric, n.d.). All of them are just capable of simulating a single set of PV generator–frequency converter–motor pump, include default settings for inexperienced users, and use simple sizing methods such as the so-called "peak month" method. There are also other tools for the design and sizing of irrigation networks, such as Hydrocalc (Netafim, n.d.) or GESTAR

(Estrada et al., 2009; *GESTAR*, n.d.), and tools for irrigation requirements depending on the crop needs, such as CROPWAT (FAO, n.d.).

These relatively small-power pumping systems with a single motor pump served mainly to supply drinking water to populations in developing countries where the conventional electrical networks necessary to raise water from the ground did not exist. However, the significant growth in electricity prices (Langarita et al., 2017) has made electricity-intensive applications look for cheaper alternatives. This is the case of modernized irrigation in professional agriculture in first-world countries that has pumping stations fed by much larger powers (>1 MW) and with much more complex configurations, with several groups of motor pumps of different models and of different powers and connected to the conventional electricity grid.

In this context, large-power PV irrigation systems (PVISs) have been proposed and introduced to the market and are growing significantly. For example, Knech et al. wrote about a possible PV plant of 1800 kW_p for a 12,000 ha farm in Patagonia (Knecht & Baumgartner, 2017). Carrêlo et al. presented a comparative economic feasibility analysis of five large-power PVISs in the range from 40 to 360 kW_p in the Mediterranean region (Carrêlo et al., 2020). Herraiz et al. technically studied the biggest one of the previous systems and a new one of 213 kW_p in Spain (Herraiz et al., 2022). Almeida et al. also technically studied one of the previous systems—a 140 kW_p system in Portugal (Almeida, Carrêlo, et al., 2018). In addition, some other systems can also be found in Spanish news—a 121 kW_p in Valladolid (Innovagri, 2016) or a 190.8 kW_p in Albacete (Viaintermedia.com, 2017). All these systems exceed the previous limit of 40 kW and reach the range of megawatts required by professional irrigators thanks to the fact that technical and economic barriers (EIP Water, 2012) have been removed—for example, the intermittent nature of the PV power was solved without the need of batteries, taking advantage of the energy regeneration of the motor pumps (Fernández-Ramos et al., 2018), and cost savings of up to 80% are shown in some real-scale experiences (Carrêlo et al., 2020; Innovagri, 2016).

As traditional pump selection methods were based on maximising the pump efficiency at the duty point at a certain single operating frequency, they were not useful for PVIS operating at variable frequency. As a first result of this thesis, (Almeida, Ledesma, et al., 2018) presents a new pump selection method that firstly considers pumps

with H-Q curves with a high slope and the duty point in the right third of the curve to ensure a wide range of operating frequencies, and secondly evaluates the efficiency over the whole range of frequencies. An example of a performance comparison between the pump selected using the new method and the traditional method is shown by comparing the performance of a PVIS in Madrid with both pumps. The results show that by using the new method, the annual volume of water pumped increases by 21.1% and the pump efficiency increases by 4.3%.

The appearance on the market of large-power PVISs to feed complex pumping stations has made it necessary to develop new simulation tools to simulate their performance. Some contributions to this need can already be found in the literature. It is worth mentioning the work of (Gasque et al., 2020) in which a method for distributing the available PV power between two equal pumps working in parallel was proposed. The authors concluded that the power distribution ratio between the two pumps to maximize the water flow rate is 0% or 50% (i.e., just one operating pump or two with half available PV power each). There are also works that analyzed how to match the operation of the pumps to the demand in systems without limitation in the available energy that could be adapted for large-power PVISs (da Costa Bortoni et al., 2008; Olszewski, 2016).

However, it is not possible to find published works that allow the simulation of PVISs that feed more complex pumping stations such as those implemented in modernized irrigation. The difficulty in simulating the behavior of these systems when they are powered by a single PV generator lies in establishing the number of pumps that should be operating and their working frequency depending on the available PV power at every instant and, at the same time, establishing the hydraulic working point (water flow, Q, and pumping head, H) since the greater the number of pumps, the greater the water flow rate but also the pumping head, since friction losses in the pipeline increase due to the greater water flow. Dynamic input PV power and dynamic hydraulic duty point make it complex to solve the problem of calculating and simulating the maximum water flow rate pumped by the PVIS for a certain available PV power.

Objectives and Organization of this Chapter

The objective of this chapter is to present new models that allow simulating the productivity of complex PVISs, such as those that exist in large-power pumping stations in irrigation communities. The models developed in this chapter seek to maximize the

water flow rate pumped at each moment according to the available PV power in large PVISs that work only with the PV generator (without the support of another power source and without the use of batteries). The models have been developed for pumping stations that raise water to an elevated water pool but are easily transferable to direct pumping to the irrigation network (i.e., systems that work at constant pressure).

The models developed and presented here were implemented in the SISIFO tool in 2021, and were used to analyze a real case study and illustrate the advantages of these models with respect to the current state of the art.

The chapter is structured as follows: after this introduction, which justifies the novelty of this work, Section 4.2 presents the work development methodology, and Section 4.3 presents the new models developed. In Section 4.4, some interesting results are presented and discussed as a result of the application of these models to various configurations of PV irrigation systems and to a real case study. The chapter ends with Section 4.5 presenting the main conclusions.

4.2 Materials and Methods

The methodology consists of two steps: the development of the models of two representative configurations of multipump PV irrigation systems and the application of the models to the simulation of a representative case study.

First, a system is modeled that consists of a group of several equal pumps in parallel that share a single PV generator and a hydraulic system, where at any given time, all or only part of the pumps may be active depending on the available PV power (Figure 4.2). Active pumps are synchronized in frequency, and the frequency value is calculated to maximize the water flow rate pumped. Frequency-synchronized equal pumps allow the modeling of an equivalent pump for each number of active pumps, which simplifies the calculation, as it is presented in Section 4.3.1. Therefore, the aim of this model is to select the combination of active–inactive pumps and working frequency that produces the highest water flow rate based on the available PV power at each moment.

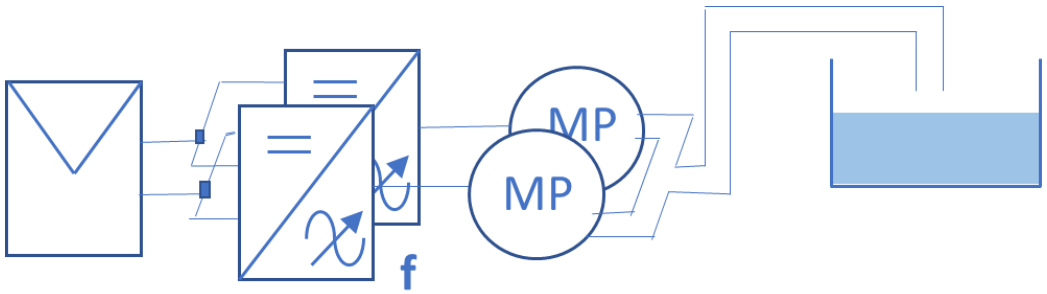


Figure 4.2. Model consisting of a group of several equal pumps in parallel that share a PV generator.

Second, a system consisting of two groups of pumps working in parallel and sharing the same PV generator and hydraulic system is modeled (Figure 4.3). This case allows using different pumps in each group. The model chooses the combination of active–inactive pumps and working frequency in each group that maximizes the total flow rate pumped based on the available PV power. Two variants are modeled:

(a) The active pumps of the first group operate synchronized with each other at a fixed frequency (typically, it corresponds to the nominal frequency or the frequency at which maximum efficiency is achieved), and the active pumps of the second group operate synchronized with each other at a variable frequency;

(b) The pumps in both groups operate at a variable frequency, and this frequency may be different in each group but equal within the same group.

Finally, a case study is simulated to analyze, first, the details of the models and, second, the advantages of multipump models compared to the traditional methodology of simulation of these kinds of systems. The case study is based on a PV irrigation system of 3625 kW_p located in Monegros (Spain) with a pumping station with a first group of five pumps of 500 kW each and a second group of two pumps of 200 kW each. The power rating of each frequency converter equals that of the pump to which it is connected.

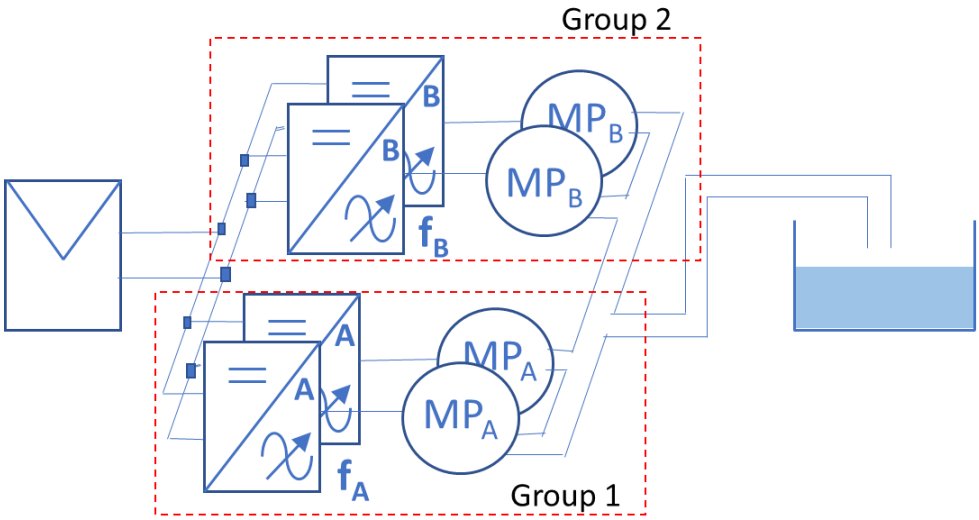


Figure 4.3. Model consisting of two groups of pumps working in parallel and sharing the same PV generator.

4.3 Modelling of the Multipumping PV Irrigation Systems

4.3.1 Configuration 1: Multipump PVIS Made Up of a Group of N Equal Motor Pumps, in Parallel and Synchronized in Frequency

The first step to model this configuration consists of obtaining the characteristic curves of an equivalent pump corresponding to N equal and frequency-synchronized pumps. The starting point is to obtain the characteristic curves of the individual pump at its nominal frequency, from the manufacturer's datasheet (Equations (57) and (58)):

$$H = k_{\mathrm{b0,1}} + k_{\mathrm{b1,1}} Q_1 + k_{\mathrm{b2,1}} Q_1^2 \tag{57}$$

$$P_2 = k_{\mathrm{p0,1}} + k_{\mathrm{p1,1}} Q_1 + k_{\mathrm{p2,1}} Q_1^2 \tag{58}$$

where H is the pumping head, P_2 is the demanded power at the pump input (or motor output), Q_1 is the water flow, and the parameters $k_{\mathrm{b0,1}}$, $k_{\mathrm{b1,1}}$, $k_{\mathrm{b2,1}}$, $k_{\mathrm{p0,1}}$, $k_{\mathrm{p1,1}}$, and $k_{\mathrm{p2,1}}$ are the parameters that fit the curves of the individual pump.

At a certain head H, the pump equivalent to N equal pumps working in parallel will pump a flow Q_N corresponding to the sum of the flow rates Q_1 that each individual pump elevates at the same head; therefore, from Equation (57), it is simple to deduce that:

$$H = k_{b0,N} + k_{b1,N}Q_N + k_{b2,N}Q_N^2 = k_{b0,1} + k_{b1,1}Q_1 + k_{b2,1}{Q_1}^2 \quad (59)$$

where $Q_N = N * Q_1$, $k_{b0,N} = k_{b0,1}$, $k_{b1,N} = \frac{k_{b1,1}}{N}$, and $k_{b2,N} = \frac{k_{b2,1}}{N^2}$.

In the same way, from Equation (58), it follows that the power $P_{2,N}$ necessary for the equivalent pump to pump a flow Q_N corresponds to the sum of the power P_2 of the N individual pumps when they pump a flow Q_1:

$$P_{2,N} = k_{p0,N} + k_{p1,N}Q_N + k_{p2,N}Q_N^2 = N(k_{p0,1} + k_{p1,1}Q_1 + k_{p2,1}Q_1^2) \quad (60)$$

where $k_{p0,N} = N * k_{p0,1}$, $k_{p1,N} = k_{p1,1}$, $k_{p2,N} = \frac{k_{p2,1}}{N}$.

Figure 4.4 shows graphically the characteristic curves of the equivalent pump corresponding to N pumps, where N is in the range $[1, 5]$.

On the other hand, the hydraulic system made up of a set of pipes of a certain diameter and length that connects the pumping station with the water pool imposes a Q-H curve that we call the "system curve" and that has the following expression:

$$H = k_{s0} + k_{s2}Q_1^2 \quad (61)$$

where k_{s0} and k_{s2} are the parameters that fit the system curve.

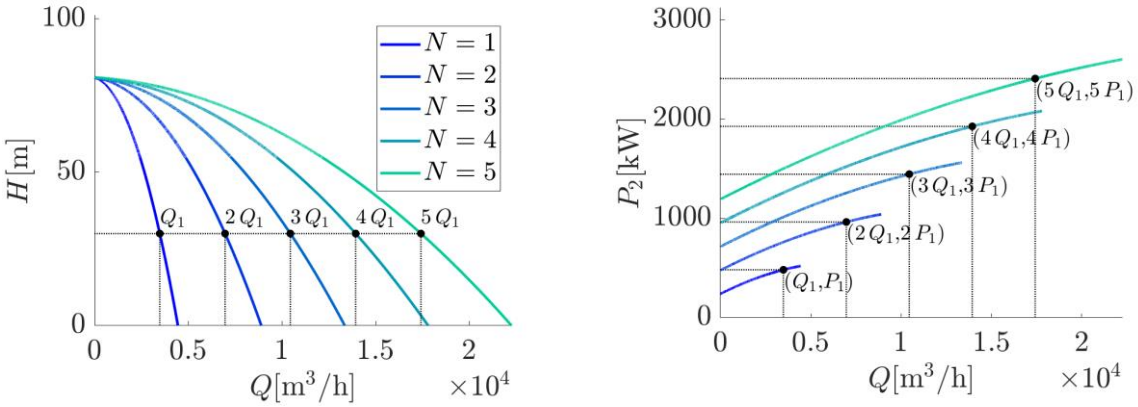


Figure 4.4. Characteristic curves of an equivalent pump corresponding to N equal and frequency-synchronized pumps, where N = 1..5.

As this equivalent pump operates at a variable frequency depending on the available PV power, $P_{DC,mpp}$, it is necessary to deduce the DC power, P_{DC}, needed to satisfy the one demanded by the pump, P_2, at all possible *Q-H* working points within the range of frequencies at which it can operate. This calculation is made from the equivalent pump curves in three consecutive steps:

(a) Determine the power P2 demanded by the equivalent pump at a certain working point Q-H;

(b) Obtain P_{DC} at the input of the frequency converter corresponding to that P_2, assuming that the motors of all pumps are identical;

(c) Select the combination of active pumps that maximizes the flow rate pumped given the available PV power $P_{DC,mpp}$.

4.3.1.1 Calculation of P_2 for Any Q-H Working Point

To calculate the P_2 required by the equivalent pump working at a certain point (Q_B, H_B) not included in the *Q-H* curve at nominal frequency, the affinity laws are used following the procedure described in (Munoz et al., 2015) but varying the head instead of the flow (Figure 4.5). Given a certain H_B:

(a) Calculate the required flow Q_B as the real positive root for Equation (3): $0 = (k_{b0,N} - H_B) + k_{b1,N}Q_B + k_{b2,N}Q_B^2$ obtaining point B (Q_B, H_B) at frequency ω.

(b) Determine the affinity parabola ($H = k_0 + k_2Q^2$) that passes through point B, where $k_0 = 0$, $k_2 = H_B/Q_B^2$. The affinity parabola connects the points of equal efficiency.

(c) Calculate the intersection of the affinity parabola and *Q-H* characteristic curve of the pump at rated frequency, ω_{rated}, to obtain point C (Q_C, H_C).

(d) Determine the hydraulic power at point C, $P_{HC} = \theta \cdot H_C \cdot Q_C$, where θ is a constant value that depends on the water density and gravity.

(e) Determine P_2 at point C, $P_{2C}(Q_C)$ using Equation (4).

(f) Calculate pump efficiency at point C, $\eta_{PC} = P_{HC}/P_2(Q_C)$, which is equal to the efficiency at point B, $\eta_{PB} = \eta_{PC}$.

(g)Calculate the hydraulic power at point B, P_{HB}.

(h)Finally, determine P_2 at point B as $P_{2B} = P_{HB}/\eta_{PB}$.

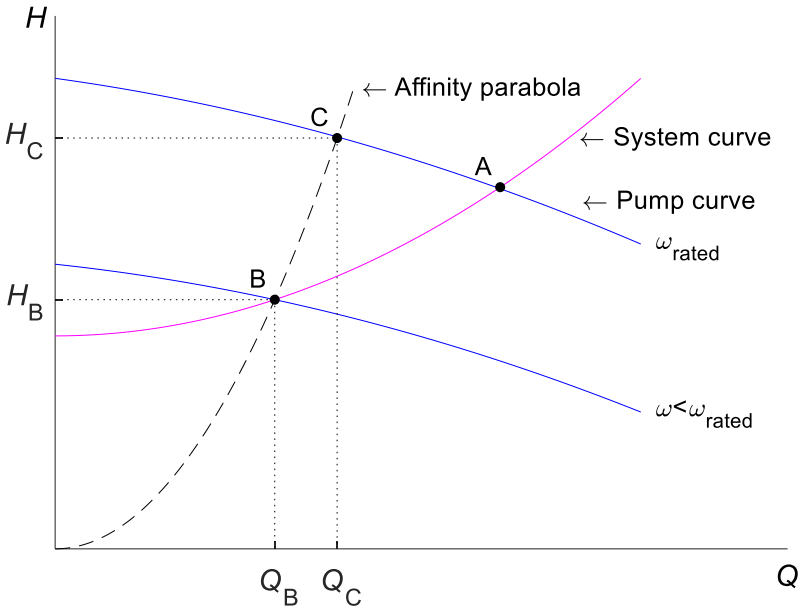


Figure 4.5. Illustration of the procedure to calculate the P2 required by the equivalent pump working at a certain point (QB, HB). Point A would be the operating point on the system curve if the pump were operating at the rated frequency, ω_rated. Point B is the actual operating point at a lower frequency. The pump works at the same efficiency at point B as at point C, therefore allowing P2 at point B to be calculated.

4.3.1.2 Calculation of P_{DC} at the Input of the Frequency Converter

The P_{DC} calculation depends on other elements present in the real system in which the pump operates, such as the pump motor, frequency converter, and the losses in the AC wiring between them. It is deduced from the value of P_{2B} according to the following algorithm:

(a)Determine the power at the input of the motor (P_1) at point B: $P_{1B} = P_{2B}/\eta_M(P_{2B})$, $\eta_M(P_{2B})$ being the efficiency of the motor at P_{2B}.

(b)Determine the power at the output of the frequency converter (P_{AC}), given the AC wiring losses W_{AC} at P_1: $P_{AC,B} = P_{1B}/W_{AC}(P_{1B})$.

(c) Determine P_{DC}: $P_{DC,B} = P_{AC,B}/\eta_{FC}(P_{AC,B})$, $\eta_{FC}(P_{AC,B})$ being the efficiency of the frequency converter at the load $P_{AC,B}$.

4.3.1.3 Selection of the Combination of Active Pumps That Maximizes the Pumped Water Flow

To obtain the highest water flow rate at the available DC PV power, $P_{DC,mpp}$, a procedure is necessary to select the number of operating pumps and the value of their synchronized frequency.

If we take S samples from the system curve, for each of the S values of H, we calculate Z values of Q, P_2, and P_{DC} for each of the Z equivalent pumps resulting from the possible combinations of N pumps, where $Z = N$ as the N pumps are equal. Note that we will finally calculate S sets of Z values of Q, P_2, and P_{DC}.

The P_{DC}-Q curve of each of the Z equivalent pumps may be fitted with a third-degree polynomial:

$$Q(P_{DC}) = k_{q0} + k_{q1}P_{DC} + k_{q2}P_{DC}^2 + k_{q3}P_{DC}^3 \quad (62)$$

Figure 4.6 shows an example of these fitted curves for the case of $Z = N = 5$ equivalent pumps. Given an available P_{DC}, it can be observed how it is possible to choose the highest flow rate as the maximum value of the different $Q = f_z(P_{DC})$, where $z = 1..Z$.

Obviously, given a certain available $P_{DC,mpp}$, not all the Z equivalent pumps are eligible because each one of them works in a certain P_{DC} range; therefore, the selection procedure applies a series of restrictions:

(a) The minimum DC power of the equivalent pump (P_{DCmin}) that is determined by the minimum cooling water flow of the pumps (Q_{min}) that its manufacturer requires. This restriction disables some combinations of pumps. It should be noted that Q_{min} of the equivalent pump is different from N times the minimum one of the individual pump due to the higher working head in the system curve.

(b) The maximum DC power of the equivalent pump (P_{DCmax}), which is determined by the maximum operating frequency of each individual pump (ω_{max}). The equivalent pump is still eligible but is limited to this maximum operating frequency even if more power is available ($P_{DC,mpp} > P_{DCmax}$). Again, note that the

power demanded at this ω_{max} by the equivalent pump is different from N times that of an individual pump, also due to the higher working head in the system curve.

It is worth mentioning that we are considering frequency-synchronized pumps; therefore, when they use the same model of motor and frequency converter and there are the same wiring losses, each of the frequency-converter–wiring–motor-pump sets active at every moment demands the same DC power.

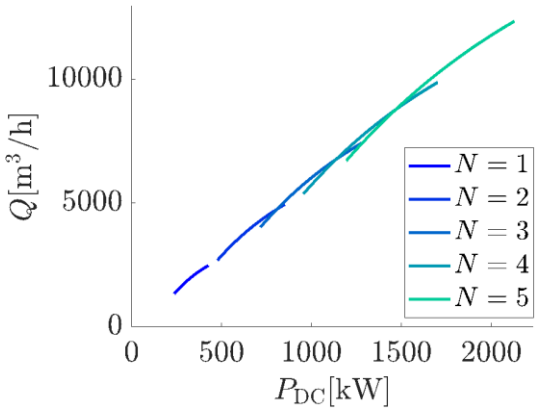


Figure 4.6. PDC-Q curves of each of the equivalent pumps of a group of five equal and synchronized pumps.

4.3.2 Configuration 2: Group of N Equal Pumps + Group of M Equal Pumps

In real PVISs, it is common to find pumping stations with two different groups of pumps. Typically, there is a group of N equal, high-power pumps driven by soft starters and therefore operating at their fixed nominal frequency. The other group consists of M equal pumps but of lower power than those of the previous group, and, in addition, they are driven by frequency converters, which allows them to work at a synchronized but variable frequency. It can also be found that the first group also has frequency converters and that, therefore, they can also work at a synchronized and variable frequency. Pump groups are modeled following the process described in configuration 1.

The number of active pumps in each group is selected again to maximize the pumped flow rate depending on the available PV power.

4.3.2.1 Selection of the Combination of Pumps

Dynamic programming (DP) was chosen as the selection methodology due to its suitable characteristics because this case (a) presents an optimal substructure, as an optimal solution for n active pumps meeting a water flow and head requirement contains a suboptimal solution for $n-1$ active pumps, and (b) presents overlapping subproblems because the power that a single pump demands when it is pumping a water flow at a given head may be part of several suitable solutions.

DP is applied in a bottom-up approach, where all possible small problems are solved and then combined to obtain solutions for bigger problems. DP is an optimization method based upon the use of Bellman's optimality principle (Bellman, 1957), which establishes that "*An optimal policy has the property that whatever the initial state and initial decision are, the remaining decisions must constitute an optimal policy with regard to the state resulting from the first decision*". As stated in (da Costa Bortoni et al., 2008) where DP is applied to optimize grid-connected pumps, this can also be expressed as: "*given an optimal trajectory from point A to point C, the portion of the trajectory from any intermediate point B to point C must be the optimal trajectory from B to C*" (Larson, & Casti, 1978).

Applying it to our case, this principle results in solving the recursive Equation (63):

$$f_z(x) = \min_{0 < x_z < x} [g_z(x_z) + f_{z-1}(x - x_z)] \tag{63}$$

with $z = 1,2, \ldots f_1(x) = g_1(x)\ x > 0$.

Where z corresponds to each combination of active pumps, with $1 < z < Z$; x corresponds to the constrained state variable, which is the required water flow, Q_s, at the system curve discretized in S samples (where $1 < s < S$), and therefore it implies a working head, H_s, that all z active pumps must meet; $g_z(x)$ is the state cost function, for this case, the demanded DC power by a single pump while pumping a water flow Q_z at H_s, $P_{\mathrm{DC},z}$; $f_{z-1}(x)$ is the cost of the rest of the path, hence the demanded DC power of the rest of $z-1$ active pumps, $P_{\mathrm{DC},z-1}$, pumping the rest of water flow, $Q_s - Q_z$ at H_s. Therefore,

$$P_{\mathrm{DC},z}(Q_s) = \min_{0 < Q_z < Q_s} \left[P_{\mathrm{DC},z}(Q_z) + P_{\mathrm{DC},z-1}(Q_s - Q_z)\right] \tag{64}$$

In this work, the aim is to maximize the volume of water pumped; therefore, for each instance, the highest flow rate Q_s where the required power $P_{\mathrm{DC},z}(Q_s)$ does not exceed the available power from the PV generator, $P_{\mathrm{DC,mpp}}$, is chosen. Therefore,

$$Q_{s,\max} = \max_{0 < Q_s < Q_S} \left[Q_{s|P_{\mathrm{DC},z}(Qs) \leq P_{\mathrm{DC,mpp}})} \right] \tag{65}$$

Each subset of active equal frequency-synchronized pumps can be reduced to an equivalent pump, as exposed above, simplifying the required calculation.

4.3.2.2 Subconfiguration 2.1: A First Group of N Pumps at Fixed Frequency and a Second Group of M Pumps at Variable Frequency

In this subconfiguration, the pumps in the first group work synchronized at a fixed nominal frequency, and the second group of pumps works synchronized at a variable frequency.

If the first group consists of N pumps and the second of M pumps, there are $Z = (N + 1) \times (M + 1) - 1$ combinations depending on the number of active pumps. The equivalent pumps for the combination of n active pumps of the first group, where $n = 0..N$, and for the combination of m active pumps of the second group, where $m = 0..M$, can be modeled using Equations (59) and (60). However, unlike in configuration 1, the points (H_n, Q_n) and (H_m, Q_m) where each group of pumps operates are not on the system curve.

If the system curve is discretized in S points (Q_s, H_s) where $1 < s < S$, for each H_s, the second group of pumps must pump the difference between the flow of the first group, Q_n, and the total flow Q_s at the height H_s (see Figure 4.7). The first group operates at the point (Q_n, H_s) of the equivalent Q-H nominal curve of n active pumps. The second group operates at the point $(Q_s - Q_n, H_s)$ on the equivalent Q-H curve of m active pumps at the frequency necessary to contain said point.

It is obvious that, in the case $n = 0$, or $m = 0$, the system is reduced to configuration 1, since only the pumps of the first group, or of the second group, are active, respectively.

As an example, Figure 4.7 shows the case $N = 2$ and $M = 1$ and the working point when $n = 2$ and $m = 1$ pumps are active at H_s.

Using the described procedure of selection of the combination of pumps, the active pump combination (n, m) that pumps the highest flow rate at the available PV power is obtained, and the combinations that demand more DC power or that would force the pumps to operate at frequencies outside of its range are discarded.

Figure 4.8 shows in red the Q-H locus where the second group of variable frequency pumps is required to work for each combination of n active pumps in the first group.

Shaded in gray, the locus for which there is no solution, i.e., for each head, the flow rate pumped by each pump group separately, or the combination of both, does not reach the required flow rate in the system curve. Obviously, when n= 0, this locus is the system curve itself.

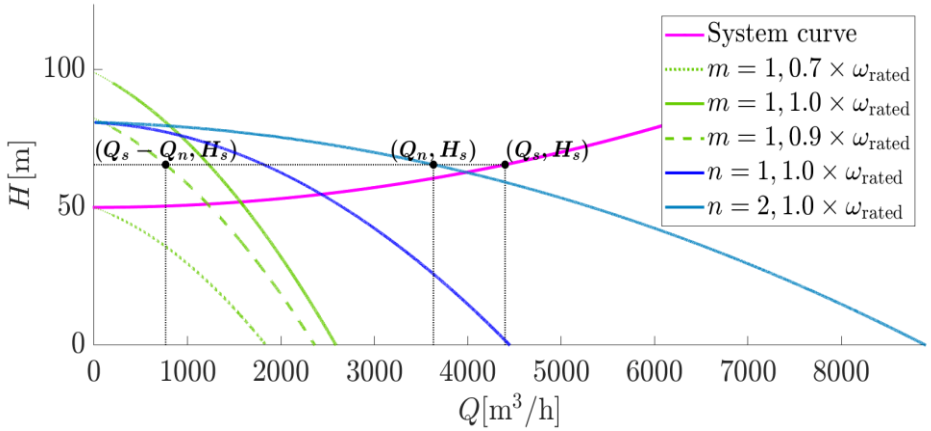


Figure 4.7. For the case N = 2 and M = 1, Q-H curves and the working point when n = 2 and m = 1 active pumps at Hs

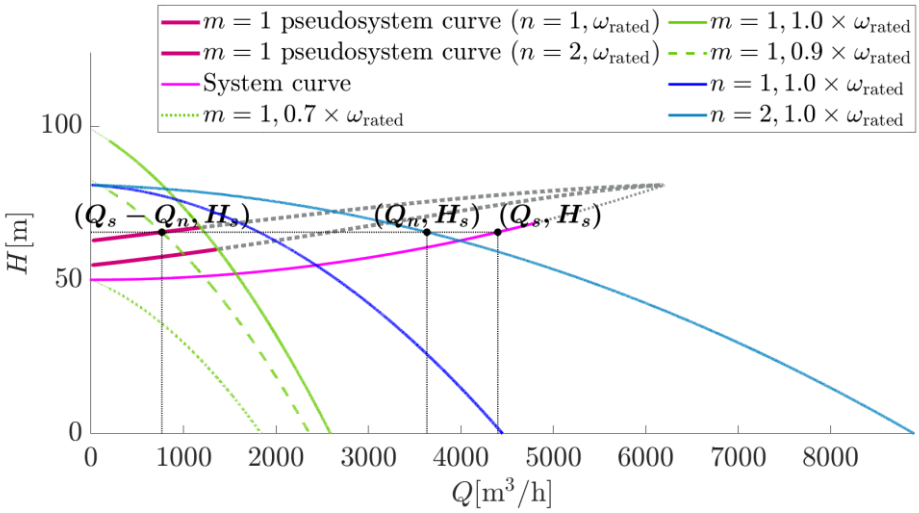


Figure 4.8 Q-H curves and working points for the case N = 2 and M = 1 and the Q-H locus where the second group of variable frequency pumps is required to work for each combination of n active pumps in the first group

This set of z_n locus (H, Q) of the second group of pumps can be modeled with third-degree polynomials that would constitute z_n "pseudo system curves" for the second group of pumps (Equation (66)).

$$H(Q) = k_{z_{n0}} + k_{z_{n1}} Q + k_{z_{n2}} Q^2 + k_{z_{n3}} Q^3 \tag{66}$$

The point of this pseudo curve at H_s determines the frequency of the second group of m active pumps.

Figure 4.9 shows the P_{DC}-Q curves for each combination of (n, m) active pumps for the case $N = 2$ and $M = 2$, where Q is normalized to its maximum value. For each combination, the flat part of the curve corresponds to all active pumps operating at their maximum (nominal) frequency.

Figure 4.10 allows analyzing the operation of the system showing, depending on the available P_{DC}, (a) the rate flow normalized to its maximum value (blue line in both Figure 4.10a,b), which is the envelope curve of Figure 4.9; (b) the chosen combination of (n, m) active pumps (dashed blue line in both Figure 4.10a,b); (c) the working frequency of the n-pump group normalized to its maximum value (orange line in Figure 4.10a); (d) the working frequency of the m-pump group normalized to its maximum value (yellow line in Figure 4.10a); (e) the ratio of P_{DC} demanded by the n-pump group, normalized to P_{DC} value (orange line in Figure 4.10b), i.e., 1 when the n-pump group is the only one operating and consuming all the power, 0.5 when both groups of pumps demand an equal power, and 0 when the n-pump group is stopped; (f) the power not used by the system, $P_{DC,mpp} - P_{DC}$ (yellow line in Figure 4.10b); and the efficiency of each group of pumps (dotted purple and green lines in Figure 4.10b) in terms of hydraulic power (P_H) regarding the DC power consumed by the group of pumps ($P_{DC,n \text{ or } m\text{-pumps}}$).

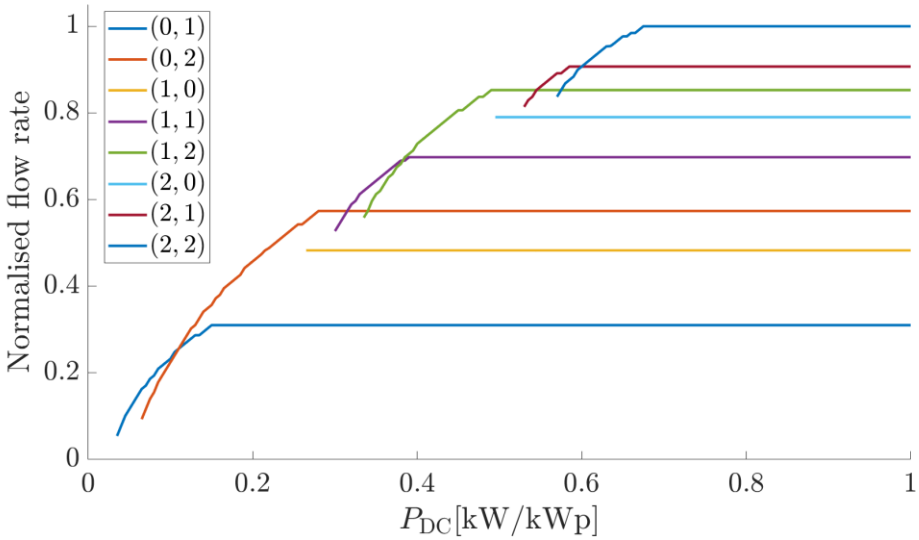


Figure 4.9. P_{DC}-Q curves for each combination (m, n) of active pumps for the case $N = 2$ and $M = 2$.

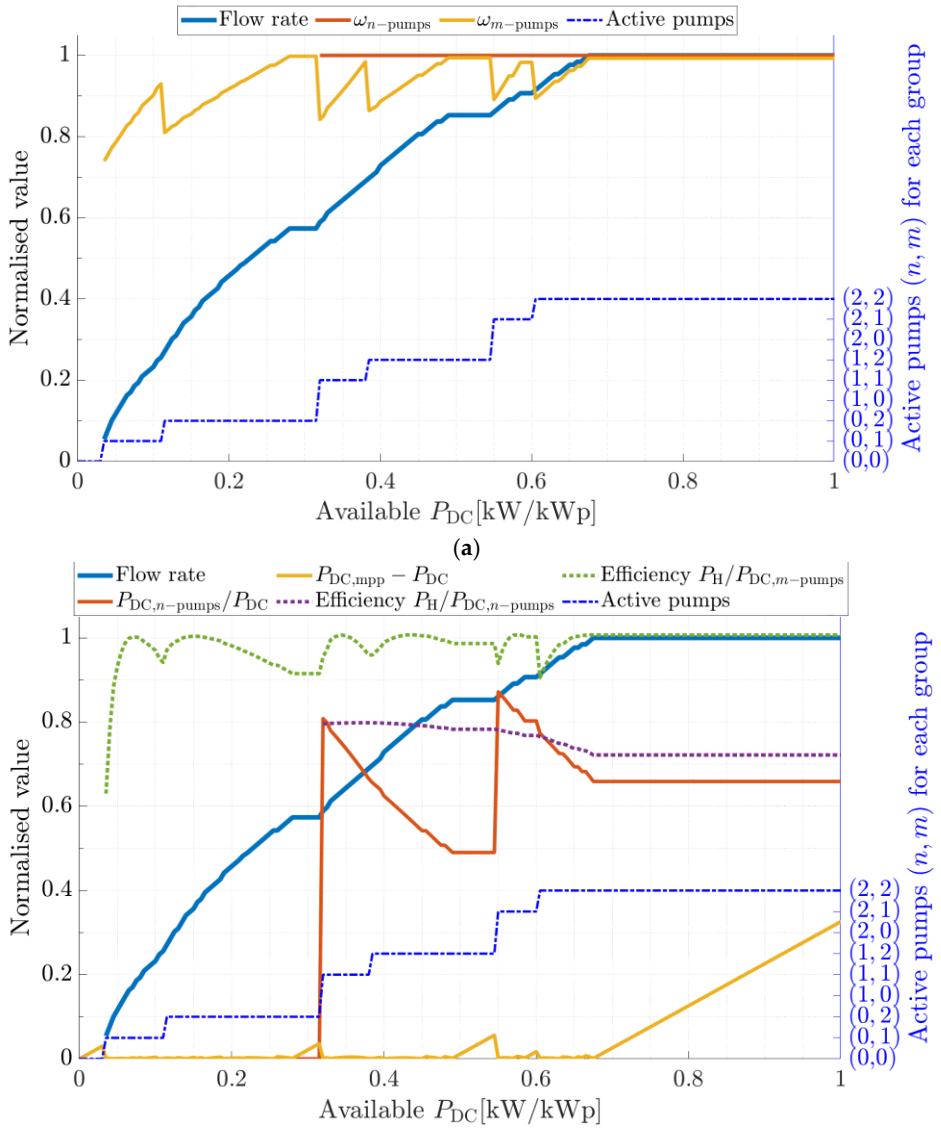


*Figure 4.10. For the case $N = 2$ and $M = 2$, combination of pumps that maximizes the water flow pumped depending on available P_{DC}, as well as the frequency at which the two groups of pumps will work; (**a**) operation view—working frequencies, (**b**) design view—efficiencies, power balance, not used P_{DC}.*

4.3.2.3 Subconfiguration 2.2: Two (or More) Groups of Pumps Working at Variable Frequency

This configuration consists of a first group of N pumps working at a variable synchronized frequency and a second group of M pumps also working at a variable synchronized frequency that does not have to be the same as the one of the first group.

Here, the case of two groups of pumps is modeled, but the model is valid for a greater number of groups.

In the same way as subconfiguration 2.1, each group of pumps is modeled with its equivalent pump and the number of active pumps in each group, n and m, and their frequencies are calculated by the same selection algorithm described there to maximize the water flow pumped at the available P_{DC}.

The only difference is that the selection algorithm is more complex, since the set of "pseudo system curves" for the different equivalent pumps of the second group of pumps is actually a "pseudo system area" because there is no single water flow rate for each equivalent pump of the first group of pumps, Q_n, at the head H_s, but there is a range of Q_n values since it can work at different frequencies and not only at the nominal frequency.

Figure 4.11 shows, for $N = 2$ and $M = 1$, the "pseudo system area" (pink area) when $n = 2$ and $m = 1$.

Figure 4.12 shows, for $N = 2$ and $M = 2$, the combination of pumps and their frequency that would maximize the water flow pumped depending on the available P_{DC}, together with the rest of the variables shown in Figure 4.10.

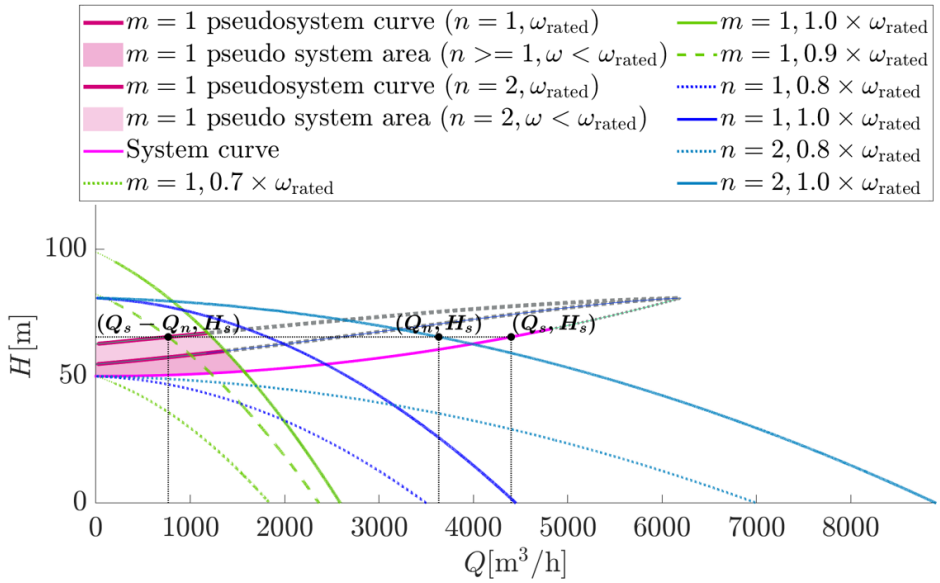


Figure 4.11. Q-H curves and working points for the case N = 2 and M = 1, and the Q-H "pseudo system area" where the second group of variable frequency pumps is required to work for each combination of n active pumps working at variable synchronized frequency in the first group.

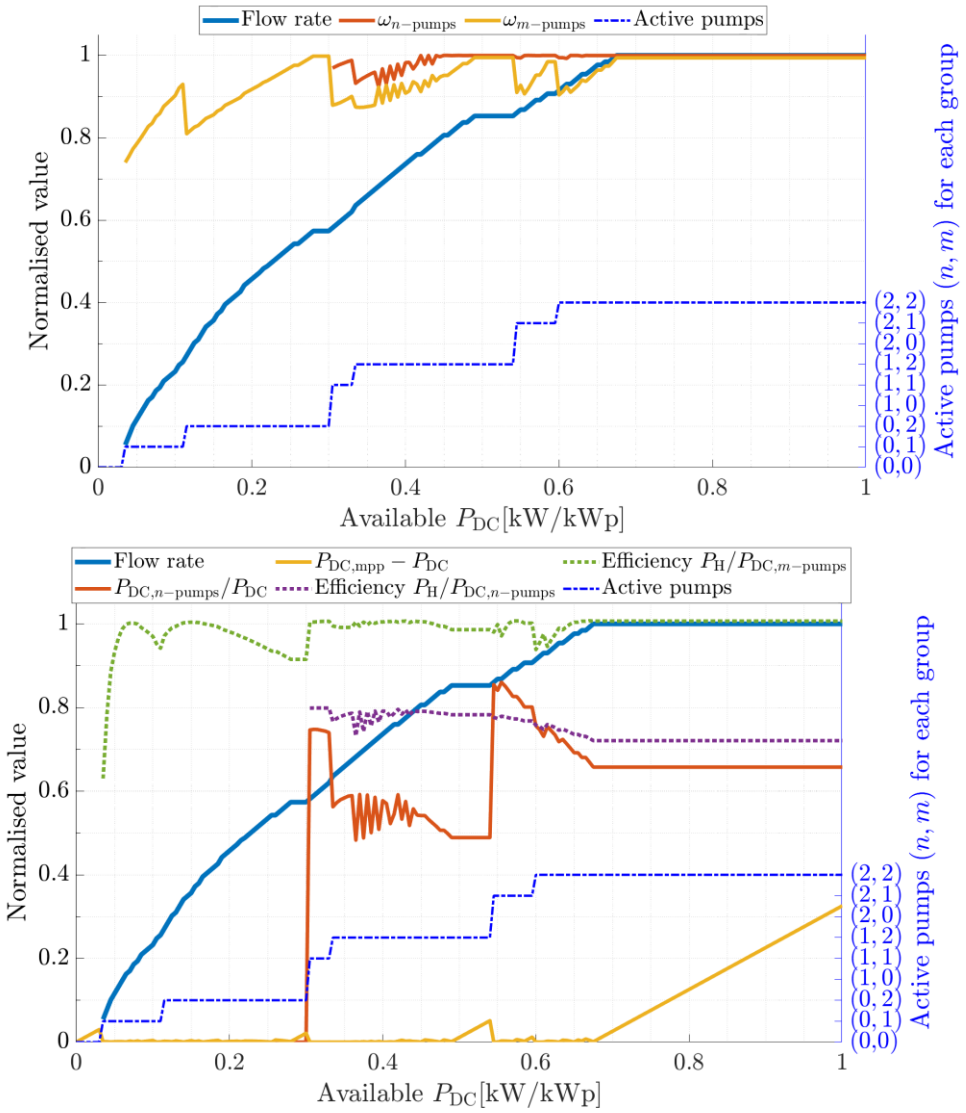
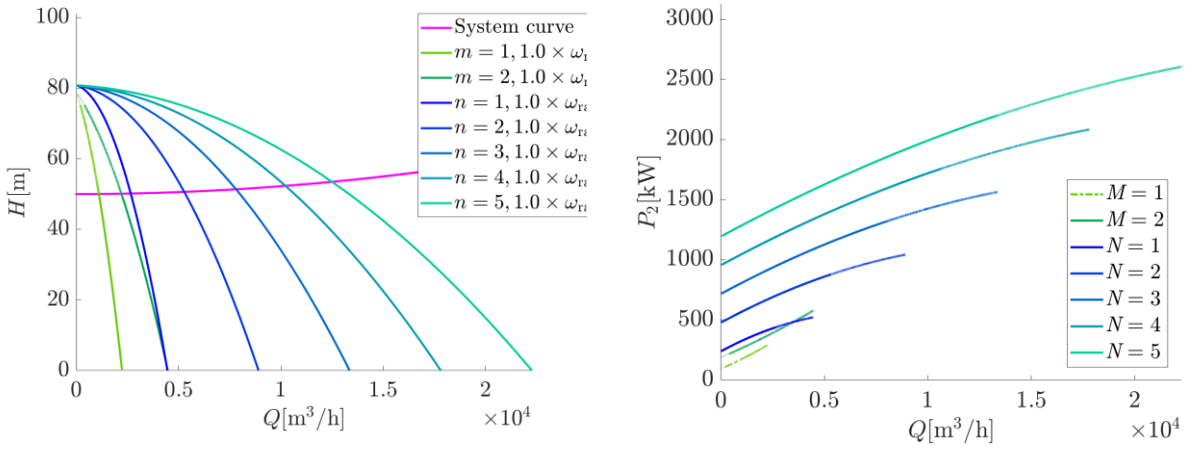


*Figure 4.12. For the case $N = 2$ and $M = 2$, combination of pumps that maximizes the water flow pumped for a certain available P_{DC}, as well as the frequency of the two groups of pumps; (**a**) operation view—working frequencies, (**b**) design view—efficiencies, power balance, non-useful P_{DC}.*

4.4 Results and Discussion

The described models were applied to a system to be installed in Monegros (Spain), lat = 41°30′03″ N, lon = 0°02125″ W, using the Typical Meteorological Year offered by PVGIS as meteorological data. This system consists of a first group of five equal frequency-converter–motor-pump sets, each with a rated power of 500 kW, and a second group consisting of two frequency-converter–motor-pump sets with a lower power of

200 kW. Both groups share a 3625 kW_p PV generator mounted on a North-South horizontal axis tracker. Figure 4.13 shows the characteristic curves for each $(n, 0)$ and $(0, m)$ combinations of active pumps, as well as the system curve.



(**a**) (**b**)

*Figure 4.13. H-Q and P_{DC}-Q characteristic curves—(**a**) and (**b**), respectively—for each of the equivalent pumps for $N = 5$ and $M = 2$*

Three different analyses are performed, and their results are discussed.

In Section 4.4.1, the difference in pumped volume is compared when considering several frequency-converter–motor-pump sets connected to independent PV generators, with respect to the same number of sets sharing the complete PV generator.

Section 4.4.2 analyzes the difference in the water volume pumped based on the type of frequency control used, specifically, frequency-synchronized groups of motor pumps with respect to the ones operating at different frequencies, either both variable or one of them at their fixed nominal frequency and the other one variable.

Finally, Section 4.4.3 describes the pumped volume expected for the complete system $(N = 5, M = 2)$ using subconfigurations 2.1 and 2.2 in order to observe the difference in production when the first group operates at nominal frequency vs. when operating at variable frequency, in both cases complemented by a group of $M = 2$ small pumps synchronized at variable frequency.

4.4.1 Independent PV Generators vs. Shared PV Generator

Existing simulation tools were just able to simulate a single frequency-converter–motor-pump set by adapting its frequency to the available power from a PV generator

with rated power P_{nom1} (hereafter referred to as the base case, Figure 4.14a). Therefore, to simulate a group of N pumps synchronized at a variable frequency and sharing a PV generator of rated power $N \times P_{nom1}$ (hereafter referred to as the N-case, Figure 4.14b), the volume pumped simulated in the base case was multiplied by N. It was known that this assumption is somewhat erroneous because, in conditions of low irradiance (early and late morning or cloudy days), the volume pumped in the N case should improve the volume pumped in the base case. It was because, at certain times, the base case PV generator may not generate enough power to activate the pump but N times this power (N case) could be enough to activate a subset of the n pumps, $0 < n < N$, even if it was not enough to activate all N pumps.

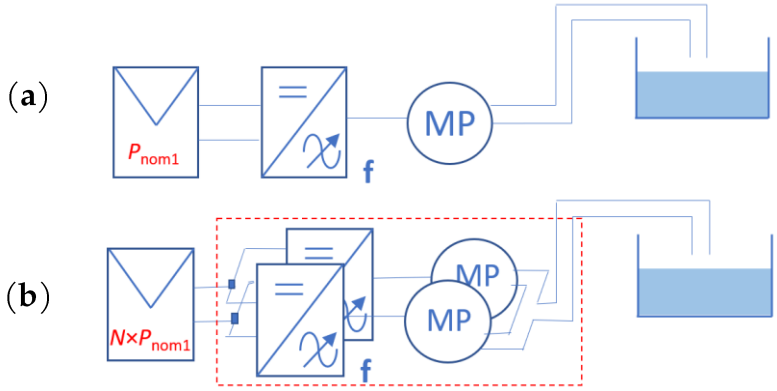


*Figure 4.14. (**a**) A single pump connected to a single PV generator of P_{nom1}. (**b**) Group of N pumps sharing a single PV generator of $N \times P_{nom1}$.*

Using the model described in configuration 1, it is possible to observe this gain. For this purpose, the first set of large pumps ($N = 5$) was simulated and compared to the base case ($N = 1$). Figure 4.15 shows the evolution of the yearly gain, varying $N = [1, 5]$, in relative terms, when the hydraulic piping system is also resized (solid line), to obtain similar friction losses for each N. It can be observed that this gain reaches the value of 8.5%. The "piping system resized" gain is representative of an irrigation system with well-designed pipes with an appropriate diameter.

The "piping system unchanged" gain (dotted line in Figure 4.15) is representative of systems without the possibility of widening the diameter of the water distribution pipes and therefore increasing the friction losses when increasing N. In this case, in the multipump simulation (N case), not only no gains are obtained but also losses of 44.8% with respect to the traditional simulation method (base case and multiplying by N).

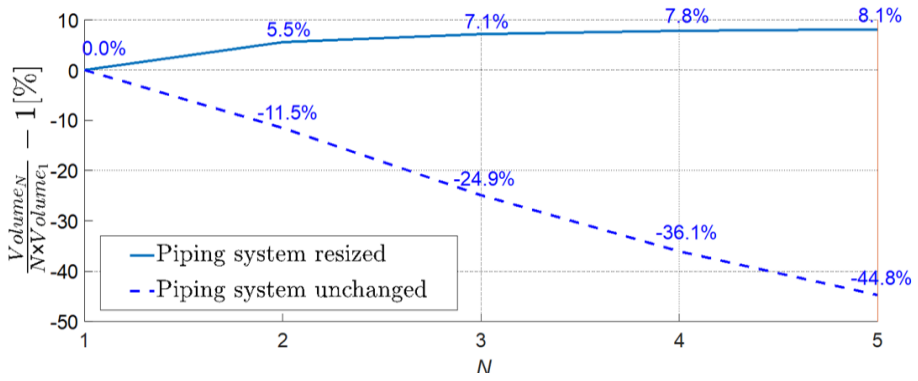
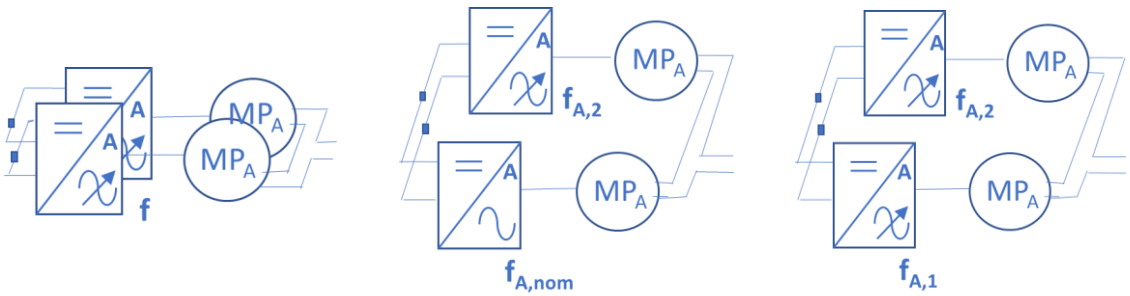


Figure 4.15. Relative gain of the volume pumped in the N case with respect to the base case with and without resizing the hydraulic piping system.

4.4.2 Performance vs. Type of Frequency Control

Here, the models developed are used to compare the difference in the volume of water pumped as a function of the type of frequency control implemented. For simplicity and to better observe the results, only two of the higher power pumps (500 kW) are considered ($N = 2$). Three frequency controls are applied, as shown in Figure 4.16: (a) both pumps work synchronized at a variable frequency; (b) one pump works at a constant (nominal) frequency, and the second pump works at a variable frequency; and (c) one pump works at a variable frequency, and the second pump also works at a variable frequency, which can be different. Control (a) is modeled by defining a single group of two pumps synchronized in frequency and applying configuration 1. Controls (b) and (c) are modeled using configurations 2.1 and 2.2, respectively, with the singularity that both groups of pumps contain the same model of pump. This allows simulating different frequencies in each group. Figure 16 illustrates the three controls, respectively. In all the cases, the PV generator and the hydraulic system are shared.



(**a**) (**b**) (**c**)

*Figure 4.16. Three possible frequency controls under comparison: (**a**) both pumps work synchronized at a variable frequency, (**b**) one pump works at a constant (nominal) frequency, and the second pump works at a variable frequency, and (**c**) one pump works at a variable frequency, and the second pump also works at a variable frequency, which can be different.*

Table 4.1 shows some relevant yearly results: potential DC energy yield of the PV generator working at maximum power point (MPP) without the limitations imposed by the motor pump, actual DC energy yield because of the pump limitation, AC energy yields at the input of motor, hydraulic energy yield and water volume obtained over a typical meteorological year.

As expected, controls (a) and (c) where both pumps are running at variable frequency show a higher annual volume than control (b) (>8%), and control (c) slightly exceeds control (a). The differences come when there is enough power available to activate more than one pump but not yet enough for all pumps to be active and at their nominal frequency and have two complementary causes:

(a) In control (b), there is a larger range of $P_{DC,mpp}$ values that cannot be fully exploited, mainly because there is not enough power available yet to start the large pump at its nominal frequency while the small pump is already operating at its nominal frequency.

(b) The efficiency of the converter, wiring, motor, and pump assembly is different for each duty point. In case (c), there are duty points corresponding to two pumps working at different frequencies that provide more total water flow than the other duty points with frequency restrictions (either one pump is forced to nominal frequency or both pumps are forced to equal frequencies). In other words, the higher efficiency of one pump can compensate for the worse efficiency of the other pump and overcome the combination where both pumps must operate at the same efficiency. The final gain is small compared to control (a) but appreciable. This gain improves if the number of pumps is increased. In the literature, some studies can be found in which this gain is neglected and the $P_{DC,mpp}$ is assumed to be equally distributed between both pumps, perhaps due to the impossibility of

predicting a different distribution, as this requires a solution such as the one proposed in this work, using dynamic programming.

Obviously, it depends on the parameters of the system elements. Furthermore, when applied to different sites, the different frequency distribution of the power available at the site can amplify or minimize each effect.

Table 4.1. Simulated yearly relevant results for each type of control

	Frequency Control Type		
	Control (a) $N = 2$ (Variable)	**Control (b) $N = 1$ (Nominal) $M = 1$ (Variable)**	**Control (c) $N = 1$ (Variable) $M = 1$ (Variable)**
Potential DC energy yield at MPP, $E_{DC,MPP}$ (kWh/kWp)	2057.9	2057.9	2057.9
DC energy yield, E_{DC} (kWh/kW$_p$)	1936.3	1924.0	2036.9
$E_{DC}/E_{DC,MPP}$ ratio	0.950	0.935	0.990
AC energy yield at the motor-pump input, E_1 (kWh/kW$_p$)	1859.7	1747.7	1860.5
Mechanical energy yield at the pump input, E_2 (kWh/kW$_p$)	1690.0	1567.1	1690.7
Hydraulic energy yield, E_H (kWh/kW$_p$)	1439.5	1326.2	1440.1
Annual water volume yield (m^3/kW$_p$)	9868	9141	9872

4.4.3 Performance of a Study Case N = 5 and M = 2

Here, the real system in Los Monegros is simulated. Two cases are considered: (a) $N = 5$ (at nominal frequency), $M = 2$ (at a variable frequency) and (b) $N = 5$ (at a variable frequency), $M = 2$ (at another variable frequency). The nominal power of the shared PV generator is 3625 kW (AC/DC ratio = 0.8).

Table 4.2 shows the yearly results of both configurations. The difference in annual pumped water flow is 2.1% in favor of control (b). Control (a) allows the large pumps to operate at nominal frequency, with the second group of pumps operating at variable frequency to adapt the water flow to the available P_{DC} at any given time. This control (a), therefore, protects more the reliability of the large pumps, which operate at nominal power without a significant loss of productivity, and simplifies the control of both groups of pumps.

Table 4.2. Simulated yearly results for the two configurations in Los Monegros.

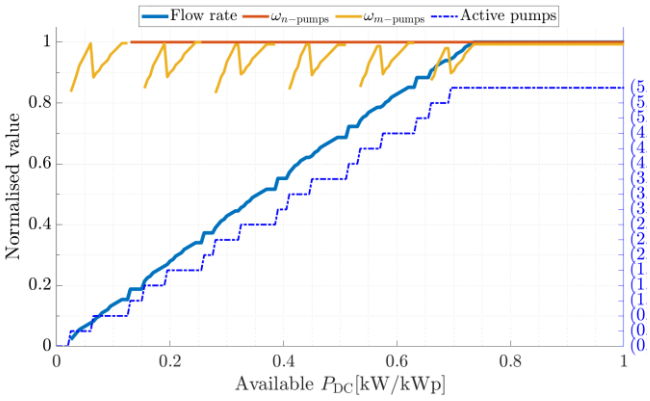
	Control (a)	**Control (b)**
Potential DC energy yield (at MPP), $E_{DC,MPP}$ (kWh/kWp)	2057.9	2057.9
DC energy yield (MPP), E_{DC} (kWh/kWp)	1990.3	2000.1
$E_{DC,MPP}/E_{DC}$ ratio	0.967	0.972
AC energy yield at the motor-pump input, E_1 (kWh/kWp)	1922.5	1936.2
Hydraulic energy yield, E_H (kWh/kWp)	1553.1	1586.3
Annual water volume yield (m^3/kWp)	10,741	10,962

Figure 4.17 is very useful to analyze the performance of the system in the two cases. In the design view (Figure 4.17b and Figure 4.17d), dotted blue lines show the active pumps depending on the available PV power while red lines show the ratio of the total power consumed by the active pumps of the group *N*, and some relevant conclusions can be drawn from their analysis. For example, the lower number of steps in the dotted blue line of control (b) indicates a lower number of start–stop events of the pumps with the variation of the available PV power, which is beneficial from the point of view of long-term reliability of motor pumps.

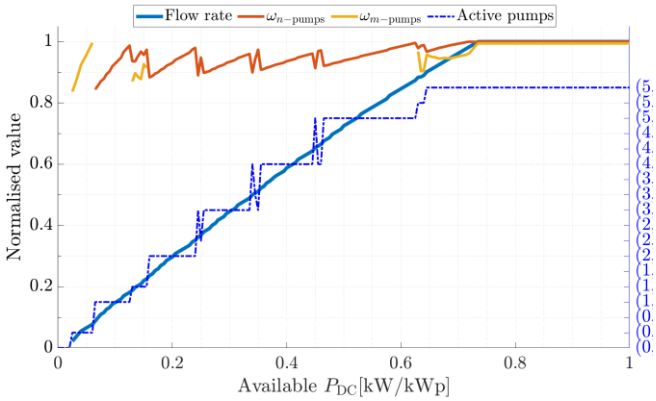
The analysis of the orange lines in design views shows how in control (b), and for values of normalized available PV power less than 0.6, the larger pumps (the ones of group *N*) absorb the whole available power, except for very low available PV power. This means that large-power pumps are more efficient, and their use is preferable to small-power pumps. However, in case control (a), an increased use of small pumps is required as the large ones must work just at nominal frequency. This is the reason why case control

(b) shows better yearly results in Table 4.2. However, this increase in performance comes at the price of having five more frequency converters.

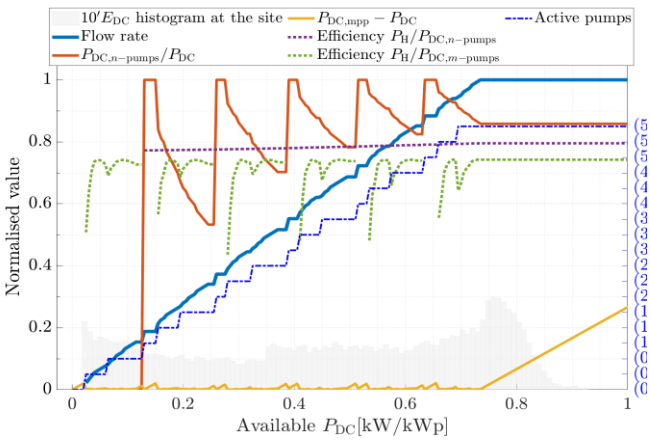
Operation view (Figure 4.17a and Figure Figure 4.17c) is not only useful for simulation purposes but also to implement the control algorithms when installing the real PVIS.



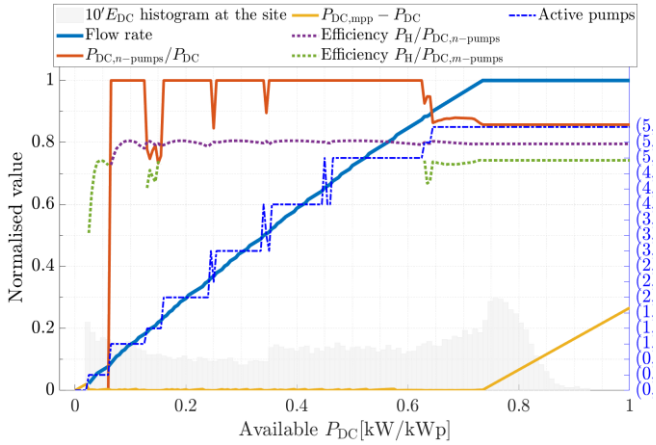
(**a**) Operation view for control (a)



(**c**) Operation view for control (b)



(**b**) Design view for control (a)

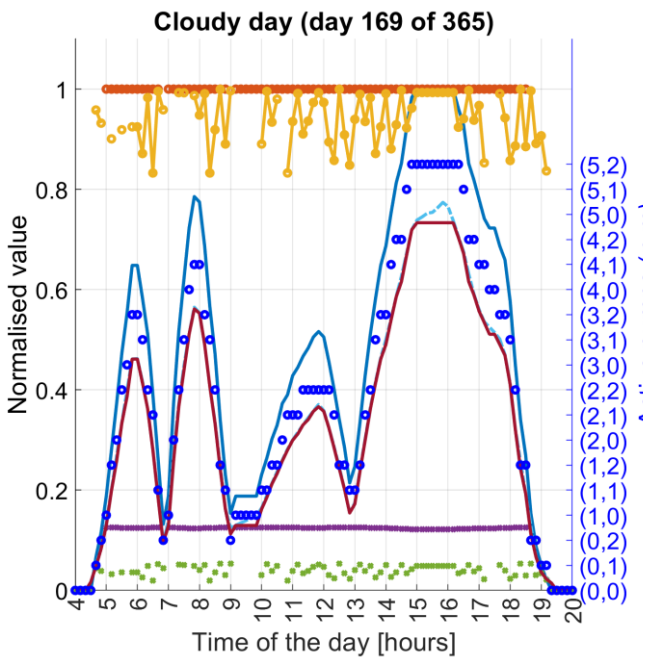


(**d**) Design view for control (b)

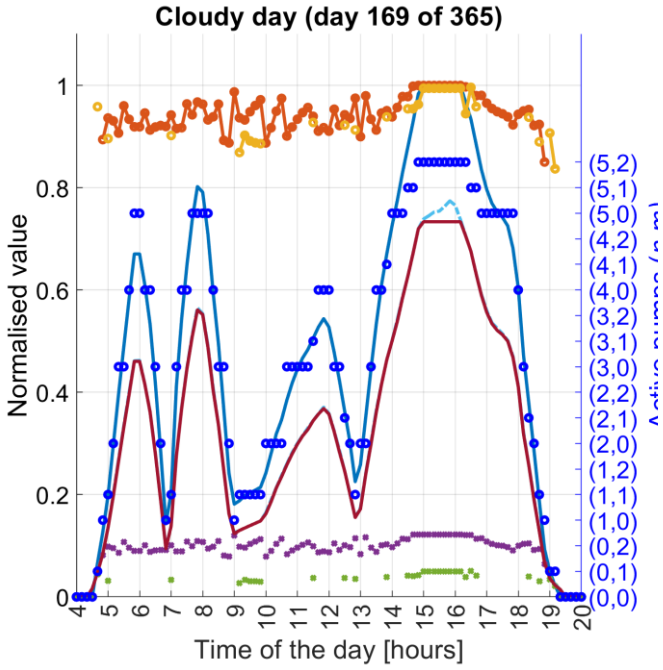
*Figure 4.17. Combination of pumps that maximizes the water flow pumped for a certain available P_{DC}, as well as the frequency at which the two groups of pumps will work in control (**a**)—n pumps at nominal frequency and m pumps at variable frequency; and in control (**b**)—n pumps at a variable frequency and m pumps at other variable frequency.*

Figure 4.18 allows an analysis on a daily basis. A clear day and a cloudy day were selected, and both of the above controls were applied. From the point of view of the greater volume of water pumped in this work, it can be seen that the origin of the difference in favor of control (b) shown in Table 4.2 comes mainly from the greater

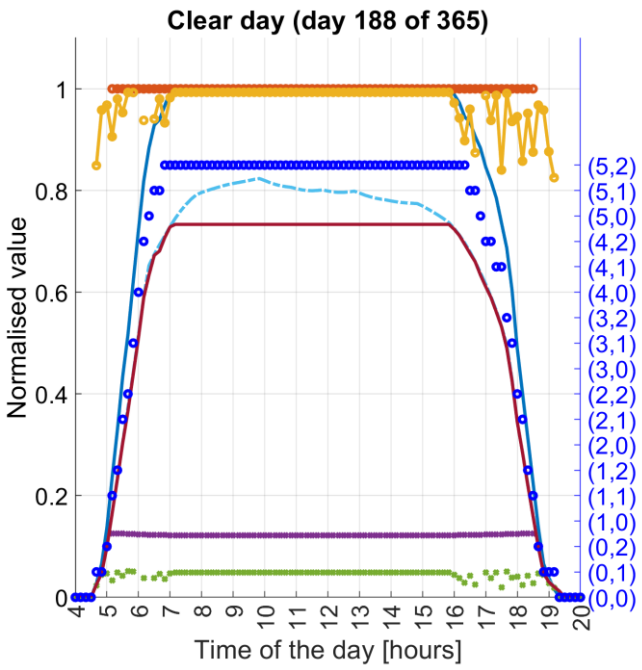
production of the system on cloudy days or in conditions of average irradiance. For example, on the cloudy day 169 of 365, control (b) (Figure 4.18b) manages to pump 29.9 m^3/kW_p compared to 28.1 m^3 for control (a) (Figure 4.18a), i.e., 6.4% more. Part of this difference is due to the higher efficiency of the pump at working points in control (b) (dotted blue and red lines in Figure 18), but another part is due to the fact that 1.67% of the available daily energy could not be used because there was no possible working point for the system in control (a) (yellow line at design view in Figure 4.17), compared to 1.0% of the daily energy not used in control (b), mainly at the beginning and end of the day. In contrast, in high-irradiance conditions, such as day 188 of 365, control (b) (Figure 4.18d) manages to pump 45.9 m^3/kW_p vs. 45.1 m^3/kW_p of control (a), only 1.7% more. This better result in pumps synchronized in frequency with respect to some pumps working at nominal frequency coincides with what has been stated by other authors for the case of grid-connected systems (Viholainen et al., 2012).



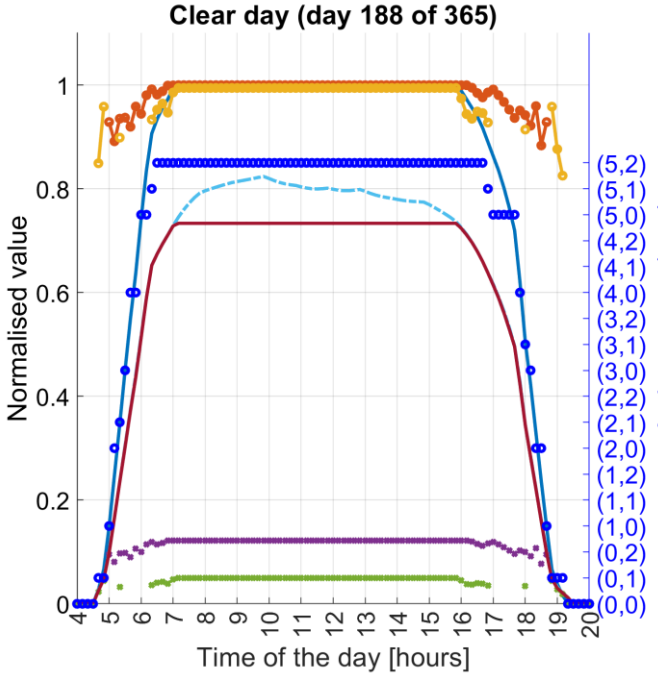
(**a**) Cloudy day, control (a)



(**b**) Cloudy day, control (b)



(**c**) Clear day, control (a)



(**d**) Clear day, control (b)

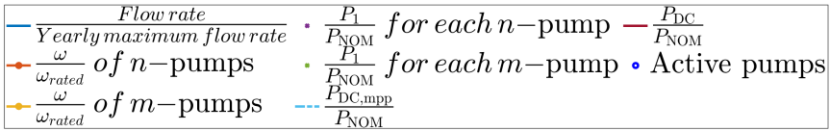


Figure 4.18. Cloudy and clear day. Case $N = 5$ and $M = 2$. (As there are two groups of different pump types, the best combination (with the chosen criteria) can include 0 or more active pumps in each group. A line disappears (discontinuous effect) in those combinations where there are 0 active pumps in one of the groups.)

The use of this tool to better adapt the design of the system to the climatology of the PV generator location and the greater complementarity between large and small pumps in pursuit of one or more objectives, such as minimizing the number of starts/stops, reducing the number of frequency converters needed, better withstanding fades in irradiance due to passing clouds, taking advantage of all the energy that the PV generator can produce at its maximum power point, or forcing higher-efficiency duty points for some pumps are some of the main advantages of the models developed in this thesis.

4.5 Conclusions

The growing market of large-power PVISs to power pumping stations, with several pumps, even of different models and nominal powers, working in parallel, requires simulation tools with the capability of estimating the productivity of these multipump systems. This was precisely one of the objectives of this thesis: to develop simulation models of multipump PV irrigation systems, show their usefulness with respect to the current state of the art, and apply them to the analysis of a case study.

Three models were developed for the most common configurations of the existing pumping stations for irrigation.

The advantage of these models over the current state of the art was shown. First, the greater precision of using multipump models was shown when there are N motor pumps sharing a single PV generator. In the case of negligible hydraulic friction losses, the use of the multipump model shows gains with respect to the state of the art in which a single motor pump connected to a $1/N$ fraction of the PV generator is simulated and the result multiplied by N. However, in the case of appreciable friction losses, the current state of the art overestimates the productivity of the systems.

Second, the ability of these models to compare different multipump designs was shown. It was illustrated with the comparison of different solutions by analyzing the productivity of the three proposed configurations. The result of the comparison between subconfigurations 2.1 and 2.2 shows better performance of the second one (8% in the example used), that is, in favor of the option of two groups of pumps working at variable frequencies instead of one of the groups working at nominal frequency. In return, one of the groups operating at nominal frequency, generally the one made up of larger pumps, could present long-term reliability advantages.

Finally, the models were applied to a real PVIS in Los Monegros, Spain, which has a pumping station with two different groups of pumps. The results of simulating two different configurations (subconfigurations 2.1 and 2.2) allowed us to analyze the advantages of each one. Particularly relevant are the graphical results that allow one not only to analyze the performance but also serve as a basis for the design of the control algorithms of the real system.

These models were implemented in the free-access SISIFO simulation tool.

This work opens the door to future lines of research for the optimization of these models. For example, the graphical tools shown in this chapter could be used for:

(a) Better selecting the large and small pumps in each group to seek greater complementarity in order to minimize the number of pump starts/stops;

(b) Better withstanding fades in irradiance due to the passage of clouds;

(c) Better adapting to the climate of the site;

(d) Taking advantage of all the energy that the PV generator can produce at its maximum power point;

(e) Limiting the working point of the pumps to efficiency ranges close to their best efficiency point;

(f) Reducing the number of frequency variators required;

(g) Combining several of these objectives, sometimes conflicting, as long as the required pumped water flow during the irrigation period can be met.

Chapter 5

THE SISIFO SIMULATION SOFTWARE TOOL AS AN OPEN ACCESS TOOL

"En cuestiones de cultura y de saber, solo se pierde lo que se guarda; solo se gana lo que se da." (Antonio Machado)

5.1 Introduction

5.1.1 Background

The simulation software SISIFO, then known as IESPRO, was born as an in-house tool for modelling grid-connected PV systems at IES-UPM in 2005. It was implemented as a monolithic application developed in MatLab©. As such, it could only be used by those who had access to its source code, in this case only the Instituto de Energía Solar. It allowed the productivity of PV systems to be estimated on the basis of meteorological data for a site and the characteristics of the components (modules, generator, inverters, transformers). The PV generator of these plants must meet certain constraints (reproduce a periodic pattern —same row spacing and same height, have a sufficient number of rows) for the models to be applicable. This software only allowed grid-connected PV systems to be modelled. The adjustment of their productivity expectation with reality was adjusted through measurement campaigns and from real PV plant operation data (at that time, these plants aggregated around 300 MW_p).

5.1.1.1 Progress made during the European PVCROPS project

In the context of the European PVCROPS project (European Commission, CORDIS, 2012), years 2012-2015, it is renamed SISIFO. It will be maintained as a monolithic version in MatLab©. It continues to allow only grid connected PV systems (Muñoz et al., 2013). It evolves during this project by incorporating several aspects, among which the following stand out:

- The possibility of hybridisation with diesel systems (Muñoz & Carrillo, 2015).
- Incorporation of a clear sky model (Muñoz & Perpiñan, 2016).

In addition, the first steps have been taken to allow any user to use the tool online without having access to the source code of the tool. To this end, a web application was developed that was completely independent of the original Matlab© code. This web application did not have all the features available in the Matlab© code, but it had enough functionality to simulate a grid connected PV system.

This web application was implemented entirely in the PHP scripting language (Carrillo et al., 2015). It consisted of:

- A web interface that collected part of the input parameters through web forms and another part through an Excel file with a defined format that had to be provided (a downloadable template was provided). The main results (annual, monthly and daily) of each simulation were presented graphically.
- Functions for calculating the simulation results. The source code, also in PHP, was actually a translation of MatLab©. Considering the appearance of the source code in MatLab© at the beginning of this thesis, it is likely that since PHP does not have vectorial calculation capacity, it was decided not to use this capacity in MatLab© as well, since an iterative version facilitates this translation.

5.1.1.2 Progress made during the European MASLOWATEN project

Between 2015 and 2018, the SISIFO simulation tool will be further developed in the framework of the European MASLOWATEN project (European Commission, CORDIS, 2015; *MASLOWATEN*, n.d.). The main developments include:

- The simulation capability of a PVIS, consisting of a PV generator, a single frequency inverter and a single motor/centrifugal pump assembly, was

incorporated into the main Matlab© software of SISIFO (Munoz et al., 2015). This change meant acting on all stages of SISIFO. Firstly, because these PVIS do not have transformer stages. Second, because they have frequency converters instead of central inverters. Thirdly, because the motor/centrifugal pump set cannot always consume as much energy as the generator could provide at its maximum power point, so the operating point of all the components (PV generator, frequency converter, motor), electrical losses, etc. must be recalculated so that the power produced by the PV generator matches the power required by the pump at each moment.

- The ability to simulate a PV generator consisting of arrays with a delta structure has been added (Almeida, Narvarte, et al., 2018). This proposed generator allows obtaining more constant daily profiles of irradiance in the inclined plane throughout the day. This is particularly interesting for PVIS, as in certain cases it allows to increase the pumped volume with respect to a static PV generator facing south.

These developments were not incorporated into the PHP web application that enabled SISIFO to be used online, so they were not publicly available. In order to do this, it would have been necessary to recode the entire web application in PHP due to the large number of changes.

5.1.2 Starting point and aims

This thesis takes up the development of the SISIFO simulation software at the aforementioned point in time, the year 2018, in the final phase of the MASLOWATEN project. The aim was to enable the free and open online use of as much of SISIFO's functionality as possible. In particular, at least the simulation of the productivity of PVIS should be possible via the web interface.

The advantages and disadvantages of the SISIFO simulation software at that time were analysed. Focusing on the aspects related to the web application that allowed its online use, the main drawbacks identified are listed below:

- Usability of the interface. Some of the input parameters were provided by an Excel file. The user had to download and complete certain templates. The other part of

the parameters were collected through web forms. These templates, which were known internally at IES-UPM, were somewhat complex for any uninitiated user.

- Performance. As Matlab© is a product specialised in vector and matrix calculations, the time needed to calculate the simulation results could be reduced by using the Matlab© version of SISIFO compared to the PHP version (which uses iterative calculations). However, it is worth noting that in reality the Matlab© version of SISIFO also omitted the matrix computation. One could speculate that the reason for this was either to facilitate a more direct translation from the Matlab© source code to the PHP source code, or to not require special matrix programming skills on the part of the researchers.
- Partial functionality. Only part of the functionality offered by the Matlab© tool had been transferred to PHP. In particular, all the developments carried out in the MASLOWATEN project between 2015 and 2018, which affected most of the SISIFO code, as described in the previous section, had not yet been transferred.
- Development process. The coexistence of two versions in different programming languages, Matlab© for the full simulation tool and PHP for the web application, complicates the development process in several ways:
    - Each evolution had to be addressed in two different languages. In addition, the different capabilities of the two languages (vectorial vs. iterative) mean that the translation to PHP was not straightforward, thus creating new potential points of failure.
    - Researchers required programming skills in both languages.

  The software development and debugging process was slowed down and made difficult.

Consequently, the following secondary objectives of this thesis are directly related to the online access to the SISIFO simulation software:

- To collect all the parameters in a more user-friendly way, by means of web forms, eliminating the use of Excel files.
- To facilitate the automatic retrieval of certain parameters (meteorological data, characteristics of motors and pumps, variators, etc.) from online databases.

- To develop a web interface that allows a more complete use of the simulation software, at least in its two main applications: grid-connected systems and PV pumping systems.
- To find a solution that exploits the strengths (performance) of each platform while simplifying the development and debugging process and avoiding translation between programming languages.

The following sections briefly describe the general aspects of the current SISIFO simulation software architecture that enable the proposed objectives to be achieved. It is not intended to explain the internal design of the individual components. Consequently, they are not described individually and in detail using any modelling language.

The SISIFO web interface is available at https://www.sisifo.info.

5.2 Architecture

In order to achieve the goals, a different architecture was implemented in 2018. Specifically, a relatively simple microservices architecture (MSA). Figure 5.1 shows the typical elements of such an architecture. As described in (Fowler, 2014), an MSA is "*an approach to developing a single application as a suite of small services, each running in its own process and communicating with lightweight mechanisms, often an HTTP resource API. These services are built around business capabilities and independently deployable by fully automated deployment machinery*".

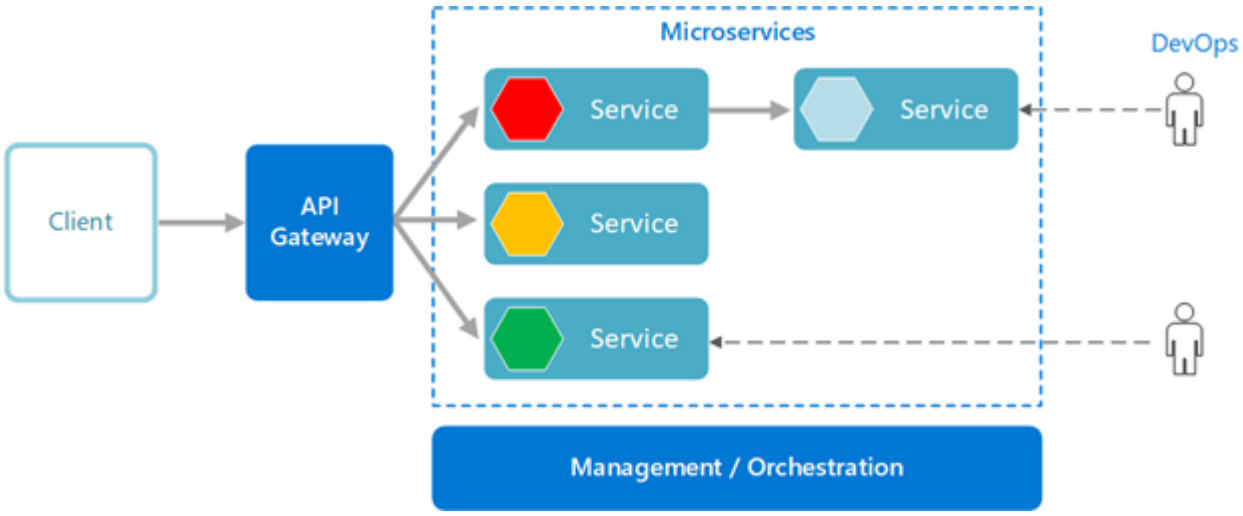


Figure 5.1 Generic example of microservices architecture. Source: (Microsoft, n.d.)

In the following, the elements considered most interesting in the context of this thesis are described in order to show the evolution of the simulation tool. Others related to the maintenance or operation of the architecture are not mentioned.

5.2.1 Simulation engine

It was decided to continue using MatLab© as the simulation engine, taking advantage of both the researchers' experience with this technology and its optimised performance for vector/matrix computations.

The new models explained in the previous chapters were incorporated into this engine.

While this engine could be decomposed into a number of independent microservices, for the time being it continues to operate as a monolithic version (a single logical executable). This aspect will be revisited when considering possible future work beyond this thesis.

5.2.2 Web interface based on a single page application (SPA) model

In this thesis, a new web interface has been designed. Its first version was implemented in 2018. It completely replaced the previous PHP web interface. It extends the open access functionality of SISIFO by incorporating the advances added to the engine during the European MASLOWATEN project. In particular, the possibility to simulate PVIS and delta-structured generators. It has also been possible to connect, via an API, to the databases of the pump manufacturer Caprari, a participant in this European project. Since then, the SISIFO web interface has made it possible to search the Caprari catalogue for motors and pumps suitable for the application and to obtain their characteristic parameters.

In the period 2018-2023, it has been the work of this thesis to guide and carry out the evolution of this web interface in several directions:

- Incorporating the contributions of this thesis described in the previous chapters.

- Adding other behavioural models available in the state of the art.
- Adding new capabilities or configurations whose suitability has been identified in the context of some work on productivity estimation of large PV plants that I have had the opportunity to carry out as a service in parallel with this thesis. These are new PV plants in the feasibility analysis phase. This allows us to observe reality and new trends and to adapt the tool accordingly.

It should be noted that each new feature requires the collection of a different, and usually larger, set of input parameters and the display of additional output results of the simulation performed. The web interface only does this, the interface to the engine that implements the models that support the new feature.

This web interface has been designed using a single page application (SPA) model. A brief guide to traditional vs. single page applications can be found in (Adobe Experience Cloud, n.d.). In short, an SPA runs directly in the web browser, does not need to be re-rendered during use, and usually relies on APIs to communicate with the server. Its main advantage is that it usually provides a smoother user experience.

The simulation SPA is surrounded by some static web pages with help, a presentation of the tool, some statistics, etc.

This SPA dynamically renders the different screens (views) according to the needs of the users navigating the application.

The front-end of this web interface uses HTML/CSS/JavaScript, mainly through the free and open-source Bootstrap framework, which is oriented towards responsive front-end web development. Its back-end is developed using an object-oriented programming paradigm. It uses the C# language and runs on the Microsoft© .NET platform.

5.2.3 Simulation microservice

A microservice is defined that provides access to the simulation engine. Like any microservice, it provides its service through a predefined contract (API). As the simulation engine evolves, versions of this microservice can be added to use each new version of the engine. This makes it possible to run different versions at the same time and, consequently, it is not necessary to update the clients with each evolution of the engine. A lightweight mechanism (in this case the HTTP protocol) is used for communication between the microservices.

The implementation of this microservice uses an object-oriented paradigm, in C# language on Microsoft© .NET architecture.

As a curiosity, due to the important effort that this change implied in the framework of the work of this thesis, it is worth mentioning that this microservice in C# language accesses the simulation engine in Matlab© through the Matlab© MWArray library, an option recommended at the time of the microservice implementation. In 2021, when integrating the multi-pump simulation capability into the microservice, a problem was discovered that forced the abandonment of the recommended library. In particular, due to the increase in the number of parameters and results, a memory leak was observed in the MWArray library. This prevented the extension of the microservice until it could be replaced by another library which, although more limited (requiring major modifications to the source code), did not have this drawback[7].

This microservice is used by several clients:

- The SISIFO SPA web interface. Call one of the versions of this microservice to obtain simulation results.
- Other external applications that could call this microservice to request the results of a simulation. This option allows, among other things, to
    - Easily create specific applications that request a large number of simulations from a version of the engine. Typically, the objective is to observe the result obtained by varying different input parameters.
    - Integrate the use of SISIFO as a simulation tool into any existing external application of any organisation.

This use by external applications is limited in order to be able to monitor and limit the load required by the simulation of large batches of simulations. Providing dedicated servers for this use, so as not to interfere with the simulations required by the web interface, is a trivial task with the proposed architecture.

Another relevant feature of this microservice is that it allows the simultaneous execution of several Matlab© instances (several independent simulation engines) on the

[7] Since 2022, Matlab© already recommends a new alternative (ref.MWarray,accessed 2023) instead of MWArray, which seems to solve this problem. We have not yet included it in the microservice.

same server. In this sense, it is worth mentioning that a pool of Matlab© simulation engines has been defined. Each invocation of the microservice waits until one of the simulation engines of the corresponding version is free and then requests the simulation. These engines are reused in other invocations of the microservice to avoid the long initialisation time required before the first simulation can be run. After a certain number of executions, they are recycled to avoid possible memory leaks in the Matlab© environment.

Figure 5.2 shows, in a simplified sequence diagram, the use of the microservice both from the web interface (as a consequence of a simulation request from a user) and without a web interface (directly from any other application with access to the microservice).

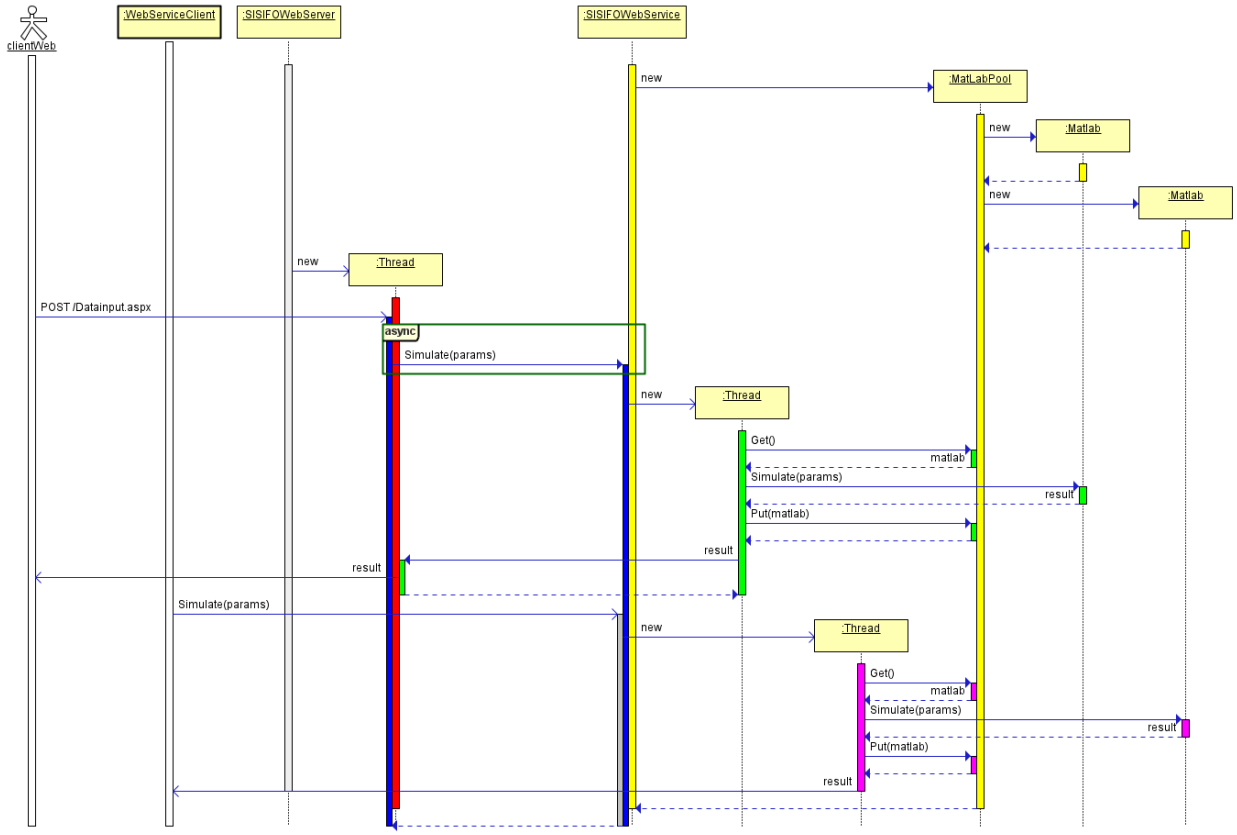


Figure 5.2 Sequence diagram of the concurrent execution of simulations by the microservice.

5.3 Volumetry and usage statistics

5.3.1 Volumetry

(a) The backend of the web interface, running on the .NET platform, consists of about 13,600 lines of C# code.

(b) The simulation microservice, also running on the .NET platform, consists of about 2500 lines of C# code.

(c) The Matlab© simulation engine consists of over 20,000 lines of MatLab© source code.

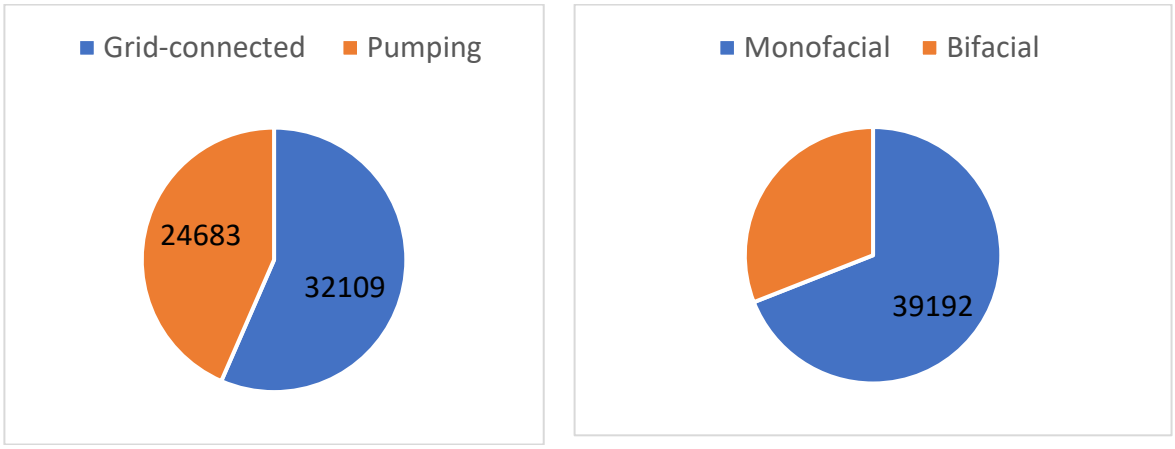
Points (a) and (b) have been fully implemented in this thesis. The work on point (c) has focused mainly, but not only, on those parts of the engine that are related to the contributions presented in the previous chapters.

5.3.2 Statistics

The statistics on the website are not as interesting as a brief analysis of some aggregate characteristics of the simulations that have been successfully completed through the online web interface of the SISIFO tool.

Figure 5.3a shows that 43.5% of the completed simulations correspond to PV irrigation systems. And 56.5% were grid connected PV systems. This indicates the growing interest in this PV application.

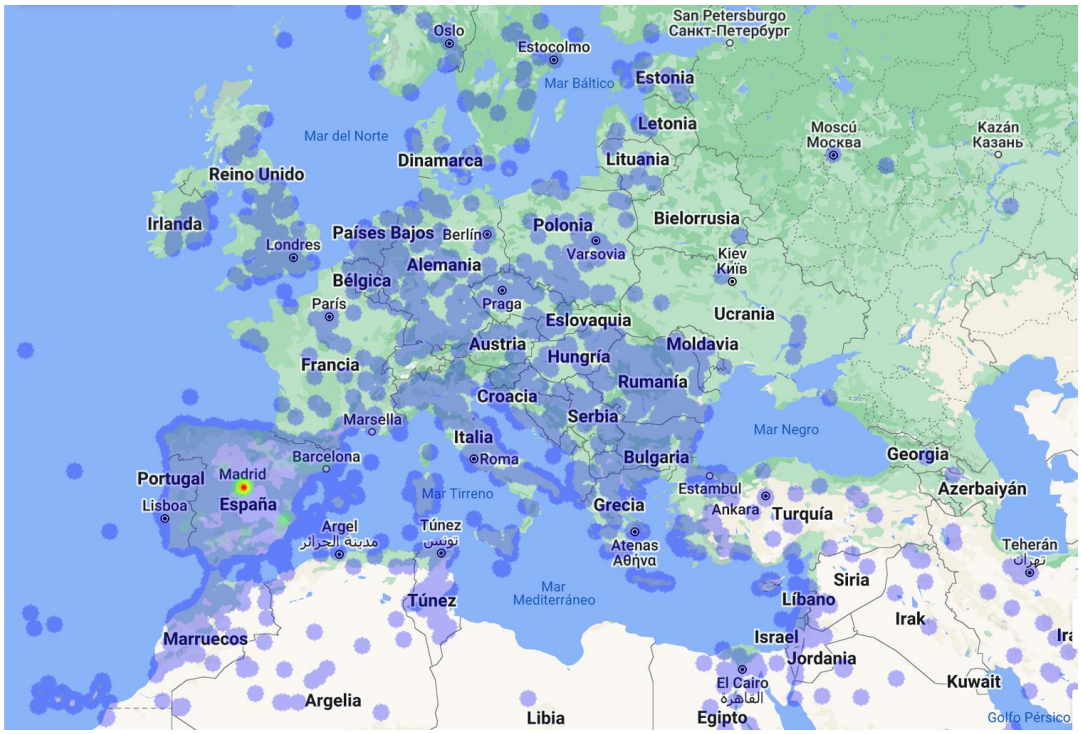
In the period 2018-2020, 38% of the simulations correspond to bifacial systems. Figure 5.3b shows that this percentage decreases to 31% in the period 2018-2023. This is mainly due to the fact that most of the simulated small-size PVIS used monofacial PV generators.



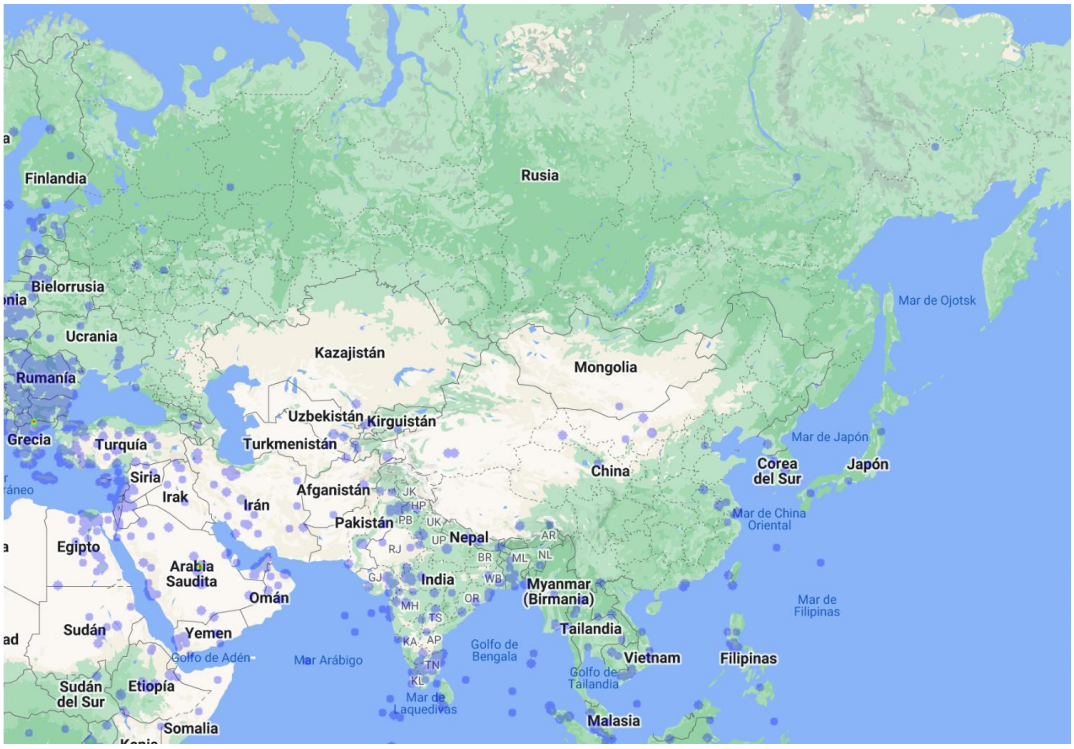
(a) (b)

Figure 5.3 Number of full simulations as a function of (a) the PV application and (b) the bifaciality.

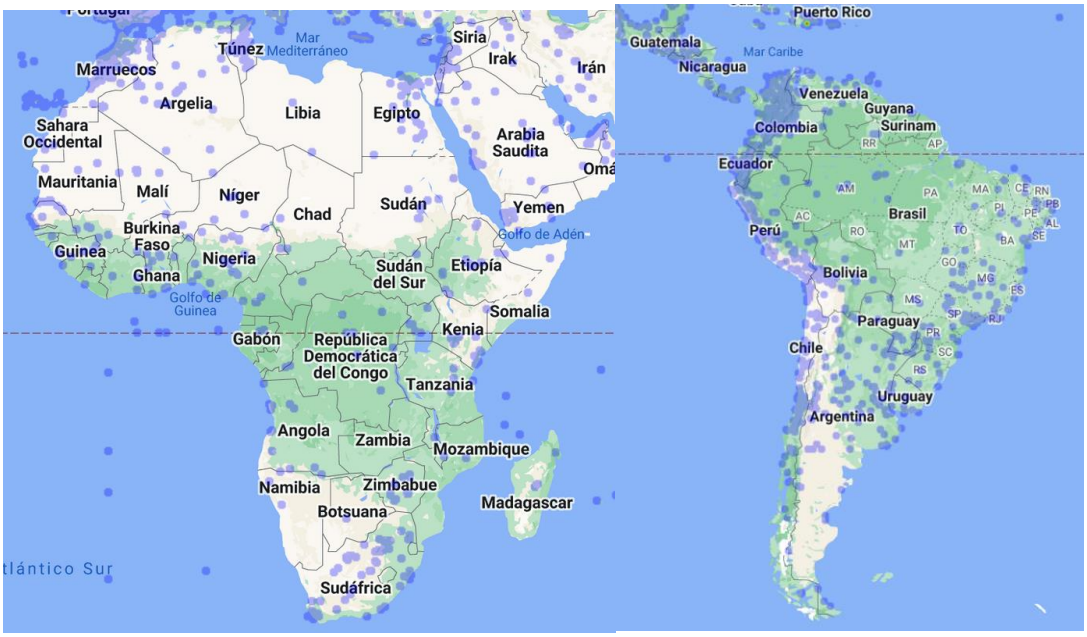
Figure 5.4 shows the distribution of simulated locations across continents, which can be accessed in the statistics section of the SISIFO online web interface.



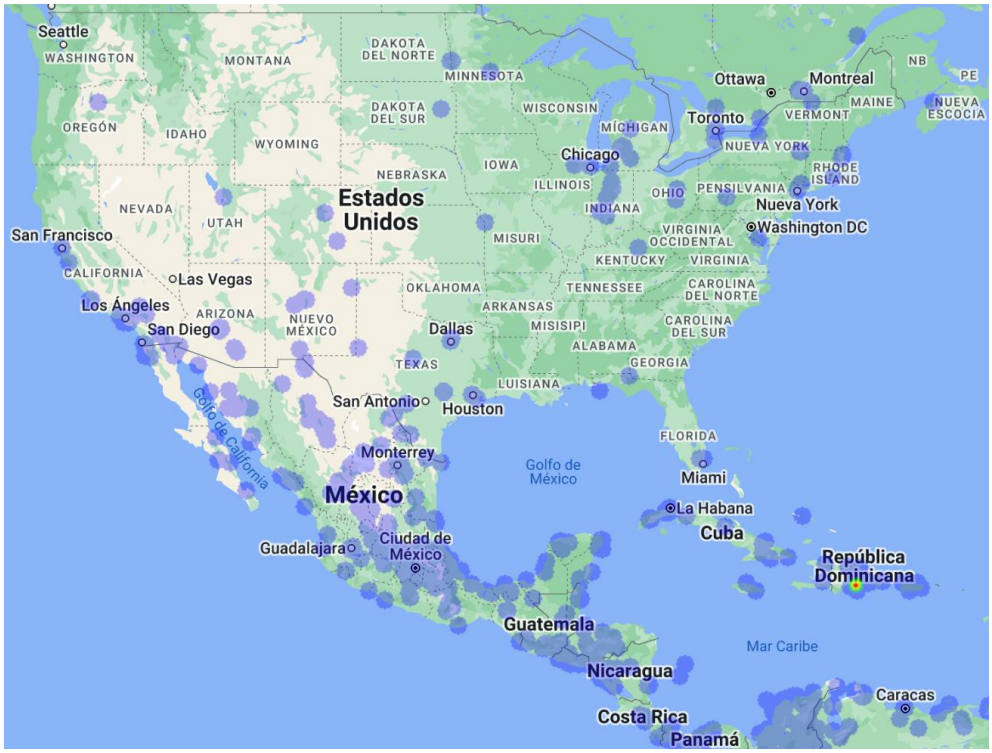
(a)


Finlandia
Rusia
Bielorrusia
Mar de Ojotsk
Ucrania
Kazajistán
Mongolia
Rumanía
Uzbekistán
Kirguistán
Grecia
Turquía
Turkmenistán
Mar de Japón
Corea del Sur
Japón
China
Siria
Irak
Afganistán
Irán
Pakistán
Mar de China Oriental
Egipto
Nepal
Arabia Saudita
India
Myanmar (Birmania)
Omán
Mar de Filipinas
Sudán
Yemen
Tailandia
Golfo de Adén
Mar Arábigo
Golfo de Bengala
Vietnam
Filipinas
Sudán del Sur
Etiopía
Golfo de Tailandia
Mar de Laquedivas
Malasia
Somalia

(b)


Mar Mediterráneo
Túnez
Siria
Irak
Irán
Marruecos
Argelia
Libia
Egipto
Arabia Saudita
Sahara Occidental
Mauritania
Malí
Níger
Chad
Sudán
Yemen
Golfo de Adén
Burkina Faso
Guinea
Nigeria
Ghana
Sudán del Sur
Etiopía
Golfo de Guinea
Somalia
Kenia
Gabón
República Democrática del Congo
Tanzania
Angola
Zambia
Mozambique
Namibia
Zimbabue
Madagascar
Botsuana
Sudáfrica
Puerto Rico
Guatemala
Mar Caribe
Nicaragua
Venezuela
Guyana
Colombia
Surinam
Ecuador
Brasil
Perú
Bolivia
Paraguay
Chile
Uruguay
Argentina

(c) (d)



(e)



(f)

Figure 5.4 Simulation location distribution across the different continents (a) Europe (b) Asia, (c) Africa (d, e) South and North América (f) Oceania

5.4 Conclusions

The new architecture allows a clear separation:

- The SISIFO simulation software engine, in Matlab© language, in which IES-UPM researchers have experience.
- The web interface, in any other programming language (in this case C#), which allows collecting the input parameters, requesting a simulation to the microservice using its API, and displaying the results graphically. The researcher does not need to know the language of this interface.

Both elements are decoupled by using the simulation microservice. This allows multiple versions of the microservice and the engine to be maintained, using the mutithreading capabilities of the .NET implementation of microservices to allow concurrent simulations without using Matlab© products.

In addition, this architecture allows for three different types of clients:

(a) Users who, through the web interface, request simulation exercises from anywhere in the world without knowing the code that performs such a simulation.

(b) Application type clients who, with prior authorisation, can directly access the simulation microservice to simply request a series of successive simulations, for example by varying some of the input parameters, from anywhere in the world and without knowing the code that performs such simulations.

(c) Developer users who, with their own local Matlab© instances, can use or develop the SISIFO Matlab© engine.

For the time being, this architecture meets the initial objectives. Installed on a server with multiple execution cores, it allows multiple simulations to be run concurrently. The simulation microservice typically completes each simulation (with hourly data) in less than 5 seconds. Regarding the secondary objective of enabling connection to online databases, it is currently possible to obtain online weather data from PVGIS (or import SolarGIS files), skyline elevation data from PVGIS, frequency converter data (Omron) and motor/centrifugal pump data from Caprari.

Chapter 6

CONCLUSIONS AND FUTURE WORK

As this thesis deals with contributions on relatively different and independent topics, each chapter has its own specific conclusions. This chapter provides an overview of these, as well as the degree to which the intended objectives have been achieved, and a brief list of possible future work that could continue or extend the work presented here.

6.1 Conclusions

As already indicated in the introduction, new contributions in the field of modelling and simulation of PV systems are still an open question and this thesis has mainly focused on this aspect of PV engineering. Using PV simulation software, productivity expectations are created. Subsequently, the analysis of the reality will allow improving the behaviour models and optimising the loss scenarios.

The resurgence of bifacial modules (essentially all high-efficiency PV cells are bifacial, so it was a matter of allowing radiation to hit the back side in a technically and economically feasible way), together with early experimental studies and analyses that created expectations of bifacial gain over monofacial modules that exceeded the price increase of bifacial modules over their monofacial counterparts, led to great interest and uncertainty in the PV industry at a time when simulation tools had not yet implemented behavioural models that would allow estimation of such gain. A notable achievement at the time was the development of a bi-dimensional model to calculate the back irradiance

of large bifacial PV installations, which has already been described in this thesis. Once incorporated into IES-UPM's SISIFO simulation software, it was one of the first, to our knowledge, to achieve this capability. When applied to large PV installations, this model produced results lower than those published in the state of the art, values that were later shown to be close to reality. The results were disseminated at a workshop organised by IES-UPM in 2020, attended by hundreds of companies and organisations in the PV sector from several countries.

In the publication of this model, we take the opportunity to highlight the historical importance of the period between 1984 and 1989 in Spain, forgotten by the state of the art, as it marked the beginning of the industrial production and commercial application of bifacial PV modules. This period saw the birth of the concept of the "vision factor", an idea imported from traditional heat transfer analysis. It is the basis for many of today's bifacial PV models. As a curiosity, during the review process of the article, some reviewers proposed to extend this historical perspective and Dr Eduardo Lorenzo, as a participant in these first steps and also in these last ones, published it in (Lorenzo, 2021). Integrated in the simulation tool SISIFO, the proposed model simplifies the complex geometry of PV arrays into a regular pattern. The model takes into account not only ground reflections, but also back-row reflections and sky irradiance, providing a complete perspective of the back-light distribution.

A second objective of this thesis has also been achieved, namely to be able to model the irradiance received in the plane of the generator in non-horizontal terrain. This case has two secondary objectives: 1) to obtain the tracking angles in sloping terrain that allow avoiding mutual shading between rows, and 2) to extend the bifacial gain calculation expressed in the first objective also to this type of terrain (mainly in the rear face of the module, where its contribution is more relevant, but also in the front face). The first secondary objective already had some solution in the state of the art. Our contribution consists of three main aspects a) to obtain an alternative calculation formula that evolves the one previously published by IES-UPM researchers for horizontal terrain, which could be useful for the various tracker software based on the latter, and b) to provide an additional calculation method that, by means of a third rotation matrix, simplifies the horizontal terrain formula and allows it to be used also for inclined terrain, with certain nuances as described above, and c) by obtaining the same angles with this calculation as

with other algorithms published in the state of the art, it contributes to validating the result of both calculations. The second secondary objective, the bifacial gain on sloping terrain, is particularly complex. Although it has been available in SISIFO since 2022, it was possible to simplify its calculation in 2023 after incorporating the rotation matrix mentioned above. In this case, as there was no known software that allowed the bifacial calculation, the result could not be validated with respect to other references, but obtaining the same result after implementing it in two different ways allows, in a way, to reinforce its validity and the process helped to better understand some of its characteristics. A few months ago, one of the commercial software packages, PVsyst, included this simulation possibility in its latest version, also using a two-dimensional model based on view factors, without further details being known.

The work carried out in this thesis has allowed us to go beyond the initial objective proposed (i.e. trackers with N-S axis on sloping terrain in an east-west direction). Thus, it is possible to simulate the bifacial gain in any terrain orientation (given the orientation and the slope of its line of maximum slope, or its two slopes in N-S and E-W direction, either of the two ways of defining the terrain plane), with the tracker axes in any orientation, and requiring only the following restrictions to be kept: a) the equispacing (pattern periodicity) of the trackers and b) that the axis of the trackers be parallel to the terrain. This has led to novel and unexpected results, such as the fact that the traditional N-S orientation of the axes is not always the most convenient for certain PV plants, depending on the slope and orientation of the terrain, the physical separation of the trackers, their physical limits of rotation, the hourly irradiation distribution that the TMY of the site determines, and other parameters of the PV generator (not only physical, but also optical or electrical, such as the angular response of the module, losses - or gains - in conditions of low irradiance, etc.).

The availability of this model has allowed us to apply it to calculate the productivity estimate of a 200 MW_p PV plant in Portugal, currently under construction. The proposed approach, based on the pre-calculation of the annual electrical productivity loss of the PV plant located in different terrain orientations, with respect to a horizontal configuration, and the power distribution of the PV plant in each orientation, allows to simplify the design and estimation process and helps to make decisions about the earthworks and the layout of the PV plant. In this PV plant, a detailed calculation was also made for the

different generators (in different orientations, with different module and power models for each string), how they are connected to each inverter in the plant, how the inverters are connected to each of the medium voltage transformers (taking into account that certain inverters may be saturated, for example because they receive energy from generators located on south-facing land, while other inverters do not, so they provide different amounts of electrical energy). The much more complex detailed calculation requires, in addition to an extensive specification, a non-negligible amount of computation time (30 minutes of computation time for a system where a single orientation simulation requires only about 8 seconds) and yet gives very similar results to the proposed simplified approach (a difference of less than 0.6% in annual electricity productivity for this particular PV system).

Regarding the third main objective of this thesis, i.e. the simulation of systems consisting of several motor-pump sets operating in parallel, sharing the same PV generator and the same hydraulic system, this thesis advances the state of the art from the simulation of a single pump to the possibility of simulating sets of two groups of pumps, each group consisting of a certain number of pumps of the same model operating at fixed or variable frequency. This configuration represents a large number of existing high power pumping systems, typically consisting of either a number of identical pumps in parallel operating at variable frequency, or one group of higher power pumps operating at variable frequency (or fixed frequency with soft starters to save on frequency converters) and a second group of lower power pumps operating at variable frequency. This work now makes it possible to estimate the productivity (typically the annual volume of water or during the irrigation period) of systems that meet these constraints. It has been possible to verify how the use of several pumps sharing a PV generator and the hydraulic system improves the productivity calculated for these pumps independently, using independent PV generators that add up to the same power. This intuition was already present in the PV pump sector, since the PV generator should be able to supply energy so that some or some of the pumps can operate at certain times (first and last hours of sunlight, cloudy days, ...) when there is not enough energy for all the pumps to operate, even at their lowest consumption operating point. However, as the state of the art only admitted the possibility of simulating a single pump, in the PV pumping sector the productivity of the pump group was historically deduced from the

simulation of a single pump connected to an independent PV generator of proportional power. The simulation of the pump group with the model proposed in this thesis has allowed us to detect a frequent error in the PV pumping sector when making this deduction: simulating this independent pump, proportionally reducing its PV generator, but maintaining the existing hydraulic system (which was designed for the whole pump group instead of a single pump). This produces an erroneously optimistic productivity estimate for that stand-alone pump (as there is less friction in the hydraulics).

In relation to the fourth main objective of this thesis, the use of the simulation tool SISIFO has been made publicly available. Code translations of the engine developed in MatLab© to other programming languages are avoided. Thus, the engine makes use of the matrix and vector calculation capabilities and efficiency of MatLab©. In addition, the engine is encapsulated in a microservice with a contract that defines its parameters and results.

This microservice is used from several sources. One of them is the web interface accessible at https://sisifo.info, developed in C# on the ASP.NET platform, which allows, in a more intuitive and simple way than the software used in this thesis, to provide the simulation parameters (or obtain others such as meteorological data, pump parameters,... from other online databases), to request the simulation to the engine, and to graphically display certain results, including some intermediate results that may be useful in teaching or research environments.

A second form of access to the engine, currently restricted to other researchers on request, is direct access to the simulation microservice. This allows other client software to request simulations directly from the microservice, facilitating, for example, the execution of multiple simulations by varying some of the parameters (e.g. selecting the best PV module model at one site or a similar system at several sites). The reason for the restricted access is that handling such requests, which can be massive, requires a large amount of computation over a long period of time. Furthermore, these microservices are implemented in such a way as to allow parallelisation of the execution of the SISIFO engine, i.e. multiple concurrent simulations are possible (otherwise, as it is a MatLab© engine, only one instance per server would be viable, unless the *MatLab Server* product is purchased, which provides similar functionality, but its high cost licence is not available

in our organisation's campus licence). Of course, the concurrent programming aspects of running the engine in parallel have been solved.

Finally, it should be noted that, as has been seen in the previous chapters, the work carried out in this thesis combines both telematic and computer aspects (related to the simulation software itself) and photovoltaic aspects, especially those related to the behavioural models included in the simulation software.) The prior knowledge required to deal with the telematics and computing part comes from the previous training of the author, who is trained in the fields of electronics and telematics, and is a teacher and researcher in the field of telematics engineering. However, the photovoltaic knowledge required to initiate and carry out the work that will lead to the achievement of the objectives has been fully acquired throughout this thesis, which has been an interesting challenge for which I can only thank, above all, Dr Eduardo Lorenzo, Dr Luis Narvarte and Dr Rita Hogan for the opportunity to undertake it and for their immense patience during the enormous transfer of knowledge that they were kind enough to carry out, as well as my fellow researchers in the Photovoltaic Systems Research Group and in the spin-off Qualifying Photovoltaics. Learning new knowledge, in this case interdisciplinary, and satisfying our curiosity is a privilege and has been an enjoyable task.

6.2 Future work

Most of the contributions in this thesis, while providing answers to the questions posed as objectives, by their very nature open the door to many other additional questions that remain as suggestions for future work. Some of these questions are already being addressed within the research group.

This section briefly lists some of them, without attempting to rank them in terms of relevance or importance, but only as outlines of a number of avenues that might be more or less interesting to pursue, and to what end.

With respect to the simulation of bifacial systems:

- To extend the analysis of the effect of non-uniformity in bifacial modules. Especially with regard to its translation to the overall production of the generator, which is still an open question.

- Compare the effect of using segment-to-point versus segment-to-segment view factors to obtain irradiance. The module, due to its construction characteristics (cells in series), does not allow some cells to generate more current than others despite receiving a higher irradiance, so a priori it does not seem appropriate to use segment-to-segment view factors. How this translates into electrical power requires further analysis.

  A first step in this direction, in which I have been involved during the last few months of this thesis, is an analysis (Santamaría & Ledesma, 2023) comparing segment-to-segment and segment-to-point 2D view factor calculations. It shows that the process of averaging the outcomes derived from applying the segment-to-point method over three strategically placed points at the centre and the edges of the PV module results in a non-significant discrepancy with the outcome of the segment-to-segment method.
- Analyse reality and compare it with simulation results. The aim is to improve and validate the models. Some of the PV plants whose expected productivity we have modelled using the work of this thesis have already been completed and connected to the grid, so it would be very interesting to have the opportunity to carry out experimental campaigns on the same or other plants in the same case.

Regarding simulation on sloping terrain:

- To allow the simulation on sloping terrain to be used to model the real angle that we have found some tracker manufacturers include to prevent the roughness of the terrain from causing shadows on the trackers. The aim is to avoid using tracking angles for perfectly horizontal terrain when real trackers do not use them, so that the expectation better matches reality.
- Extend the model to uneven terrain with curvature, such as that found on hilltops or at the bottom of valleys. This would probably require calculating the tracking angles to find the best option among the many available, or applying some deep learning as there is no single solution.
- Analyse the reality and compare it with the simulation results. The aim is to improve and validate the models. In this sense, some of the PV plants whose expected productivity we have modelled using the work of this thesis are already

under construction, so it would be very interesting to have the opportunity to carry out experimental campaigns on them.

Concerning multi-pump irrigation systems:

- Incorporate the existence of tolerances in the pump specifications into the model. Some manufacturers provide the expected tolerance in the characteristic curves of the pumps they manufacture. It would be very interesting to consider to what extent this tolerance influences the final expected productivity.
- Investigate the design of multi-pump systems. With the initial state of the art, where it was possible to simulate a single pump separately, in the first journal article published as part of this thesis (Almeida, Ledesma, et al., 2018) it was possible to establish some general criteria that allow the most suitable pump to be selected, when powered by a PV generator, from a set of available pumps. By extending the simulation possibility to multi-pump systems, it is possible to investigate which pump models in one group could be best combined with other pumps in the second group. Defining "better" in the desired sense, such as higher productivity in terms of annual pumped water volume, or less downtime. This aspect that could contribute to a better design of newly developed PV pumping systems is an open question.
- Analyse the reality and compare it with the simulation results. The aim is to improve and validate the models.

Concerning the SISIFO simulation software itself:

- To make visible in the SISIFO web interface other simulation possibilities that the engine allows, resulting in many cases from previous theses, such as hybridisation in the generator part (diesel,...) or in the pump part, as groups of pumps powered by PV generator, others by generators with other energy sources (diesel, grid connection) sharing the hydraulic system. The aim is to enable the simulation of hybrid systems. These systems are common, for example, when the generator is migrated from pumping systems previously connected to the grid or diesel to PV generators, as a partial migration is often undertaken (either to convince irrigators of the benefits of PV systems, or for economic reasons, etc.).

- To allow the simulation of not only a representative case (PV generator set, inverter, transformers) in the web interface. The engine, following the work of this thesis, already allows to combine different types of generators, with different module models, structure types, etc., to connect different generators to each inverter, to use several inverter models, etc. The representative case worked sufficiently well until recently, as PV plants used the same model of module, inverter, transformer, etc. However, today many large PV systems are designed with two module models, strings with different module quantities, two or more inverter models, so it is important to cover this. This is even more important on a sloping site, as the generators in each orientation will deliver an amount of energy that can be very different at any given time.
- Decompose the current monolithic engine and propose it as a serverless architecture. This architecture allows each functionality to be programmed in a different programming language and executed independently (even on separate systems, outside the programmer's control). The aim is twofold:
    - To make it easy for teachers or researchers to contribute to the development of the simulation tool by contributing or improving existing models, focusing only on the specific functionality to be improved, without having to know the rest of the tool in detail. This allows the teacher or researcher to choose which features to focus on, to use their preferred programming language, and to run the simulation with the new functionality they provide.
    - Improve the parallelization and scalability of the system. As a feature, a serverless architecture takes full care of the choice of platform that executes each function, the number of instances that grow or shrink according to demand, and similar situations.

  This feature will be a good starting point for revising the software internally and making it open source. There is a similar initiative (Stein et al., 2016) in the state of the art, but it requires the use of a specific programming language and does not allow execution, but only works as a publicly available code library.
- Regarding the web interface, currently using C# and ASP.NET on the server side (back-end) and HTML/CSS/JavaScript on the client side (front-end), it will be

migrated to the new Blazor paradigm. This will allow the use of C#/Blazor in both front-end and back-end, improving user interaction and certain response times.

In relation to other aspects of photovoltaics:

- Improve the fit of spectral losses to reality. This includes both incorporating more advanced spectral models that have recently appeared in the state of the art, as well as proposing a new spectral model. Spectral loss (or gain) is significant in certain locations and is not considered, for example, in widely used software such as PVsyst© where it is not considered by default. In this sense, we at IES-UPM have already started some experiments in PV plants in Chile to obtain data to improve existing models or to propose new ones.
- Incorporate an axis tracking model that does not completely avoid inter-row shading during back-tracking, but partially allows for it. This partial shading allowance may vary depending on whether the module configuration in the generator is horizontal or vertical. If the module is horizontal, partial shading of up to 1/3 (or 2/3) of the module can be allowed, leaving one (or two) of the diodes in conduction. If the module is mounted vertically and is of the "half-cell" type, partial shading of ½ of the module can be tolerated. In certain cases, it may be possible to compensate for the losses due to shading by better matching the tracker angle to the ideal. Something similar was suggested in (Lorenzo & Macagnan, 1994).
- As an extension to the previous section, allow the simulation of "hot-spot-free" type modules, where the loss due to shading is proportional to the geometric shading and therefore does not behave like traditional modules, which disable entire thirds of the module when the protection diodes enter conduction to prevent the module from operating in the second quadrant of the I-V curve.
- Incorporate additional state-of-the-art models of cell temperature behaviour.
- Include the ability to simulate generators in buildings (BIPV) or floating on water. These are new trends with their own specific characteristics.

In relation to other non-photovoltaic aspects of large PV plants:

- Refine the inverter model in at least two ways: a) include the effect of reactive power (it affects clipping and efficiency) and b) allow the use of efficiency curves as a function of inverter output voltage and temperature.
- Allow the simulation of battery systems, both isolated and connected to the grid. In this sense, in this thesis, I have included in the simulation software the possibility of simulating a PV system configuration with battery storage (CATL cubes) during sunshine hours, where the inverters draw their energy either from the PV generator or from the batteries, but never simultaneously), typically to use the batteries to produce electrical energy after sunset. But there is still a lot of work to be done.

Chapter 7

DISSEMINATION

7.1 International peer-reviewed journals

(a) Almeida, R. H., **Ledesma, J.R.**, Barata, I. A., Narvarte, L., Ferrara, G., & Antipodi, L. (2018). A new pump selection method for large-power PV irrigation systems at a variable frequency. *Energy Conversion and Management*, 174, 874–885. https://doi.org/10.1016/j.enconman.2018.08.071.

(b) **Ledesma, J. R.**, Almeida, R. H., Martínez-Moreno, F., Rossa, C., Martín-Rueda, J., Narvarte, L., & Lorenzo, E. (2020). A simulation model of the irradiation and energy yield of large bifacial photovoltaic plants. *Solar Energy*, 206, 522–538. https://doi.org/10.1016/j.solener.2020.05.108.

(c) **Ledesma, J. R.**, Almeida, R.H., & Narvarte. L. (2022). Modeling and Simulation of Multipumping Photovoltaic Irrigation Systems. *Sustainability* 14, no. 15. https://doi.org/10.3390/su14159318.

(d) Theristis, M., Riedel-Lyngskær, N., Stein, J. S., Deville, L., Micheli, L., Driesse, A., Hobbs, W. B., Ovaitt, S., Daxini, R., Barrie, D., Campanelli, M., Hodges, H., **Ledesma, J. R.**, Lokhat, I., McCormick, B., Meng, B., Miller, B., Motta, R., Noirault, E., ... Zhao, C. (2023). Blind photovoltaic modeling intercomparison: A multidimensional data analysis and lessons learned. *Progress in Photovoltaics: Research and Applications*, 31(11), 1144–1157. https://doi.org/10.1002/pip.3729.

(e) **J.R. Ledesma**, Lorenzo E., y Narvarte L. Single-axis tracking and bifacial gain on sloping terrain. (Submitted to *Progress in Photovoltaics: Research and Applications* in March 2023; under review at the time of writing).

7.2 Conference papers

(a) Martínez-Moreno, F., Rossa, C., **Ledesma, J. R.**, & Merodio, P. (2020). Aspectos de la no uniformidad de la irradiancia trasera en generadores fotovoltaicos bifaciales. In H. Gonçalves & M. Romero (Eds.), *CIES2020: As Energias Renováveis na Transição Energética: Livro de Comunicações do XVII Congresso Ibérico e XIII Congresso Ibero-americano de Energia Solar* (pp. 271–279). LNEG. https://doi.org/10.34637/cies20201.2030.

(b) Almeida, R. H., Belouaret, J., **Ledesma, J. R.**, & Narvarte, L. (2020). Simulación de sistemas de riego hibridos FV-RED: aplicación a riego directo. In H. Gonçalves & M. Romero (Eds.), *CIES2020: As Energias Renováveis na Transição Energética: Livro de Comunicações do XVII Congresso Ibérico e XIII Congresso Ibero-americano de Energia Solar* (pp. 1203–1209). LNEG - Laboratório Nacional de Energia e Geologia. https://doi.org/10.34637/cies2020.2.3142.

(c) **Ledesma, J. R.**, Almeida, R. H., & Narvarte, L. (2021). Modeling and Simulation of Multipump Photovoltaic Irrigation Systems. *38th European Photovoltaic Solar Energy Conference*, 1579–1582. https://doi.org/10.4229/EUPVSEC20212021-6CV.4.37.

(d) Theristis, M., Riedel-Lyngskær, N., Stein, J. S., Deville, L., Micheli, L., Driesse, A., Hobbs, W. B., Ovaitt, S., Daxini, R., Barrie, D., Campanelli, M., Hodges, H., Ledesma, J. R., Lokhat, I., McCormick, B., Meng, B., Miller, B., Motta, R., Noirault, E., … Zhao, C. (2022). *International Photovoltaic Modeling Intercomparison. 8th World Conference on Photovoltaic Energy Conversion (WCPEC-8)*, 1. https://doi.org/10.2172/2004810.

(e) Santamaría, J., & **Ledesma, J. R.** (2023). Evaluating 2D View-Factor Solutions to Estimate Ground-Reflected Irradiance in Large Bifacial PV Plants. *40th European Photovoltaic Solar Energy Conference and Exhibition*, 020462-001-020462–007. https://doi.org/10.4229/EUPVSEC2023/4DV.4.30.

7.3 Technology transfer

(a) Workshop. *Simulación avanzada de sistemas de bombeo fotovoltaico.* 16/Jan/2019. Instituto de Energía Solar, Madrid.

Technical workshop to disseminate research results on PVIS. It disseminated the new pump selection method published in the corresponding journal article, A new pump selection method for large-power PV irrigation systems at variable frequency, using the on-line SISIFO simulation software tool as presented in chapter 5. Organised in the framework of the European project MASLOWATEN. Limited to 30 industrial participants.

(b) Workshop. *Estimación y certificación de la producción energética en centrales fotovoltaicas con módulos bifaciales.* 24/Apr/2019. Instituto de Energía Solar, Madrid.

Technical workshop to disseminate research results on modelling and estimation of bifacial gain. Based on the model presented in Chapter A SIMULATION MODEL OF THE IRRADIATION AND ENERGY YIELD OF LARGE BIFACIAL PV PLANTS ON FLAT TERRAIN2. Organized in the framework of the European project MASLOWATEN. More than 150 participants from academia and industry.

(c) Workshop. *Simulación avanzada de sistemas de bombeo fotovoltaico constituidos por varias bombas en paralelo*. 28/Oct/2021. Instituto de Energía Solar, Madrid.

Technical workshop to disseminate research results on multi-pump PVIS. It disseminated the new model and the multi-pump simulation capability presented in chapter 4, using the online simulation software tool SISIFO, as presented in

chapter 5. Organised in the framework of the European MASLOWATEN project. Limited to 20 industrial participants. Several editions.

Annex A

We have been preparing 'reference' monofacial modules for measuring both G and T_C simultaneously for many years (Martínez-Moreno et al., 2011). For that, a part of the module is short-circuited for measuring I_{SC} keeping the other part in open circuit for measuring V_{OC}. Now, we have extended this practice making a bifacial reference module to measure operational conditions, G_{FRONT}, G_{REAR} and T_C. Accordingly, the module is electrically divided into three parts (this is easily done by accessing the junction boxes) as Figure A.1 shows. The upper and lower parts are short-circuited through calibrated resistances. A black vinyl sheet has been directly glued onto the front (rear) side and, then, protected with a white vinyl sheet. The black vinyl minimizes/reduces internal reflection and so it can be neglected/despised, helping to make linear the relation between G and I_{SC}. The high reflectance of the white vinyl should help making the temperature increment of each part with respect to the ambient temperature related just to the irradiance incident on that part.

This way, the corresponding short-circuit current, $I_{SC,REAR}$ ($I_{SC,FRONT}$), becomes sensitive to only $G_{BACK}(G_{FRONT})$. The central part is left in open-circuit. A first approximation is obtained when neglecting the effect of temperature on short-circuit current. Then:

$$G_{FRONT(1A)} = I_{SC,FRONT} \cdot \frac{G^*}{I^*_{SC,Front}} \tag{A.1}$$

$$G_{REAR(1A)} = I_{SC,REAR} \cdot \frac{G^*}{I^*_{SC,REAR}} \tag{A.2}$$

$$T_{C,VOC} = T_C^* + \frac{1}{\beta_T} \cdot \left[\frac{V_{OC}}{V_{OC}^*} - 1 - a \cdot ln \frac{G_{FRONT(1A)} + G_{REAR(1A)}}{G^*}\right] \tag{A.3}$$

Where β_T is the thermal coefficient of V_{OC} and a is the ratio of the thermal voltage to the open circuit voltage ($a = 0.05$ is a reasonable approximation for crystalline silicon modules). A further refinement is achieved by estimating the operating temperature of the upper and lower parts. The assumption that the temperature increment with respect to the ambient temperature is linearly related with corresponding irradiance leads to:

$$T_{\mathrm{C,FRONT}} = T_{\mathrm{C,VOC}} - C_{\mathrm{T}}.G_{\mathrm{REAR(1A)}} \quad (A.4)$$

$$T_{\mathrm{C,REAR}} = T_{\mathrm{C,VOC}} - C_{\mathrm{T}}G_{\mathrm{FRONT(1A)}} \quad (A.5)$$

where C_T keeps the meaning and value given in Equation (23). Then, a temperature correction is applied to the first approximation G values are corrected in temperature:

$$G_{\mathrm{FRONT}} = G_{\mathrm{FRONT(1A)}}/[1 + \alpha_T(T_{\mathrm{C,FRONT}} - T_{\mathrm{C}}^*)] \quad (A.6)$$

$$G_{\mathrm{REAR}} = G_{\mathrm{REAR(1A)}}/[1 + \alpha_T(T_{\mathrm{C,REAR}} - T_{\mathrm{C}}^*)] \quad (A.7)$$

where α_T is the thermal coefficients of I_{SC}. It must be noted that because α_T is low (usually below 0.07%/ºC) the correction of G_{1A} to G is also low, typically less than 2% and 1% for G_{FRONT} and G_{REAR}, respectively.

Finally, in case the PV plant is delivering power, a correction must be made to consider the fact that the reference module is slightly hotter. Then

$$T_{\mathrm{C,MPP}} = T_{\mathrm{C,VOC}} - C_{\mathrm{T}} \cdot G_{\mathrm{FRONT}} \cdot \eta_{\mathrm{FRONT}}^* \cdot [1 + \gamma \cdot (T_{\mathrm{C,VOC}} - T_{\mathrm{C}}^*)] \cdot (1 + \varphi_P \cdot GBR) \quad (A.8)$$

where η_{FRONT}^* is the efficiency of the frontal side of the PV module and GBR is the Irradiance bifacial ratio defined in Equation (21).

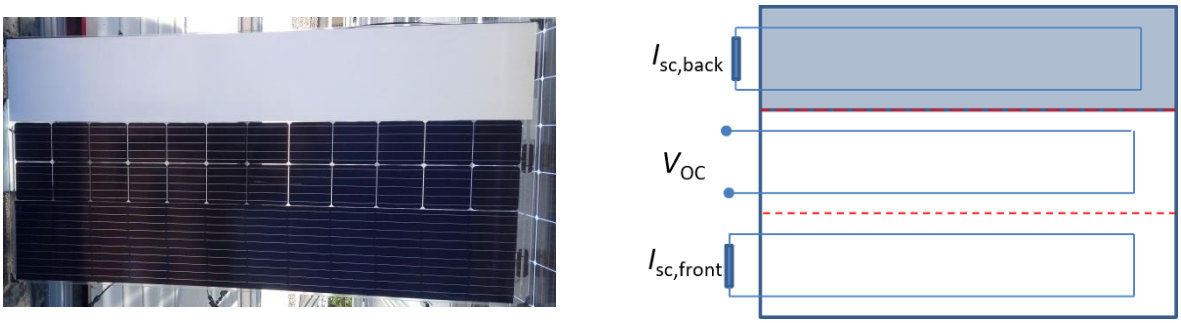


Figure A.1. Bifacial reference module (a) View of the frontal side (b) Electrical scheme

This set of equations implies assuming, first, that heat transfer between the three parts of the module is negligible. That allows assuming the temperature of the middle (uncovered) part is equal to the temperature of a normal module. Besides, it implies that the optical properties of the exposed side of the upper and lower parts are not affected by the black vinyl sheet covering the non- exposed side. That obviously depends on the transparency (spaced cells) of the modules, which is typically very low. For example, the

TRINA DUOMAX TWIN TSM PV modules are composed by square cells (156 mm, side-spaced 4mm). Hence, transparency is about 5%. Corresponding $T_{C,REAR}$ increase with respect to Equation (A.5) due to the black vinyl can be estimated at a maximum of 1.5ºC (for G_{REAR}as high as G^*), which translate in G_{REAR} errors below 0.1%. Finally, it also implies that the two-vinyl sheets do not alter heat dissipation of the covered parts, i.e. that the thermal isolation provided by the sheets is negligible. These two last suppositions allow us to postulate Equation (A.4) and Equation (A.5). Perhaps they are not true, and these parts are in fact slightly hotter than if they were uncovered. However, because α_T is very low, the impact on corrections from G_{1A} to G must also be negligible.

On the other hand, the vertical non-uniformity of rear irradiance also deserves further comment. For that, the experimental set-up described in Section 2.4 includes a reference cell (ATERSA Compensated Calibrated Cell) close to the reference module and in the same horizontal coordinate as the module part measuring G_{REAR}, as Figure A.2-a shows. The measurements of this cell are compensated in temperature. Both reference module and cell are calibrated in the IES-UPM against the same secondary device (Carrillo et al., 2017). Figure A.2-b compares the simultaneous measurements of both devices from 5th October to 18th November. The difference is 1%, which is below the measurement uncertainty. Experiments with the module in vertical instead of landscape position are planned for future work.

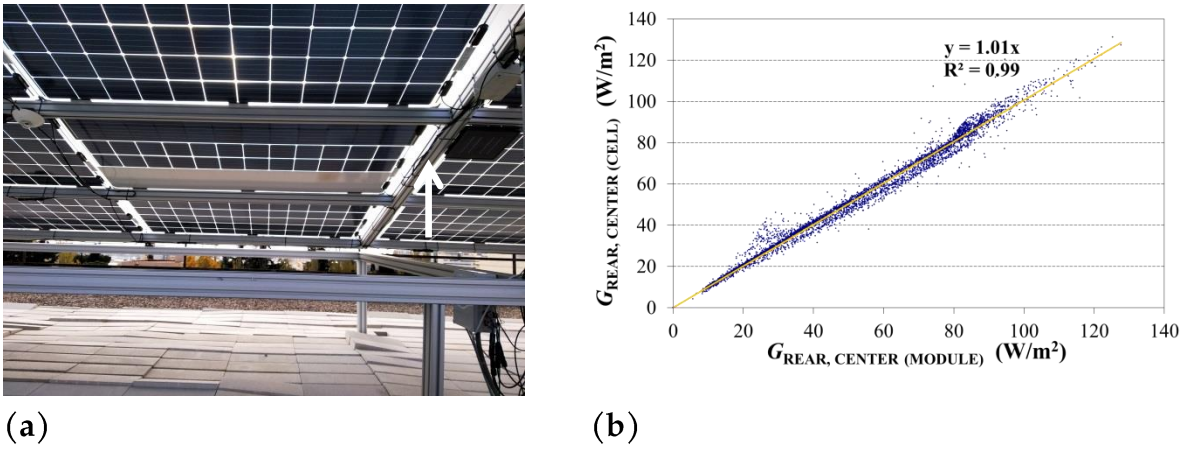


Figure A.2. (a) Bifacial reference module (rear view) and calibrated reference cell to measure G_{REAR} (b) Comparison between the G_{REAR} measured by both devices

References

Adobe Experience Cloud. (n.d.). *A guide to traditional vs. Single-page apps (SPAs)*. A Guide to Traditional vs. Single-Page Apps (SPAs). Retrieved October 19, 2023, from https://business.adobe.com/blog/basics/differences-between-traditional-web-apps-and-single-page-apps

Aguiar, R., & Collares-Pereira, M. (1992). TAG: a time-dependent, autoregressive, Gaussian model for generating synthetic hourly radiation. *Solar Energy*, *49*(3), 167–174. https://doi.org/10.1016/0038-092X(92)90068-L

Almeida, R. H., Carrêlo, I. B., Lorenzo, E., Narvarte, L., Fernández-Ramos, J., Martínez-Moreno, F., & Carrasco, L. M. (2018). Development and Test of Solutions to Enlarge the Power of PV Irrigation and Application to a 140 kW PV-Diesel Representative Case. *Energies*, *11*(12), 3538. https://doi.org/10.3390/en11123538

Almeida, R. H., Ledesma, J. R., Barata, I. A., Narvarte, L., Ferrara, G., & Antipodi, L. (2018). A new pump selection method for large-power PV irrigation systems at a variable frequency. *Energy Conversion and Management*, *174*, 874–885. https://doi.org/10.1016/j.enconman.2018.08.071

Almeida, R. H., Narvarte, L., & Lorenzo, E. (2018). PV arrays with delta structures for constant irradiance daily profiles. *Solar Energy*, *171*, 23–30. https://doi.org/10.1016/j.solener.2018.06.066

Alonso-Abella, M., Lorenzo, E., & Chenlo, F. (2003). PV water pumping systems based on standard frequency converters. *Progress in Photovoltaics: Research and Applications*, *11*(3), 179–191. https://doi.org/10.1002/pip.475

Anderson, K., & Mikofski, M. (2020). *Slope-Aware Backtracking for Single-Axis Trackers Slope-Aware Backtracking for Single-Axis Trackers* (NREL/TP-5K00-76626). National Renewable Energy Laboratory. https://doi.org/10.2172/1660126

Asgharzadeh, A., Lubenow, T., Sink, J., Marion, B., Deline, C., Hansen, C., Stein, J., & Toor, F. (2017, June). *Analysis of the Impact of Installation Parameters and System Size on Bifacial Gain and Energy Yield of PV Systems*. 2017 IEEE 44th Photovoltaic Specialist Conference (PVSC). https://doi.org/10.1109/pvsc.2017.8366690

Ayala, P., Munoz, C., Osorio, N., Hernandez, C., Zurita, F., Gutierrez, V., Ramirez, G., Mancilla, F., Valdivia, P., Cuevas, F., & Ferrada, P. (2018, June). *Bifacial Technology Performance Compared With Three Commercial Monofacial PV Technologies under Outdoor High Irradiance Conditions at the Atacama Desert*. 2018 IEEE 7th World Conference on Photovoltaic Energy Conversion (WCPEC) (A Joint Conference of 45th IEEE PVSC, 28th PVSEC & 34th EU PVSEC). https://doi.org/10.1109/pvsc.2018.8547345

Bailey, R., & Jaubert, J. (2018). A simplified method to approximate bifacial system mismatch losses. *5th Bifi PV Workshop, Denver, Colorado*. http://npv-workshop.com/fileadmin/images/bifi/denver/presentations/5__Bailey-_simplified_method_to_approximate_mismatch_losses_bifiPV2018.pdf

Bakelli, Y., Hadj Arab, A., & Azoui, B. (2011). Optimal sizing of photovoltaic pumping system with water tank storage using LPSP concept. *Solar Energy*, *85*(2), 288–294. https://doi.org/10.1016/j.solener.2010.11.023

Barlow, R., McNelis, B., & Derrick, A. (1993). *Solar pumping: An introduction and update on the technology, performance, costs, and economics* (NASA STI/Recon Technical Report N Volume:93;

p. 23444). NASA STI/Recon Technical Report N Publication NASA STI/Recon Technical Report N Volume: 93. https://doi.org/10.3362/9781780445984.002

Bellman, R. E. (1957). *Dynamic Programming*. Princeton University Press.

Bonilla-Castro, J., Herz, M., Monokroussos, C., & Schweiger, M. (2018). Energy Yield Comparison between Bifacial and Monofacial PV Modules: Real World Measurements and Validation with Bifacial Simulations. *35th EUPVSEC, Brussels*.

Bouzidi, B. (2013). New sizing method of PV water pumping systems. *Sustainable Energy Technologies and Assessments*, *4*, 1–10. https://doi.org/10.1016/j.seta.2013.08.004

Brennan, M. P., Abramase, A. L., Andrews, R. W., & Pearce, J. M. (2014). Effects of spectral albedo on solar photovoltaic devices. *Solar Energy Materials and Solar Cells*, *124*, 6. https://doi.org/10.1016/j.solmat.2014.01.046

Buß, D., Herzog, E., Scholz, C., Zimmermann, R., & Eisenhawer, B. (2018, September). *Outdoor characterization of bifacial modules at Hanwha Q Cells*. BifiPV Workshop 2018, Denver, CO. http://npv-workshop.com/fileadmin/images/bifi/denver/presentations/4__Buss-_outdoor_module_characterisation_bifiPV2018.pdf

Campana, P. E., Li, H., & Yan, J. (2013). Dynamic modelling of a PV pumping system with special consideration on water demand. *Applied Energy*, *112*, 635–645. https://doi.org/10.1016/j.apenergy.2012.12.073

Carrêlo, I. B., Almeida, R. H., Narvarte, L., Martinez-Moreno, F., & Carrasco, L. M. (2020). Comparative analysis of the economic feasibility of five large-power photovoltaic irrigation systems in the Mediterranean region. *Renewable Energy*, *145*, 2671–2682. https://doi.org/10.1016/j.renene.2019.08.030

Carrillo, J. M., Martínez-Moreno, F., Lorenzo, C., & Lorenzo, E. (2017). Uncertainties on the outdoor characterization of PV modules and the calibration of reference modules. *Solar Energy*, *155*, 880–892. https://doi.org/10.1016/j.solener.2017.07.028

Carrillo, J. M., Muñoz, J., Makibar, A., Luna, A., & Narvarte, L. (2015). SISIFO: The open-source simulation tool of PV systems developed in PVCROPS. *EU PVSEC Proceedings*, 2190–2192. https://oa.upm.es/41959/

Catena, M., Cascone, I., & Carbone, M. (2018). Performance estimation of bifacial PV modules: A simulation approach through both physical and semi-empirical math models and its validation using real bifacial plant data. *PVSEC 2017*. PVSEC, Amsterdam.

Chudinzow, D., Haas, J., Díaz-Ferrán, G., Moreno-Leiva, S., & Eltrop, L. (2019). Simulating the energy yield of a bifacial photovoltaic power plant. *Solar Energy*, *183*, 812–822. https://doi.org/10.1016/j.solener.2019.03.071

Chunduri, S., & Schmela, M. (2017). *Bifacial Solar Module Technology—2017 Edition*. TaiyangNews. https://taiyangnews.info/taiyangnews-bifacial-solar-report-2017/

COMPASS. (n.d.). Retrieved November 4, 2021, from https://www.lorentz.de/en/products/submersible-solar-pumps.html

Cuevas, A. (2005). The early history of bifacial solar cells. *20th European Photovoltaic Solar Energy Conference (EU PVSEC)*, 801–805.

da Costa Bortoni, E., de Almeida, R. A., & Viana, A. N. C. (2008). Optimization of parallel variable-speed-driven centrifugal pumps operation. *Energy Efficiency*, *1*(3), 167–173. https://doi.org/10.1007/s12053-008-9010-1

de la Parra, I., Muñoz, M., Lorenzo, E., García, M., Marcos, J., & Martínez-Moreno, F. (2017). PV performance modelling: A review in the light of quality assurance for large PV plants. *Renewable and Sustainable Energy Reviews*, *78*, 780–797.

https://oa.upm.es/49950/1/INVE_MEM_2017_271037.pdf. https://doi.org/10.1016/j.rser.2017.04.080

Deline, C., MacAlpine, S., Marion, B., Toor, F., Asgharzadeh, A., & Stein, J. (2016). Evaluation and Field Assesment of Bifacial Photovoltaic Module Power Rating Methodologies. *2016 IEEE 43rd Photovoltaic Specialists Conference (PVSC)*, 3698–3703.

Deline, C., Marion, B., MacAlpine, S., Stein, J., Toor, F., & Ayala, S. (2017, October 26). *Bifacial PV Performance Models: Comparison and Field Results*. BiFiPV 2017 Workshop, Konstanz, Germany. https://www.nrel.gov/docs/fy20osti/70463.pdf

Djoudi Gherbi, A., Hadj Arab, A., & Salhi, H. (2017). Improvement and validation of PV motor-pump model for PV pumping system performance analysis. *Solar Energy*, *144*, 310–320. https://doi.org/10.1016/j.solener.2016.12.042

Egido, M., & Lorenzo, E. (1986). Bifacial Photovoltaic Panels with Sun Tracking. *International Journal of Solar Energy*, *4*(2), 97–107. https://doi.org/10.1080/01425918608909842

EIP Water. (2012). *European Innovation Partnership Water—Strategic Implementation Plan*. European Commission. https://single-market-economy.ec.europa.eu/sectors/raw-materials/eip/strategic-implementation-plan-sip_en

Enochian, R. V. (1982). *Solar- and Wind-Powered Irrigation Systems* (307914; Agricultural Economic Reports). United States Department of Agriculture, Economic Research Service. https://doi.org/10.22004/ag.econ.307914

Estrada, C., González, C., Aliod, R., & Paño, J. (2009). Improved Pressurized Pipe Network Hydraulic Solver for Applications in Irrigation Systems. *Journal of Irrigation and Drainage Engineering*, *135*(4), 421–430. https://doi.org/10.1061/(asce)ir.1943-4774.0000100

European Commission, CORDIS. (2012). *PhotoVoltaic Cost r€duction, Reliability, Operational performance, Prediction and Simulation*. https://cordis.europa.eu/project/id/308468

European Commission, CORDIS. (2015). *MArket uptake of an innovative irrigation Solution based on LOW WATer-ENergy consumption*. https://cordis.europa.eu/project/id/640771

FAO. (n.d.). *CropWat | Land & Water | Food and Agriculture Organization of the United Nations*. Retrieved November 4, 2021, from https://www.fao.org/land-water/databases-and-software/cropwat/en/

Fedrizzi, M. C., & Sauer, I. L. (2002). Bombeamento Solar Fotovoltaico, histórico, características e projetos. *Encontro de Energia no Meio Rural*, *4*. http://www.proceedings.scielo.br/scielo.php?script=sci_arttext&pid=MSC0000000022002000100034&lng=en&nrm=iso

Fernández-Ramos, J., Narvarte, L., Almeida, R. H. T., Carrêlo, I. B., Moreno, L. M. C., & Lorenzo, E. (2018). *Method and Control Device for Photovoltaic Pumping Systems* (Patent WO 2018/134453 A1).

Fowler, M. (2014, March 25). *Microservices*. Martinfowler.Com. https://martinfowler.com/articles/microservices.html

Franklin Electric. (n.d.). *SOLARPAK*. Retrieved November 4, 2021, from http://tools.franklin-electric.com/solar/

Gasque, M., González-Altozano, P., Gutiérrez-Colomer, R. P., & García-Marí, E. (2020). Optimisation of the distribution of power from a photovoltaic generator between two pumps working in parallel. *Solar Energy*, *198*, 324–334. https://doi.org/10.1016/j.solener.2020.01.013

GESTAR. (n.d.). Retrieved November 9, 2021, from http://www.acquanalyst.com/contenido.php?idioma=2&modulo=descargas&cat=2

Ghoneim, A. A. (2006). Design optimization of photovoltaic powered water pumping systems. *Energy Conversion and Management*, *47*(11–12), 1449–1463. https://doi.org/10.1016/j.enconman.2005.08.015

Gracia-Amillo, A., Lopez-Garcia, J., Kenny, R. P., & Sample, T. (2019). Energy yield analysis of bifacial PV modules: Different technologies and configurations. *Proc. 36th European PVSEC*, 1165–1170.

Grundfos. (n.d.). Retrieved November 4, 2021, from http://de.grundfos.com/grundfos-wincaps.html

Gueymard, C., Lara-Fanego, V., Sengupta, M., & Xie, Y. (2019). Surface and albedo reflectance: Review of definitions, angular and spectral effects, and intercomparison of major data sources in support of advanced solar irradiance modeling over the America. *Solar Energy*, *182*, 18. https://doi.org/10.1016/j.solener.2019.02.040

Halcrow, W. (1981). *Small-scale solar-powered irrigation pumping systems; technical and economic review*. UNDP (United Nations Development Program) Project GLO/78/004, executed by The World Bank. https://www.ircwash.org/sites/default/files/232.4-81SM-2.pdf

Hamidat, A., & Benyoucef, B. (2008). Mathematic models of photovoltaic motor-pump systems. *Renewable Energy*, *33*(5), 933–942. https://doi.org/10.1016/j.renene.2007.06.023

Hansen, C. W., Deline, C., MacAlpine, S., Marion, B., Asgharzadeh, A., Toor, F., & Stein, J. S. (2016). *Analysis of Irradiance Models for Bifacial PV Modules*. IEEE 43th PVSC, Portland.

Hay, J. E., & McKay, D. C. (1985). Estimating Solar Irradiance on Inclined Surfaces: A Review and Assessment of Methodologies. *International Journal of Solar Energy*, *3*(4–5), 203–240. https://doi.org/10.1080/01425918508914395

Herraiz, J. I., Fernández-Ramos, J., Almeida, R. H., Báguena, E. M., Castillo-Cagigal, M., & Narvarte, L. (2022). On the tuning and performance of Stand-Alone Large-Power PV irrigation systems. *Energy Conversion and Management: X*, *13*, 100175. https://doi.org/10.1016/j.ecmx.2021.100175

Hiroshi, M. (1966). *Radiation energy transducing device* (Patent US 3278811 A).

IEA-PVPS Task1. (2023). *Snapshot of Global PV Markets 2023* (IEA-PVPS T1-44:2023). International Energy Agency, Photovoltaic Power Systems Programme. https://iea-pvps.org/wp-content/uploads/2023/04/IEA_PVPS_Snapshot_2023.pdf

IEA-PVPS Task13. (2014a). *Analysis of Long-Term Performance of PV Systems—Different Data Resolution for Different Purposes* (IEA-PVPS T13-05:2014; Photovoltaics Power Systems Programme (PVPS)). International Energy Agency (IEA). https://iea-pvps.org/wp-content/uploads/2020/01/IEA-PVPS_T13-D2_3_Analytical_Monitoring_of_PV_Systems_Final.pdf

IEA-PVPS Task13. (2014b). *Analytical Monitoring of Grid-connected Photovoltaic Systems—Good Practices for Monitoring and Performance Analysis* (IEA-PVPS T13-03:2014; Photovoltaics Power Systems Programme (PVPS)). International Energy Agency (IEA). https://iea-pvps.org/wp-content/uploads/2020/01/IEA-PVPS_T13-D2_3_Analytical_Monitoring_of_PV_Systems_Final.pdf

IEA-PVPS Task13. (2017). *PV Performance Modelling Methods and Practices—Results from the 4th PV Performance Modeling Collaborative Workshop* (IEA-PVPS-T13-06:2017; p. 56). https://iea-pvps.org/wp-content/uploads/2020/01/T13_Report_PV_Performance_Modeling_Methods_and_Practices_FINAL_March_2017.pdf

Innovagri. (2016, May 25). *El riego solar, una alternativa para rentabilizar la energía*. https://www.innovagri.es/comunidad/el-riego-solar-una-alternativa-para-rentabilizar-la-energia.html

Iqbal, M. (1983). *An Introduction To Solar Radiation*. Academic Press. https://doi.org/10.1016/B978-0-12-373750-2.X5001-0

IRENA. (2023). *World Energy Transitions Outlook 2023: 1.5°C Pathway* (Vol. 1). International Renewable Energy Agency.

Kankiewicz, A. (2021, May 20). *PV plant performance challenges from near shading and complex terrain*. Solar Builder Magazine. https://solarbuildermag.com/news/pv-plant-performance-challenges-from-near-shading-and-complex-terrain/

Knecht, R., & Baumgartner, F. (2017, September 25). *PV-Battery and Diesel Hybrid System for Irrigation of a Farm in Patagonia*. 33rd EUPVSEC, Amsterdam.

Kopecek, R., & Libal, J. (2021). Bifacial Photovoltaics 2021: Status, Opportunities and Challenges. *Energies*, *14*(8). https://doi.org/10.3390/en14082076

Krenzinger, A., & Lorenzo, E. (1986). Estimation of Radiation Incident on Bifacial Albedo-Collecting Panels. *International Journal of Solar Energy*, *4*, 22.

kWh Analytics. (2021). *Solar Risk Assessment: 2021. Quantitative Insights from the Industry Experts*. https://www.kwhanalytics.com/solar-risk-assessment

Lamers, M. W. P. E., Özkalay, E., Gali, R. S. R., Janssen, G. J. M., Weeber, A. W., Romijn, I. G., & Van Aken, B. B. (2018). Temperature effects of bifacial modules: Hotter or cooler? *Solar Energy Materials and Solar Cells*, *185*, 192–197. https://doi.org/10.1016/j.solmat.2018.05.033

Lancho, F. (1989). *Aesthetic Considerations in a PV Project*. 9th PVSEC, Freiburg, Germany.

Langarita, R., Sánchez Chóliz, J., Sarasa, C., Duarte, R., & Jiménez, S. (2017). Electricity costs in irrigated agriculture: A case study for an irrigation scheme in Spain. *Renewable and Sustainable Energy Reviews*, *68*, 1008–1019. https://doi.org/10.1016/j.rser.2016.05.075

Larson, R. E., & Casti, J. L. (1978). *Principles of Dynamic Programming. Part I: Basic Analytic and Computational Methods*. Marcel Dekker Inc.

Ledesma, J. R., Almeida, R. H., Martinez-Moreno, F., Rossa, C., Martín-Rueda, J., Narvarte, L., & Lorenzo, E. (2020). A simulation model of the irradiation and energy yield of large bifacial photovoltaic plants. *Solar Energy*, *206*, 522–538. https://doi.org/10.1016/j.solener.2020.05.108

Ledesma, J. R., Almeida, R. H., & Narvarte, L. (2022). Modeling and Simulation of Multipumping Photovoltaic Irrigation Systems. *Sustainability*, *14*(15). https://doi.org/10.3390/su14159318

Leung, M., Mikofski, M. A., Hamer, M., Neubert, A., Parikh, A., Rainey, P., & Kharait, R. (2022). Tracker Terrain Loss Part Two. *IEEE Journal of Photovoltaics*, *12*(1), 127–132. https://doi.org/10.1109/JPHOTOV.2021.3114599

LG Electronics Inc. (2019). *Bifacial Design Guide*. https://www.lg.com/global/business/download/resources/solar/Bifacial_design_guide_Full_ver.pdf

Liang, T. S., Pravettoni, M., Deline, C., Stein, J. S., Kopecek, R., Singh, J. P., Luo, W., Wang, Y., Aberle, A. G., & Khoo, Y. S. (2019). A review of crystalline silicon bifacial photovoltaic performance characterisation and simulation. *Energy Environ. Sci.*, *12*(1), 116–148. https://doi.org/10.1039/C8EE02184H

Lo, C. K., Lim, Y. S., & Rahman, F. A. (2015). New integrated simulation tool for the optimum design of bifacial solar panel with reflectors on a specific site. *Renewable Energy*, *81*, 293–307. https://doi.org/10.1016/j.renene.2015.03.047

Lopez-Garcia, J., Casado, A., & Sample, T. (2019). Electrical performance of bifacial silicon PV modules under different indoor mounting configurations affecting the rear reflected irradiance. *Solar Energy*, *177*, 471–482. https://doi.org/10.1016/j.solener.2018.11.051

Lopez-Garcia, J., Pavanello, D., & Sample, T. (2018). Analysis of Temperature Coefficients of Bifacial Crystalline Silicon PV Modules. *IEEE Journal of Photovoltaics*, *8*(4), 960–968. https://doi.org/10.1109/jphotov.2018.2834625

Lorenzo, E. (2010). Energy Collected and Delivered by PV Modules. In A. Luque & S. Hegedus (Eds.), *Handbook of Photovoltaic Science and Engineering* (pp. 984–1042). https://doi.org/10.1002/9780470974704.ch22

Lorenzo, E. (2021). On the historical origins of bifacial PV modelling. *Solar Energy*, *218*, 587–595. https://doi.org/10.1016/j.solener.2021.03.006

Lorenzo, E., & Macagnan, M. H. (1994). Considerations in the design of a one-axis tracking photovoltaic system. *Progress in Photovoltaics: Research and Applications*, *2*(1), 45–55. https://doi.org/10.1002/pip.4670020107

Lorenzo, E., Montero, M., & Egido, M. A. (1988). Operational Results of a 8.1 kWp P.V. Installation in a Sub-Sahel Village in Senegal. *8th Photovoltaic Solar Energy Conference (PVSEC)*, 221–215.

Lorenzo, E., Narvarte, L., & Muñoz, J. (2011). Tracking and back-tracking. *Progress in Photovoltaics: Research and Applications*, *19*(6), 747–753. https://oa.upm.es/12154/2/INVE_MEM_2011_109654.pdf. https://doi.org/10.1002/pip.1085

Lorenzo, E., Pérez, M., Ezpeleta, A., & Acedo, J. (2002). Design of tracking photovoltaic systems with a single vertical axis. *Progress in Photovoltaics: Research and Applications*, *10*(8), 533–543. https://doi.org/10.1002/pip.442

Luque, A., Sala, G., Lorenzo, E., & Lopez-Romero, S. (1984). Diffusing reflectors for bifacial photovoltaic panels. *Solar Cells*, *13*, 15. https://doi.org/10.1016/0379-6787(85)90021-3

Macagnan, M. H., Lorenzo, E., & Jimenez, C. (1994). Solar Radiation in Madrid. *International Journal of Solar Energy*, *16*(1), 1–14. https://doi.org/10.1080/01425919408914262

Marion, B., MacAlpine, S., Deline, C., Asgharzadeh, A., Toor, F., Riley, D., Stein, J., & Hansen, C. (2017). A practical irradiance model for bifacial PV modules. *2017 IEEE 44th Photovoltaic Specialist Conference (PVSC)*, 1537–1542. https://www.nrel.gov/docs/fy17osti/67847.pdf

Martín, N., & Ruiz, J. M. (1999). A new method for the spectral characterisation of PV modules. *Progress in Photovoltaics: Research and Applications*, *7*(4), 299–310. https://doi.org/10.1002/(sici)1099-159x(199907/08)7:4<299::aid-pip260>3.0.co;2-0

Martin, N., & Ruiz, J. M. (2005). Annual Angular Reflection Losses in PV Modules. *Progress in Photovoltaics: Research and Applications*, *13*, 9. https://doi.org/10.1002/pip.585

Martínez-Moreno, F., Lorenzo, E., Muñoz, J., & Moretón, R. (2011). On the testing of large PV arrays. *Progress in Photovoltaics: Research and Applications*, *20*(1), 100–105. https://doi.org/10.1002/pip.1102

Martínez-Moreno, F., Muñoz, J., & Lorenzo, E. (2010). Experimental model to estimate shading losses on PV arrays. *Solar Energy Materials and Solar Cells*, *94*(12), 2298–2303. https://doi.org/10.1016/j.solmat.2010.07.029

MASLOWATEN. (n.d.). MASLOWATEN. Retrieved October 19, 2018, from https://maslowaten.eu/

Mayer, O., Baumeister, A., & Festl, T. (1995). Design, simulation and diagnosis of photovoltaic pumping systems with DASTPVPS. *Proceedings of the 13th European Photovoltaic Solar Energy Conference*, 1915–1917.

McAdams, W. H. (1954). *Heat transmission* (3rd ed.). McGraw-Hill.

Mermoud, A., & Wittmer, B. (2017, December). *New features and latest developments in PVsyst.* 9th PVPMC Workshop, Weihai, China. https://pvpmc.sandia.gov/app/uploads/sites/243/2022/10/09_Bruno-Wittmer_New-features-and-latest-developments-in-PVsyst.pdf

Microsoft. (n.d.). *Microservice architecture style—Azure Architecture Center*. Microservice Architecture Style. Retrieved October 19, 2023, from https://learn.microsoft.com/en-us/azure/architecture/guide/architecture-styles/microservices

Monís, J. I., López-Luque, R., Reca, J., & Martínez, J. (2020). Multistage Bounded Evolutionary Algorithm to Optimize the Design of Sustainable Photovoltaic (PV) Pumping Irrigation Systems with Storage. *Sustainability*, *12*(3), 1026. https://doi.org/10.3390/su12031026

Moretón, R. (2016). *Contributions to uncertainty reduction in the estimation of PV plants performance* [Thesis (Doctoral), https://doi.org/10.20868/UPM.thesis.39896, E.T.S.I. Telecomunicación, Universidad Politécnica de Madrid]. https://oa.upm.es/39896/

Moretón, R., Lorenzo, E., Pinto, A., Muñoz, J., & Narvarte, L. (2017). From broadband horizontal to effective in-plane irradiation: A review of modelling and derived uncertainty for PV yield prediction. *Renewable and Sustainable Energy Reviews*, *78*, 886–903. https://oa.upm.es/46271/1/INVE_MEM_2017_252039.pdf. https://doi.org/10.1016/j.rser.2017.05.020

Muhsen, D. H., Ghazali, A. B., & Khatib, T. (2016). Multiobjective differential evolution algorithm-based sizing of a standalone photovoltaic water pumping system. *Energy Conversion and Management*, *118*, 32–43. https://doi.org/10.1016/j.enconman.2016.03.074

Muhsen, D. H., Khatib, T., & Abdulabbas, T. E. (2018). Sizing of a standalone photovoltaic water pumping system using hybrid multi-criteria decision making methods. *Solar Energy*, *159*, 1003–1015. https://doi.org/10.1016/j.solener.2017.11.044

Muñoz, J., & Carrillo, J. M. (2015). Modeling and sizing of large PV-diesel hybrid systems without energy storage. In *31st European Photovoltaic Solar Energy Conference and Exhibition (EU PVSEC 2015)* (pp. 1–6). WIP - Renewable Energies. https://oa.upm.es/41958/

Munoz, J., Carrillo, J., Martínez-Moreno, F., Carrasco, L., & Narvarte, L. (2015, September). Modeling and simulation of large PV pumping systems. *Proceedings of the 31th European Photovoltaic Solar Energy Conference and Exhibition*.

Muñoz, J., Marroyo, L., Collares-Pereira, M., Tyutyuyndzhiev, N., Conlon, M., El Moussaoui, A., & Wilkin, B. (2013). An open-source simulation tool of grid-connected PV systems. *28th European PV Solar Energy Conference and Exhibition*, 1–2. https://oa.upm.es/25779/

Muñoz, J., & Perpiñan, O. (2016). A simple model for the prediction of yearly energy yields for grid-connected PV systems starting from monthly meteorological data. *Renewable Energy*, *97*, 680–688. https://doi.org/10.1016/j.renene.2016.06.023

Narvarte, L., & Lorenzo, E. (2008). Tracking and ground cover ratio. *Progress in Photovoltaics: Research and Applications*, *16*(8), 703–714. https://doi.org/10.1002/pip.847

Nascimento, B., Albuquerque, D., Lima, M., & Sousa, P. (2015). Backtracking Algorithm for Single-Axis Solar Trackers installed in a sloping field. *International Journal of Engineering Research and Applications*, *5*(12–4), 100–103. https://www.ijera.com/papers/Vol5_issue12/Part%20-%204/P51204100103.pdf

Netafim. (n.d.). *Hydraulic Calculation Tool*. Retrieved November 4, 2021, from http://www.netafim.com/service/hydrocalc-pro

Nordmann, T., Vontovel, Th., & Clavadetscher, L. (2012). *15 years of Practical Experience in Development and Improvement of Bifacial Photovoltaic Noise Barriers along Highways and Railway lines in Switzerland*. 3843–3847. https://doi.org/10.4229/27thEUPVSEC2012-5DO.7.2

Nussbaumer, H., Janssen, G., Berrian, D., Wittmer, B., Klenk, M., Baumann, T., Baumgartner, F., Morf, M., Burgers, A., Libal, J., & Mermoud, A. (2020). Accuracy of simulated data for bifacial systems with varying tilt angles and share of diffuse radiation. *Solar Energy*, *197*, 6–21. https://doi.org/10.1016/j.solener.2019.12.071

Nussbaumer, H. ; K. (2019). PV systems with lowest LCOE using bifacial modules: State-of-the-art Systems and components. *PV Tech Power*, *18*, 12.

Olcan, C. (2015). Multi-objective analytical model for optimal sizing of stand-alone photovoltaic water pumping systems. *Energy Conversion and Management*, *100*, 358–369. https://doi.org/10.1016/j.enconman.2015.05.018

Olszewski, P. (2016). Genetic optimization and experimental verification of complex parallel pumping station with centrifugal pumps. *Applied Energy*, *178*, 527–539. https://doi.org/10.1016/j.apenergy.2016.06.084

Palz, W. (2001). The French Connection: The rise of the PV water pump. *Refocus*, *2*(1), 46–47. https://doi.org/10.1016/S1471-0846(01)80096-2

Pelaez, S. A., Deline, C., Greenberg, P., Stein, J., & Kstuk, R. (2018). *Single-Axis Tracked Bifacial System Results*. 5th bifiPV Workshop, Colorado.

Pelaez, S. A., Deline, C., Greenberg, P., Stein, J. S., & Kostuk, R. K. (2019). Model and Validation of Single-Axis Tracking With Bifacial PV. *IEEE Journal of Photovoltaics*, *9*(3), 715–721. https://doi.org/10.1109/jphotov.2019.2892872

Pelaez, S. A., Deline, C., Stein, J. S., Marion, B., Anderson, K., & Muller, M. (2019). Effect of torque-tube parameters on rear-irradiance and rear-shading loss for bifacial PV performance on single-axis tracking systems. *2019 IEEE 46th Photovoltaic Specialists Conference (PVSC)*, *2*, 1–6.

Perez, R., Seals, R., Ineichen, P., Stewart, R., & Menicucci, D. (1987). A new simplified version of the perez diffuse irradiance model for tilted surfaces. *Solar Energy*, *39*(3), 221–231. https://doi.org/10.1016/s0038-092x(87)80031-2

Podlowski, L. (2019). Bifacial PV Technology Ready for Mass Deployment. In *PI Berlin*.

Reise, C., Baarah, G., Schnabel, E., Kräling, U., Müller, B., Chang, S., Choe, Y., & Cho, H. (2018). From bifaciality to yield: Different bifacial cell technologies may differ even more in annual outdoor performance. *35th European PV Solar Energy Conference and Exhibition*, 24–28.

Renu, Bora, B., Prasad, B., Sastry, O. S., Kumar, A., & Bangar, M. (2017). Optimum sizing and performance modeling of Solar Photovoltaic (SPV) water pumps for different climatic conditions. *Solar Energy*, *155*, 1326–1338. https://doi.org/10.1016/j.solener.2017.07.058

Santamaría, J., & Ledesma, J. R. (2023). Evaluating 2D View-Factor Solutions to Estimate Ground-Reflected Irradiance in Large Bifacial PV Plants. *40th European Photovoltaic Solar Energy Conference and Exhibition*, 020462-001-020462–007. https://doi.org/10.4229/EUPVSEC2023/4DV.4.30

Schneider, D. (2012). Control Algorithms for Large-scale Single-axis Photovoltaic Trackers. *Acta Polytechnica*, *52*, 86–92. https://doi.org/10.14311/1648

Shoukry, I., Libal, J., Kopecek, R., Wefringhaus, E., & Werner, J. (2016). Modelling of bifacial gain for stand-alone and in-field installed bifacial PV modules. *Energy Procedia*, *92*, 600–608.

Singh, J. P., Walsh, Timothy M., & Aberle, A. G. (2012). *Performance Investigation of Bifacial PV Modules in the Tropics*. 3262–3266.

Solera, J. S. (1985). *100 kWp Experimental PV Power Plant*. 504–508.

Soria, B., Gerritsen, E., Lefillastre, P., & Broquin, J. E. (2016). A study on the annual performance of bifacial photovoltaic modules in the case of vertical facade integration. *Energy Science &Engineering*, *4*(1), 17.

Stein, J. S., Holmgren, W. F., Forbess, J., & Hansen, C. W. (2016). PVLIB: Open source photovoltaic performance modeling functions for Matlab and Python. *2016 IEEE 43rd Photovoltaic Specialists Conference (PVSC)*, 3425–3430. https://doi.org/10.1109/PVSC.2016.7750303

Suehrcke, H., Appelbaum, J., & Breshef, B. (1997). Modelling a permanent magnet DC motor/centrifugal pump assembly in a photovoltaic energy system. *Solar Energy*, *59*(1–3), 37–42. https://doi.org/10.1016/s0038-092x(96)00117-x

Sun, X., Khan, M. R., Deline, C., & Alam, M. A. (2018). Optimization and performance of bifacial solar modules: A global perspective. *Applied Energy*, *212*, 1601–1610. https://doi.org/10.1016/j.apenergy.2017.12.041

Theristis, M., Riedel-Lyngskær, N., Stein, J. S., Deville, L., Micheli, L., Driesse, A., Hobbs, W. B., Ovaitt, S., Daxini, R., Barrie, D., Campanelli, M., Hodges, H., Ledesma, J. R., Lokhat, I., McCormick, B., Meng, B., Miller, B., Motta, R., Noirault, E., … Zhao, C. (2022). International Photovoltaic Modeling Intercomparison. *8th World Conference on Photovoltaic Energy Conversion (WCPEC-8)*, *1*. https://doi.org/10.2172/2004810

Theristis, M., Riedel-Lyngskær, N., Stein, J. S., Deville, L., Micheli, L., Driesse, A., Hobbs, W. B., Ovaitt, S., Daxini, R., Barrie, D., Campanelli, M., Hodges, H., Ledesma, J. R., Lokhat, I., McCormick, B., Meng, B., Miller, B., Motta, R., Noirault, E., … Zhao, C. (2023). Blind photovoltaic modeling intercomparison: A multidimensional data analysis and lessons learned. *Progress in Photovoltaics: Research and Applications*, *31*(11), 1144–1157. https://doi.org/10.1002/pip.3729

Van Campen, B., Guidi, D., & Best, G. (2000). *Solar Photovoltaics for Sustainable Agriculture and Rural Development*. FAO (Food and Agriculture Organization of the United Nations). https://doi.org/10.13140/RG.2.1.5056.4962

VDMA. (2018). *International Technology Roadmap for Photovoltaic. Results 2017 including maturity report 2018*.

Viaintermedia.com. (2017, October 23). *Fotovoltaica—Powen instala en el campo de Albacete un bombeo solar para autoconsumo de casi doscientos kilovatios—Energías Renovables*. Energías Renovables, el periodismo de las energías limpias.; Fotovoltaica - Powen instala en el campo de Albacete un bombeo solar para autoconsumo de casi doscientos kilovatios - Energías Renovables, el periodismo de las energías limpias. https://www.energias-renovables.com/fotovoltaica/powen-instala-en-el-campo-de-albacete-20171023

Viholainen, J., Tamminen, J., Ahonen, T., Ahola, J., Vakkilainen, E., & Soukka, R. (2012). Energy-efficient control strategy for variable speed-driven parallel pumping systems. *Energy Efficiency*, *6*(3), 495–509. https://doi.org/10.1007/s12053-012-9188-0

Wang, H., Cheng, X., & Yang, H. (2020). Temperature Coefficients and Operating Temperature Verification for Passivated Emitter and Rear Cell Bifacial Silicon Solar Module. *IEEE Journal of Photovoltaics*, *10*(3), 729–739. https://doi.org/10.1109/jphotov.2020.2974289

Wang, S., Wilkie, O., Lam, J., Steeman, R., Zhang, W., Khoo, K. S., Siong, S. C., & Rostan, H. (2015). Bifacial photovoltaic systems energy yield modelling. *Energy Procedia*, *77*, 428–433.

Yahyaoui, I., Atieh, A., Serna, A., & Tadeo, F. (2017). Sensitivity analysis for photovoltaic water pumping systems: Energetic and economic studies. *Energy Conversion and Management*, *135*, 402–415. https://doi.org/10.1016/j.enconman.2016.12.096

Yusufoglu, U. A., Lee, T. H., Pletzer, T. M., Halm, A., Koduvelikulathu, J., Comparotto, C., Kopecek, R., & Kurz, H. (2014). Simulation of energy production by bifacial modules with revision of ground reflection. *Energy Procedia*, *55*, 7. https://doi.org/10.1016/j.egypro.2014.08.111